INFORMATION TO USERS

This manuscript has been reproduced from the microfilm master. UMI films the text directly from the original or copy submitted. Thus, some thesis and dissertation copies are in typewriter face, while others may be from any type of computer printer.

The quality of this reproduction is dependent upon the quality of the copy submitted. Broken or indistinct print, colored or poor quality illustrations and photographs, print bleedthrough, substandard margins, and improper alignment can adversely affect reproduction.

In the unlikely event that the author did not send UMI a complete manuscript and there are missing pages, these will be noted. Also, if unauthorized copyright material had to be removed, a note will indicate the deletion.

Oversize materials (e.g., maps, drawings, charts) are reproduced by sectioning the original, beginning at the upper left-hand corner and continuing from left to right in equal sections with small overlaps.

ProQuest Information and Learning
300 North Zeeb Road, Ann Arbor, MI 48106-1346 USA
800-521-0600

UMI®

The Pennsylvania State University
The Graduate School
Department of Energy and Geo-Environmental Engineering

SECONDARY GAS MIGRATION LIMITED BY FRACTURED ROCK

A Thesis in
Petroleum and Natural Gas Engineering
by
Victor Siahaan

Submitted in Partial Fulfillment
of the Requirements
for the Degree of

Doctor of Philosophy

August 2002

UMI Number: 3064997

UMI Microform 3064997

ProQuest Information and Learning Company
300 North Zeeb Road
P.O. Box 1346
Ann Arbor, MI 48106-1346

We approve the thesis of Victor Siahaan.

Date of Signature

Peter B. Flemings — 7-3-02
Associate Professor of Geosciences
Thesis Co-Advisor
Chair of Committee

Paul J. Hicks, Jr. — May 15, 2002
ExxonMobil Upstream Research Co.
Thesis Co-Advisor
Special Member of Committee

Turgay Ertekin — July 01, 2002
Professor of Petroleum and Natural Gas Engineering
George E. Trimble Chair in Earth and Mineral Sciences

Abraham S. Grader — June 7 2002
Professor of Petroleum and Natural Gas Engineering
Victor G. Beghini Fellow

Phillip M. Halleck — 6-7-02
Associate Professor of Petroleum and Natural Gas Engineering

Michael A. Adewumi — 5-22-02
Professor of Petroleum and Natural Gas Engineering
Quentin E. and Louise L. Wood Fellow
In Charge of Graduate Programs in Petroleum and Natural Gas Engineering

Abstract

We present a conceptual and quantitative model to describe the interactions between minimum horizontal stress, pore pressure, and fracture permeability. The model is then coupled with a one-dimensional vertical fracture flow model to investigate the gas column height which can be trapped by a fractured caprock during steady-state gas migration. One and two-dimensional transient numerical flow models are developed to evaluate the formation of a gas cap within reservoir sands underlying fractured caprock. The model assumes that all flow in the caprock is via fracture permeability and that this permeability is a function of the effective minimum horizontal stress in the caprock. The absolute stress state within the caprock is assumed to be uncoupled from the pore pressure. Trap integrity is shown to depend strongly on the water charge rate, the fracture permeability model and the rock properties.

Table of Contents

List of Figures

Chapter 1

Chapter 3

Chapter 4

Chapter 5

Chapter 6

List of Tables

Nomenclature

Roman

a	Individual asperity surface area	L^2
A	Fracture area	L^2
A_x	Cross-sectional area normal to x direction	L^2
A_y	Cross-sectional area normal to y direction	L^2
A_z	Cross-sectional area normal to z direction	L^2
b	Width of the fracture perpendicular to flow	L
B	FVF, reservoir volume/volume at standard condition	L^3/L^3
B_g	Gas FVF	L^3/L^3
$B_{i,j,k}$	Transmissibility coefficient of $p_{i,j-1,k}$ in matrix notation	L^4T/M
B_w	Water FVF	L^3/L^3
$D_{i,j,k}$	Transmissibility coefficient of $p_{i-1,j,k}$ in matrix notation	L^4T/M
E	Young's Modulus	ML/T^2
$E_{i,j,k}$	Transmissibility coefficient of $p_{i,j,k}$ in matrix notation	L^4T/M
f	Load	ML/T^2
f_c	fractional contact area	L^2/L^2

F	Force	ML/T^2
$F_{i,j,k}$	Transmissibility coefficient of $p_{i+1,j,k}$ in matrix notation	L^4T/M
F_a	Force exerted by the asperities	ML/T^2
F_a/A	Effective stress	M/LT^2
F_{hmax}	Compression force caused by S_{hmax} over area A	ML/T^2
F_{hmin}	Compression force caused by S_{hmin} over area A	ML/T^2
F_p	Force caused by the pore pressure	ML/T^2
F_v	Compression force caused by S_v over area A	ML/T^2
g	Local gravitational acceleration	L/T^2
G	Pore geometrical factor	
$G_{i,j,k}$	Depth of block (i, j, k)	L
GWC	Gas water contact	L
$H_{i,j,k}$	Transmissibility coefficient of $p_{i,j+1,k}$ in matrix notation	L^4T/M
k	Permeability	L^2
k_f	Fracture permeability	L^2
k_r	Relative permeability	
k_{r_w}	Water relative permeability	
k_{r_g}	Gas relative permeability	
k_x	Permeability along x-direction	L^2

k_y	Permeability along y-direction	L^2
k_z	Permeability along z-direction	L^2
m	Mass per unit volume of porous medium	M/L^3
m_l	Mass of fluid with phase l per unit volume	M/L^3
$\dot{m}_l$	Mass flux of fluid with phase l	M/TL^2
N_t	Total number of asperities	
p	Pressure	M/LT^2
p_g	Gas pressure	M/LT^2
p_p	Pore pressure	M/LT^2
p_w	Water pressure	M/LT^2
P_c	Capillary pressure	M/LT^2
P_d	Displacement pressure	M/LT^2
dp/dl	Pressure gradient along l-direction	M/L^2T^2
q	Flow rate	L^3/T
q_g	Gas flow rate	L^3/T
q_w	Water flow rate	L^3/T
q_x	Flow rate in x-direction	L^3/T
q_y	Flow rate in y-direction	L^3/T
q_z	Flow rate in z-direction	L^3/T
$\tilde{q}_l$	Phase l rate depletion	M/T

Q	Flow rate at standard condition	L^3/T
Q_w	Water flow rate at standard condition	L^3/T
Q_g	Gas flow rate at standard condition	L^3/T
r	Radius of oil/gas globule	L
r_1, r_2	Principal radii of curvature of the interface between the phases	L
R_{sw}	Solution gas in water	L^3/L^3
s	Fracture spacing	L
s_x	Fracture spacing in x-direction	L
s_y	Fracture spacing in y-direction	L
s_z	Fracture spacing in z-direction	L
S_g	Gas saturation	L^3/L^3
$S_{g_{irr}}$	Gas irreducible saturation	L^3/L^3
S_{hmax}	Horizontal stress in y-direction	M/LT^2
S_{hmin}	Horizontal stress in x-direction	M/LT^2
$S_{i,j,k}$	Transmissibility coefficient of $p_{i,j,k-1}$ in matrix notation	L^4T/M
S_v	Vertical stress	M/LT^2
S_w	Water saturation	L^3/L^3
$S_{w_{irr}}$	Water irreducible saturation	L^3/L^3
S_1	Vertical stress	M/LT^2

S_2	Maximum horizontal stress	M/LT^2
S_3	Minimum horizontal stress	M/LT^2
T	Transmissibility	L^4T/M
$T_{l_{i\pm 1/2,\,j,\,k}}$	Phase l transmissibility along the x-direction between gridblock (i, j, k) and gridblock $(i \pm 1/2, j, k)$	L^4T/M
$T_{l_{i,\,j\pm 1/2,\,k}}$	Phase l transmissibility along the x-direction between gridblock (i, j, k) and gridblock $i, j \pm 1/2, k$	L^4T/M
$T_{l_{i,\,j,\,k\pm 1/2}}$	Phase l transmissibility along the z-direction between gridblock (i, j, k) and gridblock $i, j, k \pm 1/2$	L^4T/M
V_b	Bulk volume or control volume	L^3
ΔV	Deformation	L
w	Hydraulic fracture width	L
w_x	Hydraulic fracture width in x-direction	L
w_y	Hydraulic fracture width in y-direction	L
w_z	Hydraulic fracture width in z-direction	L
W_o	Maximum asperity height	L
x	Loaded asperity height or distance in x-direction	L
y	Distance in y-direction	L
z	Distance in z-direction	L

$Z_{i,j,k}$	Transmissibility coefficient of $p_{i,j,k-1}$ in matrix notation	L^4T/M

Greek

α_c	Unit conversion	
β	Minimum horizontal stress gradient	M/L^2T^2
β_c	Unit conversion	
γ	Gas-water interfacial tension	M/T^2
Δ	Difference operator	
Δt	Time step	T
Δx	Control volume dimension along the x-direction	L
Δy	Control volume dimension along the y-direction	L
Δz	Control volume dimension along the z-direction	L
ε	Tensile strain	
θ	Gas-water interfacial contact angle	Degree
μ	Viscosity	M/LT
μ_w	Water viscosity	M/LT
μ_g	Gas viscosity	M/LT
ρ	Density	M/L^3
ρ_w	Water density	M/L^3
ρ_g	Gas density	M/L^3
σ	Tensile stress	M/LT^2
σ_{hmin}	Effective stress	M/LT^2

υ_l	Superficial velocity of fluid with phase l	L/T
Φ_w	Water potential	M/LT^2
Φ_g	Gas potential	M/LT^2
$d\Phi/dl$	Potential gradient along the l-direction	M/L^2T^2
$\nabla\Phi$	Potential gradient	M/L^2T^2
ϕ	Porosity	L^3/L^3

Superscripts

k	Old iteration level
$k+1$	Current iteration level
n	Old time level
$n+1$	Current time level
θ	Time level in between n and $n+1$, $0<\theta<1$
$\circ$	Extrapolation value

Subscripts

c	contact area
g	gas phase
i	block index in x-direction
j	block index in y-direction
k	block index in z-direction
l	phase index
max	maximum
min	minimum
p	pressure

v	vertical
w	water phase
x	x-direction
y	y-direction
z	z-direction

Acknowledgments

I would like to thank Dr. Peter B. Flemings and Dr. Paul J. Hicks, Jr. for the support and guidance in completing this dissertation. I would also like to express my sincere gratitude and special thanks to Dr. Turgay Ertekin who made valuable suggestions which helped to overcome difficulties during my research and to other members of my committee, Dr. Abraham S. Grader, Dr. Phillip M. Halleck, and Dr. Michael A. Adewumi for their beneficial comments and suggestions while completing this research.

I also like to extend my thanks to my fellow graduate students in The Petroleum and Natural Gas Engineering at Penn State, particularly, my friends and colleges, Nuntawan Silpngarmlers and Gaoming Li, who have been helpful throughout my research.

Finally, I am very grateful to my mother, my brothers and sisters, and my other family members for their love, continued support, and encouragement while working toward this degree. I dedicate this thesis to my mother and the memory of my father.

Chapter 1
Introduction

This thesis is part of an ongoing research initiative to evaluate the development of overpressured basins. One of the major challenges in overpressured basins is to predict the presence of an effective seal. In this research we develop a model that couples the mechanical and hydraulic behavior of the seal (fractured caprock). Furthermore, the model is used to quantify the ability of a fractured caprock to entrap hydrocarbons in an underlying reservoir under varying *in-situ* stress and fluid charge conditions.

It has been observed in many sedimentary basins around the world that hydrocarbons (petroleum) migrated vertically through thick sequences of low-permeability caprock (e.g., Gulf of Mexico, SouthEast Asia) (Finkbeiner et al., 2001). This process (upward migration of hydrocarbons through the caprock) indicates that the low caprock permeability is enhanced through a certain mechanism. Here, we present a conceptual model of how this caprock permeability can be enhanced. A thorough understanding of the concept is useful in studying secondary hydrocarbon migration and entrapment. In the field of exploration, this concept can be used to trace hydrocarbons migration routes, to predict a seal capacity, to exploit the discovered fields, and to understand the distribution of hydrocarbons in the subsurface.

Methods of hydrocarbon migration and entrapment have been discussed and debated for years by petroleum engineers and geologists. Migration hypotheses vary from simple migration from the source rock into adjacent carrier bed (*primary migration*) and through the carrier bed to the trap (*secondary migration*), to complicated multi-stage migration schemes. In all migration hypotheses, the permeability pathways and barriers play an important role in hydrocarbon accumulation.

The simplest migration and entrapment model is the "fill and spill" model shown in Figure 1.1 (Gussow, 1954). Gussow (1954) was the first to describe this model. In this model, oil and gas expelled from the source rock coalesces to form continuous slugs in a carrier bed and migrates up structure under an impermeable caprock. The lowest structural trap along the migration path will be filled first. When the structure is filled, the hydrocarbons will spill from the structure and continue migrating up the carrier bed until another trapping structure is encountered.

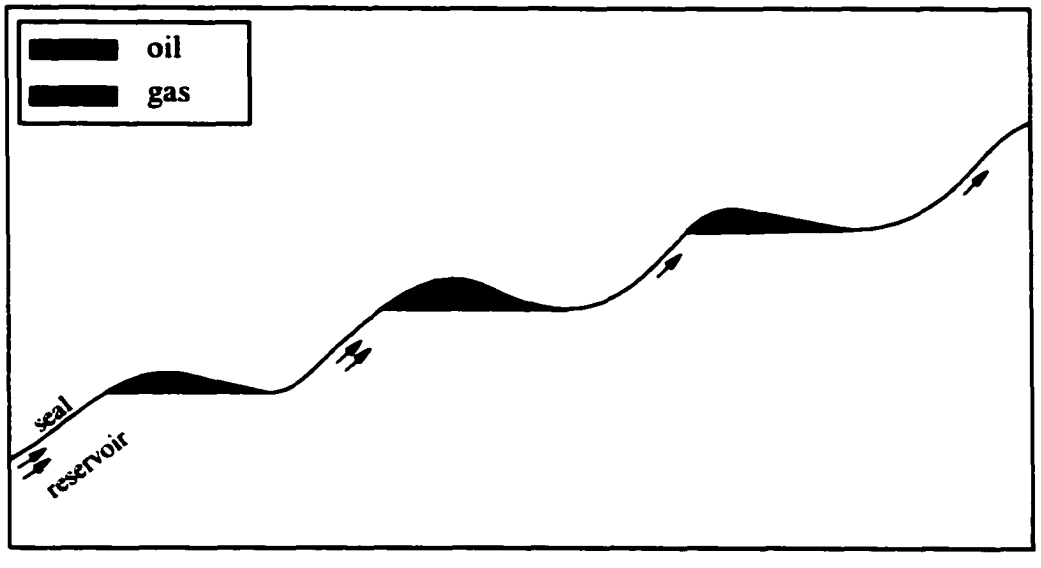

Figure 1.1: Structural differential entrapment of oil and gas (fill and spill) model (after Gussow, 1954).

A second model of migration and entrapment is the "capillary entry pressure" model. This model differs from the fill and spill model in that, rather than structure acting to trap the hydrocarbons, regions of low permeability and high capillary entry pressure within the carrier bed (e.g. Figure 1.2), inhibit vertical migration (Smith, 1966; Schowalter, 1976; Watts, 1987).

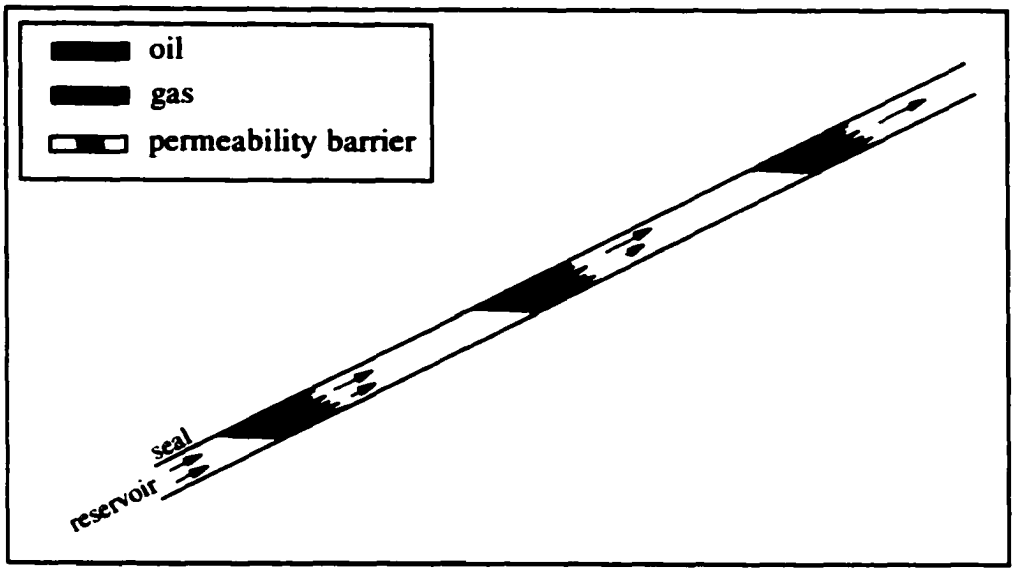

Figure 1.2: Capillary entry pressure model of entrapment by zones of low permeability and high capillary entry pressure (after Schowalter, 1976).

Berg (1975) has illustrated the capillary entry pressure model for secondary migration as shown in Figure 1.3. By considering an oil globule which is impelled by buoyancy and moves through the pores in a rock, he illustrated how the globule must be deformed in order to go through the pore throat. According to Berg, in a multi-phase system (oil-water) capillary pressure arises because of molecular forces at the interface between oil and water attempting to maintain the smallest surface area per volume possible, that of a sphere. If the globule deforms to squeeze through the pore throat, the pressure provided by buoyancy has to be greater than the opposing pressure (pore-entry or deformation pressure). When buoyancy pressure is less than the entry pressure no migration occurs. As pore throat size decreases, the amount of deformation necessary for the oil globule to enter the pore throat increases and thus the entry pressure increases.

Intrinsic permeability has been shown to be proportional to pore throat size and thus inversely proportional to capillary entry pressure, implying that zones of low permeability would also have high capillary entry pressure.

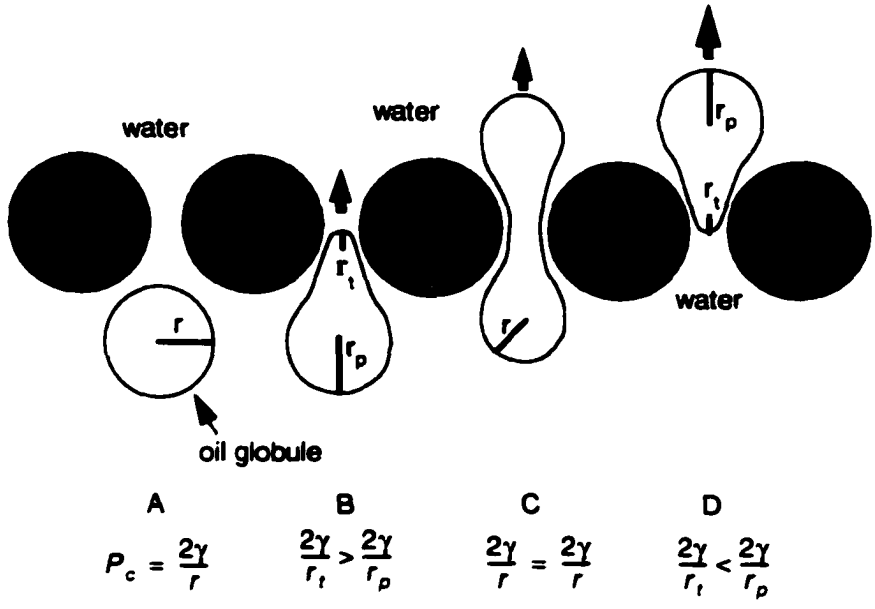

Figure 1.3: Diagram illustrating the interplay between capillary pressure and buoyancy as oil globule moves through the pore throat: (A) oil globule before it deforms; (B) buoyancy force is sufficient to distort oil globule, but capillary pressure of globule in pore throat exceeds capillary pressure of globule in the pore because radius of pore throat is smaller than the maximum radius of pore; (C) buoyant force in globule equals the capillary pressure in pore throat; (D) buoyant force in globule is larger than the capillary pressure in the pore throat and the globule moves through the pore throat (after Berg, 1975).

Both the "fill and spill" and "capillary entry pressure" models are static, meaning they predict hydrocarbon column heights that depend only on static rock and fluid properties. Bennett (1996) proposed a dynamic entrapment model (Figure 1.4) where reservoir sands juxtaposed to a low permeability fault zone are charged by hydrocarbons migrating up a fault. The resulting steady-state hydrocarbon column height in the reservoir sands is a dynamic function of the hydrocarbon flux in the fault. Ashbaugh (1997) further showed that the column height depended upon both the hydrocarbon and the water flux in the fault. In both models the hydraulic properties of the fault were independent of both the fluid pressures and the stress-state of the fault zone.

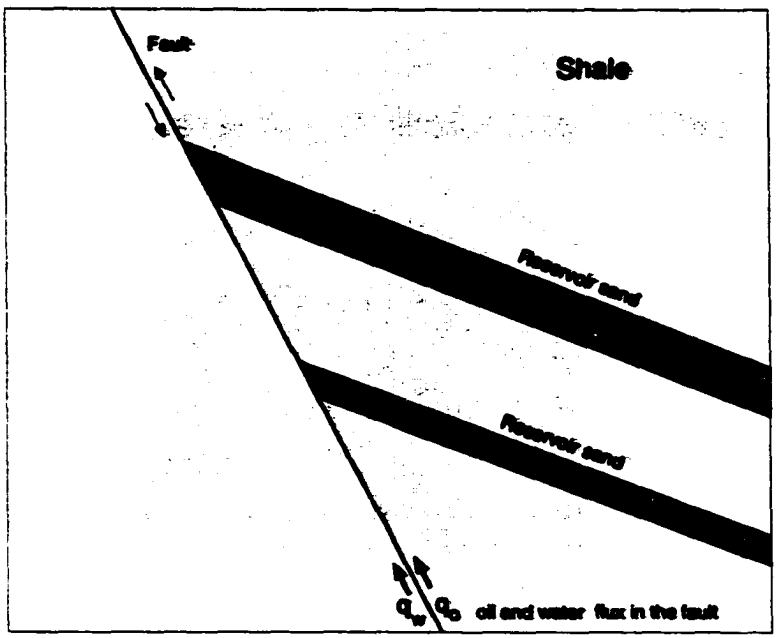

Figure 1.4: Dynamic column height model where fault zone acts as both the migration pathway and the trapping mechanism.

In this research, we consider a fractured caprock which acts as both a migration pathway and as the trap seal. This model differs from a dynamic entrapment model in that the mechanical and hydraulic properties of the fractured rock are a function of the fluid pressure within the fracture and the stress-state of the caprock.

Consider the interbedded sand-shale system shown in Figure 1.5. As hydrocarbons (oil and gas) are generated in the source rock, buoyant forces cause them to migrate laterally and vertically. The low permeability shale caprock initially serves as a seal to prevent "cross-strata hydrocarbon migration" due to their high displacement pressure, low permeability, and lateral continuity (Downey, 1984). As the filling process continues, the buoyant pressure of the hydrocarbon increases. If the hydrocarbon phase pressure (capillary pressure) exceeds the displacement pressure of the caprock, hydrocarbons will displace water in the caprock and will migrate through the caprock pore throats as a continuous oil or gas phase (Schowalter, 1976).

The presence of natural fractures in the caprock act to both increase the permeability and decrease the displacement pressure. This allows hydrocarbons to breach the seal, resulting in underfilled traps (traps not filled to the spill point).

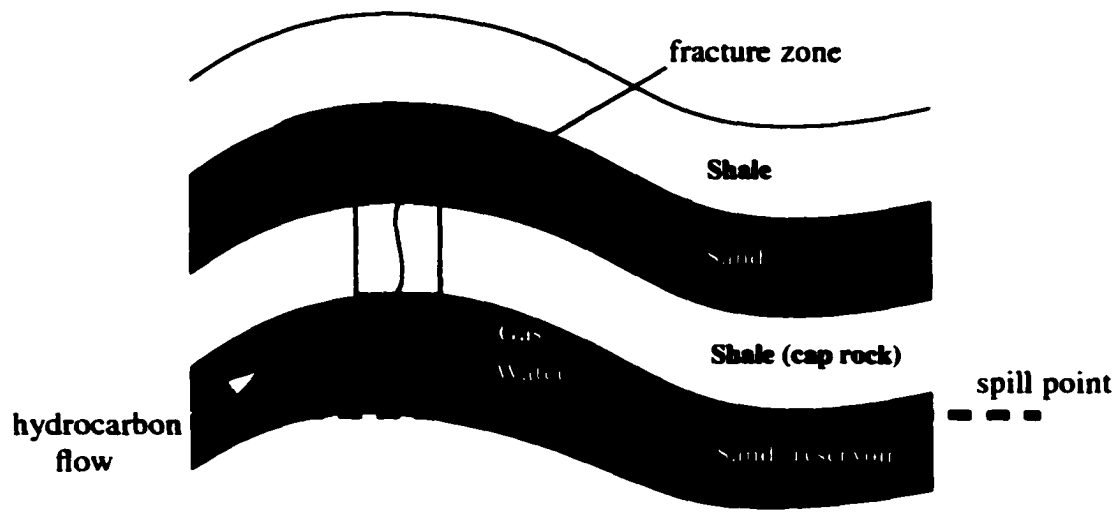

Figure 1.5: Cross-strata hydrocarbon migration through a fractured caprock occurs as a high permeability reservoir sand is charged by hydrocarbons. The structural trap in the reservoir sand is underfilled (not filled down to the spill point) due to hydrocarbon migration through the fractured shale caprock.

Chapter 2

Objectives and Approach

When the trap exists (e.g. Figure 1.5), fluid pressure in excess of the hydrostatic can occur (overpressure). In this environment, it is expected that fluid pressure gradient in the underlying reservoir is hydrostatic due to the high permeability of the reservoir and low fluid velocities in the reservoir. However, within the lower permeability caprock, pressures may increase significantly above hydrostatic. This overpressure facilitates the enhancement of the caprock permeability.

2.1 Objectives

The objectives are: 1) to characterize and quantify the permeability and displacement pressure of the fractured caprock (under overpressures condition) for use as a tool to predict trap integrity, 2) to relate fracture permeability and the displacement pressure of the caprock to the fluid pressure within the fracture and the stress-state of the caprock, and 3) to develop a simple formulation for the effective stress that relates fluid pressure and S_{hmin}.

2.2 Approach

We will construct our model in a step-wise fashion. First, we develop a model of the mechanical behavior of the fractured caprock. In this development, the elastic properties of the host rock, the topography of the fracture surface (fractional contact area), the fluid pressure within the fracture, and the stress state of the host rock are considered.

Second, we present a model to relate hydraulic properties (hydraulic width and permeability) of the fracture to the mechanical behavior. It is assumed that fracture planes behave like smooth parallel-plates. This assumption is based on the small fractional

contact area found in the model. The fractional contact area which is defined as the ratio of the contact area of the asperities to the fracture surface is presented. Furthermore, we calibrate and scale the model using the actual data (Fisher and Zwart, 1996).

Third, we combine the mechanical and hydraulic models to develop a 1-D steady-state flow model describing two-phase fluid flow in the fracture and predict hydrocarbon column height in the underlying reservoir. In this model, capillary pressure of the fracture is constructed based on the smooth parallel-plates model and is a function of fluid pressure and S_{hmin} within the caprock.

Finally, we extend the 1-D steady-state flow model to a 2-D transient numerical flow model. Using mass-conservation and Darcy's equation, a seven-point finite-difference simulator is constructed. The mechanical and hydraulic models are inserted into the model. The model is then used to study trap integrity in the secondary hydrocarbon migration where the column height is limited by the fluid pressure and the stress field.

Chapter 3

Mechanical behavior of tensile fractures

We begin our model development by considering the mechanical behavior of a fractured rock and the key parameters controlling this behavior. In particular, we will relate fracture deformation to normal stress, fluid pressure, fracture surface topography, and elastic properties of the host rock.

3.1 Stress State

We first look at a representative volume within the cap rock. The stress tensor acting upon the volume can be described in terms of three orthogonal stresses (S_1, S_2, and S_3). This is shown in Figure 3.1. By definition S_1 is greater than S_2 and S_2 is greater than S_3. In our model, it is assumed that the largest of the principle stresses is oriented vertically, thus $S_1 = S_v$. Then the remaining two principle stresses are horizontal and by definition the least (minimum) principle stress is horizontal, $S_3 = S_{hmin}$. Furthermore, we assume that all fractures are tensile (mode 1) fractures, which are perpendicular to the principle stresses. The aperture of fractures decrease under increasing effective stress (Jones, 1975; Tsang and Witherspoon, 1981; Walsh, 1981).

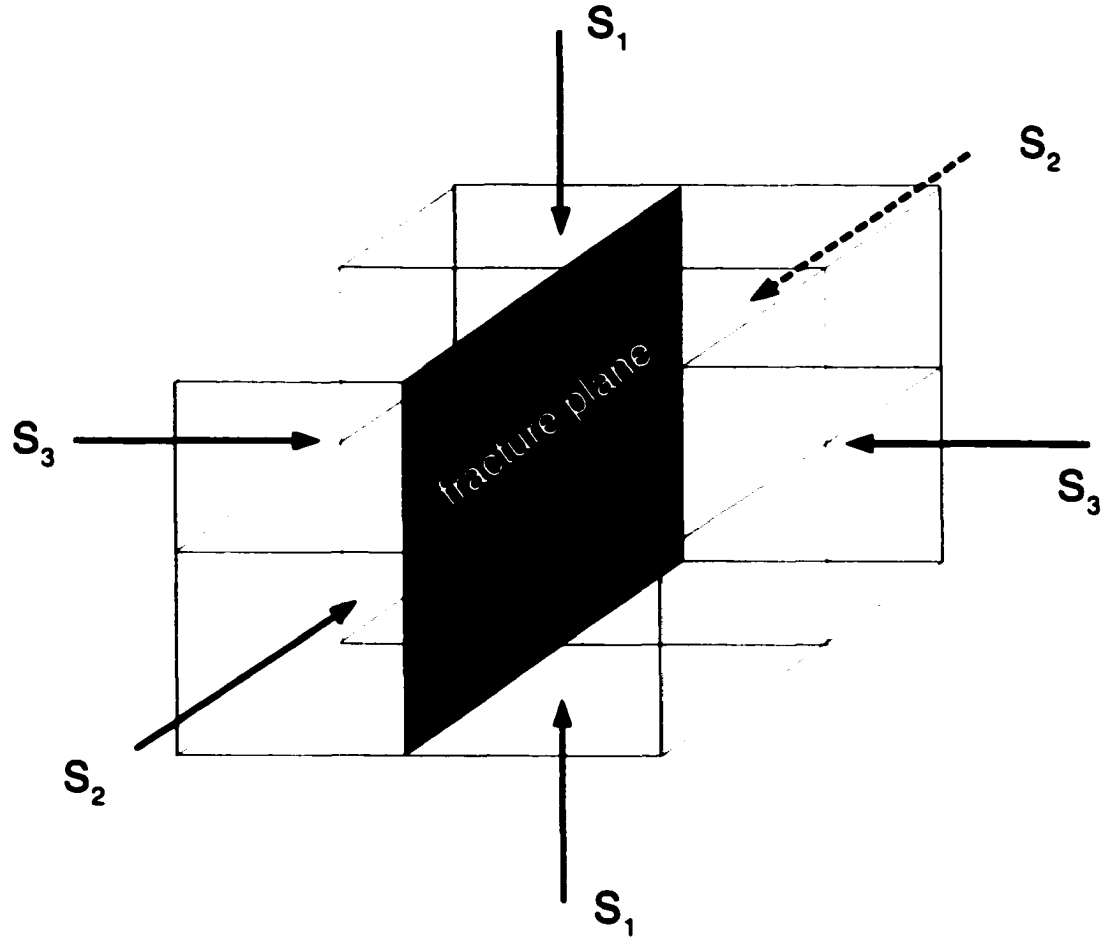

Figure 3.1: Representative rock volume depicting three orthogonal principle stresses (mode 1) and three fracture planes. The largest principle stress is assumed to be vertical and is termed $S_v = S_1$. The least principle stress is horizontal ($S_{hmin} = S_3$).

3.2 Fluid pressure

We consider fractures that are normal to S_{hmin}, S_{hmin} acting to close the fracture and the pore pressure (p_p) acting to keep the fracture open (Figure 3.2). In the figure, W represents the fracture width, F_a represents the force exerted by the asperities over the

area a, F_p represents the force caused by the pore pressure (p_p) acting on the area ($A - a$), and F_{hmin} represents the compression force caused by S_{hmin} over area A. The term asperity has been used by several authors (Gangi, 1978; Walsh and Grosenbaugh, 1979) to describe the pinnacles present on the fracture surface.

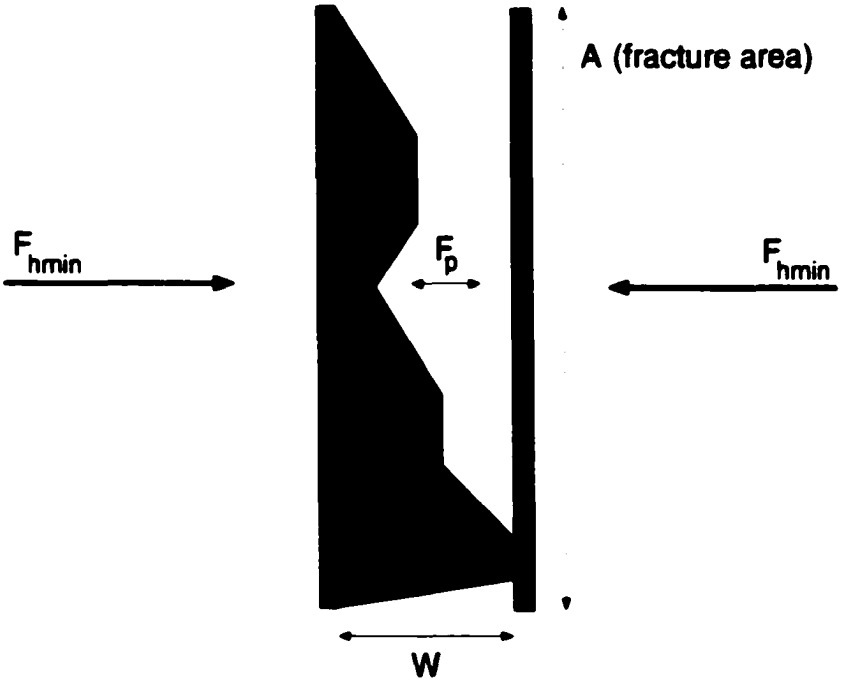

Figure 3.2: 2-D depiction of forces acting on a fracture.

Increases in S_{hmin} act to close the fracture and increases in p_p act to open the fracture. At equilibrium, the summation of forces working on a system must equal to zero:

$$\sum F = 0 \tag{3.1}$$

$$F_{hmin} = F_p + F_a \tag{3.2}$$

$$F_a = F_{hmin} - F_p \tag{3.3}$$

Dividing Eqn. 3.3 by nominal fracture plane area A yields:

$$\frac{F_a}{A} = \frac{F_{hmin}}{A} - \frac{F_p}{A} \tag{3.4}$$

$$\frac{F_a}{A} = S_{hmin} - \left(\frac{A-a}{A}\right) p_p \tag{3.5}$$

where F_a/A is the axial stress or the horizontal effective stress (see Figure 3.2).

3.3 Modeling a fracture with a single asperity

We model the deformation of a single asperity that separates two parallel plates. The asperity is modeled as a cylindrical elastic solid of length W_o at zero stress and the stress is assumed to be *uniaxial*. The 3-D depiction of forces acting on a fracture is shown in Figure 3.3. The final crack aperture is represented by $W_o - \Delta V$ while the ΔV represents the total deformation resulting from the applied load F_{hmin}. In the figure, x represents the loaded asperity height.

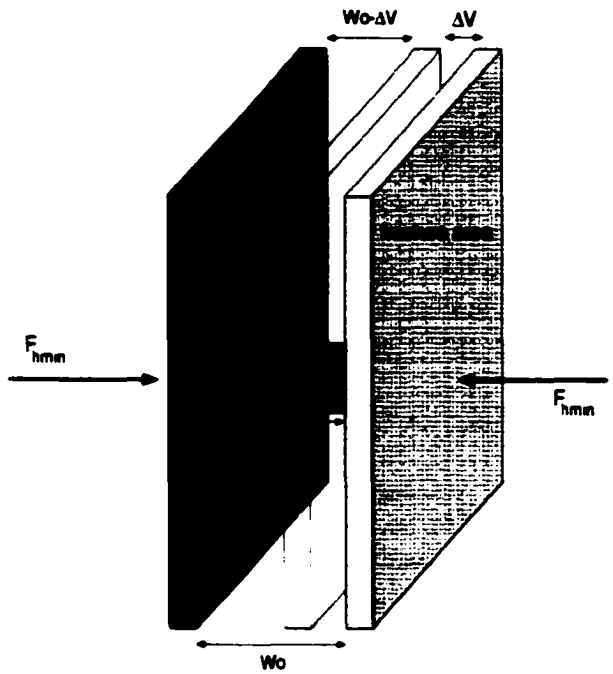

Figure 3.3: Single asperity elastic model.

Under the assumption of uniaxial stress, the tensile stress (σ) is proportional to tensile strain (ε) and can be expressed as:

$$d\sigma = -Ed\varepsilon \tag{3.6}$$

$$d\left(\frac{f}{a}\right) = -E\left(\frac{dx}{x}\right) \tag{3.7}$$

where f is the load supported by the single asperity, a is the cross-sectional area of the asperity and is approximated to be constant, E is the intact rock Young's modulus, and x is the asperity length (loaded height).

Integration of Eqn. 3.7 yields:

$$\int_0^{f_1} df = -Ea \int_{W_o}^{(W_o-\Delta V)} \frac{dx}{x} \tag{3.8}$$

$$f_1 = -Ea\ln\left(\frac{W_o - \Delta V}{W_o}\right) \tag{3.9}$$

Dividing Eqn. 3.9 by the fracture plane area (A) yields:

$$f_1/A = -\frac{Ea}{A}\ln\left(\frac{W_o - \Delta V}{W_o}\right) \tag{3.10}$$

where (f_1/A) is the axial stress or the effective stress that controls the crack aperture.

We now examine Eqn. 3.10 to study the mechanical behavior of tensile fracture for a single asperity. Result of the study is plotted in Figure 3.4 as an axial stress vs. deformation. We observe that even for a single asperity, the relationship between stress and deformation is non-linear for large strains. We used data (including sample dimensions) from Iwai's (1976) laboratory sample (Sierra white granite) to study this behavior. In Iwai's (1976) sample, the fractures were artificially made tension cracks. These artificially made tension cracks are then used to investigate the laws governing flow in natural rock fractures. The Young's modulus (E) for the Sierra white granite sample is $4.44\times10^4\ MPa$.

Snow (1968) had reported that fracture apertures at damsites varied between 50 um at a depth of 50 meters to 100 um at a depth of 15 meters. In Iwai's (1976) experiments, the fracture apertures are ranged from zero to 250 um. Based on these measurements, in this study we use a maximum asperity height (W_o) of 120 um in our models.

Gangi (1978) through his "bed of nails" model showed that the ratio of the contact area of the asperities to the fracture surface is small. Using the "bed of nails" model, Gangi (1978) matched Nelson's (1975) experimental data for sandstones and found

that the fractional contact area is only about 4% of the total fracture surface. He further showed that to match Jones' (1975) experimental data for fractures in carbonate rocks the contact area is much less than 4% ($a \ll A$). Based on this knowledge and for the purpose of studying the relationship between stress and deformation in the single asperity model, we assigned fractional contact area (f_c) to 0.4E-03 (0.4%).

Figure 3.4 shows the deformation up to 30 um for asperity heights of 120 um. In Iwai's (1976) experiments for sample Sierra white granite, Iwai (1976) showed the deformation up to 150 um for maximum asperity heights of 250 um. There is possibility that at very large strain the asperities would be crushed. This interpretation is supported by Iwai's (1976) flow data after repeated loadings. Iwai's (1976) results for flow versus stress differ substantially from cycle to cycle while the flow essentially remains constant. By comparison with the sample basalt where the asperity heights are relatively "uniform", the crushing of asperities is less probable.

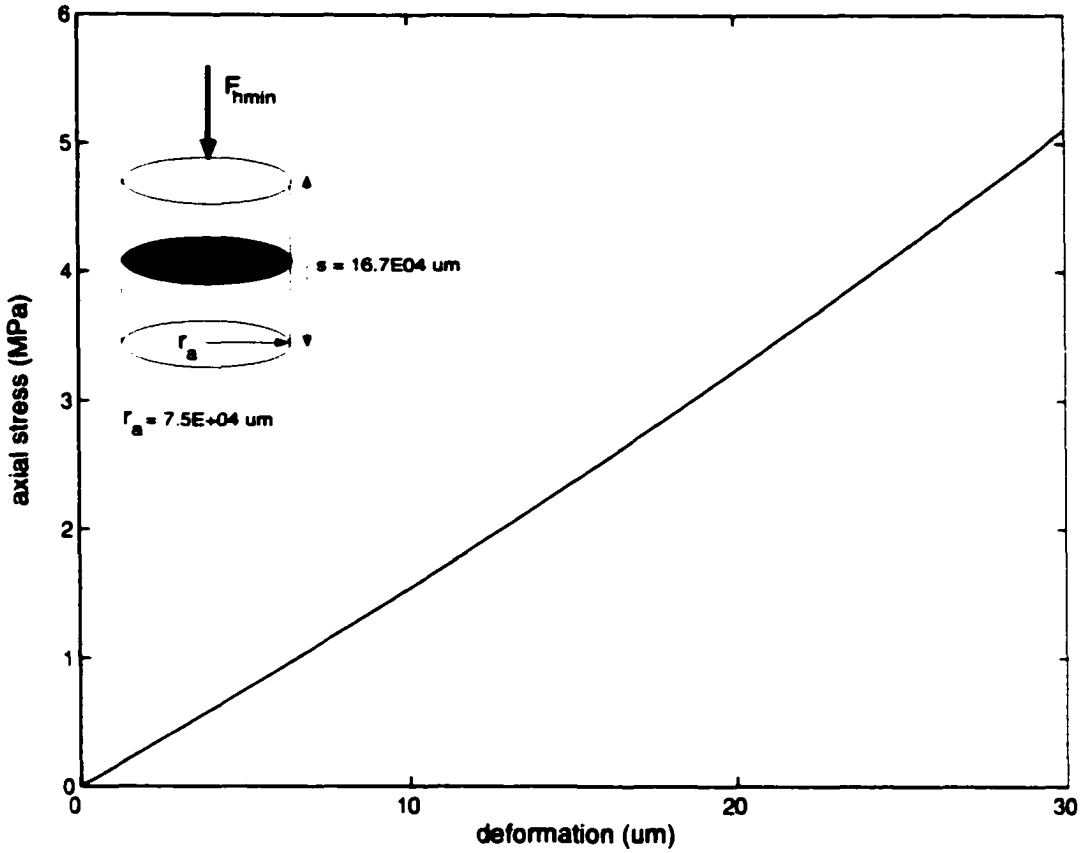

Figure 3.4: Mechanical behavior of tensile fracture for a single asperity. A single asperity model is used to study the relationship between the axial stress and fracture deformation. In this study, Eqn. 3.10 is used and is applied to Iwai's (1976) sample (Sierra white granite). The sample dimensions and the artificial made fracture are shown. The Young's modulus (E) for the Sierra white granite is 4.44×10^4 MPa and the maximum asperity height at zero effective stress (W_o) is assigned as 120 um. The fractional contact area (f_c) is assigned to be 0.4 %. It can be seen through the figure that the relationship between the axial stress and the deformation is non-linear for a large strain.

3.4 Modeling fracture deformation with multiple asperities of equal length

We extend our investigation to multiple asperities where each asperity has the same length. Figure 3.5 illustrates the model. Wo is the maximum crack aperture which is the asperity height at zero stress and $Wo - \Delta V$ represents the final crack aperture while ΔV represents the total deformation resulting from the applied load F_{hmin}. Again, x represents the loaded asperity height.

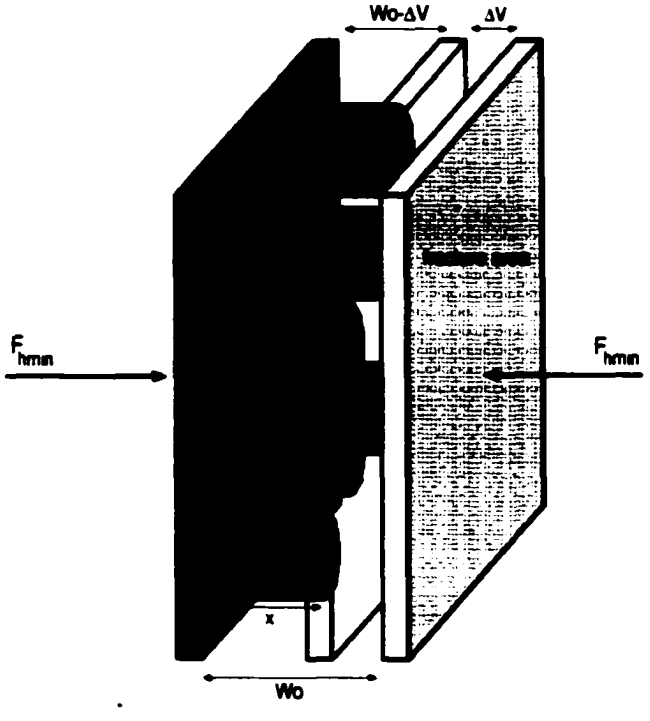

Figure 3.5: Multiple asperities elastic model.

For multiple asperities with the same asperity height, we can re-write Eqn. 3.8 as:

$$F_a = f_1 + f_2 + f_3 + \ldots + f_n \tag{3.11}$$

$$F_a = -E_1 a_1 \int_{W_o}^{W_o - \Delta V} \frac{dx}{x} - E_2 a_2 \int_{W_o}^{W_o - \Delta V} \frac{dx}{x} - E_3 a_3 \int_{W_o}^{W_o - \Delta V} \frac{dx}{x} - \ldots - E_n a_n \int_{W_o}^{W_o - \Delta V} \frac{dx}{x} \tag{3.12}$$

Assuming all asperities have the same Young's modulus (E) and the same constant cross-sectional area ($a_1 = a_2 = a_3 = \ldots = a_n$), we simplify Eqn. 3.12 to:

$$F_a = -N_t E a \int_{W_o}^{W_o - \Delta V} \frac{dx}{x} \tag{3.13}$$

where F_a is the total load supported by the asperities, N_t is the total number of asperities, E is the intact rock Young's modulus, a is the cross-sectional area of a single asperity, W_o is the maximum crack aperture, $W_o - \Delta V$ is the final crack aperture, and x is the asperity height.

Dividing Eqn. 3.13 by the total fracture area A and integrating yields:

$$F_a/A = \frac{-N_t E a}{A}\left(\int_{W_o}^{W_o - \Delta V} \frac{dx}{x}\right) \tag{3.14}$$

$$F_a/A = \frac{-N_t E a}{A} \ln\left(\frac{W_o - \Delta V}{W_o}\right) \tag{3.15}$$

where (F_a/A) is the axial stress or the effective stress.

The same relationship between stress and fracture width is obtained using a single asperity or multiple smaller asperities as long as the asperities have the same Young's modulus, height at zero stress and the sum of cross-sectional area of the smaller asperities equals the cross-sectional area of the single larger asperity.

We use Eqn. 3.15 to study the mechanical behavior of a tensile fracture. Figure 3.6 shows the behavior of tensile fracture. As the number of asperities increases, which is described in term of f_c (fractional contact area), the total stress needed to effect the same deformation increases.

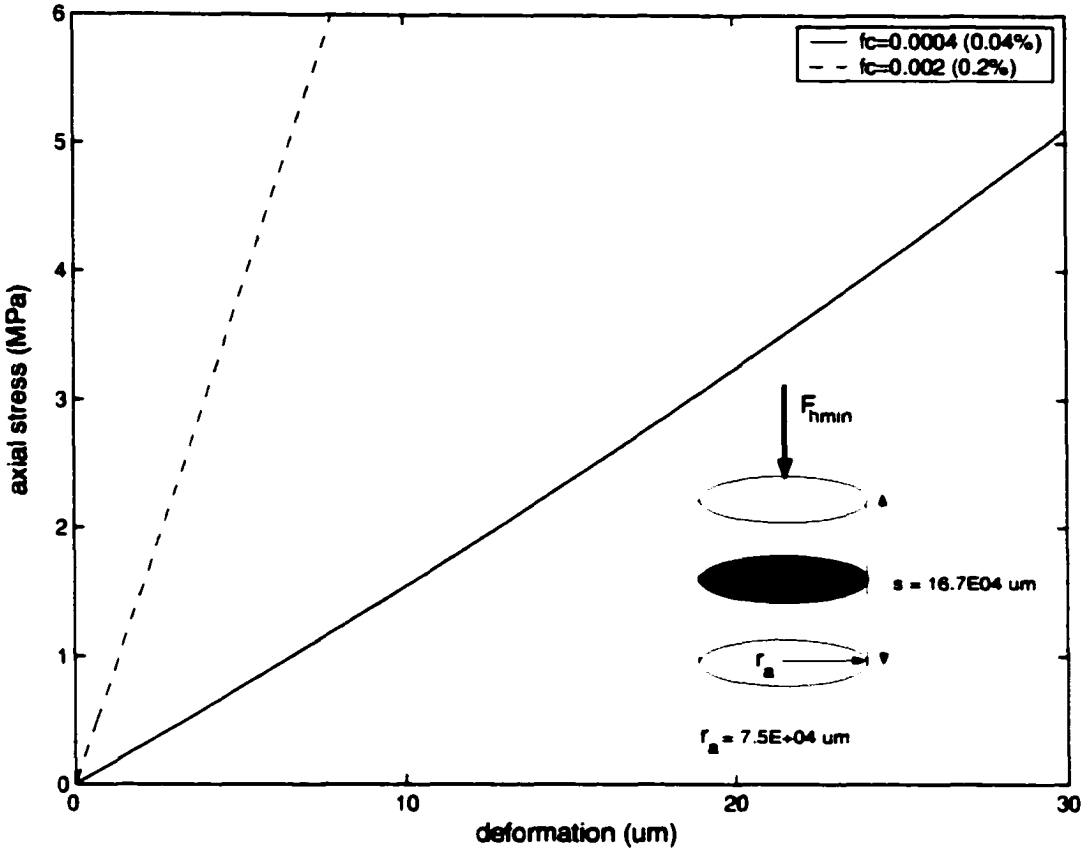

Figure 3.6: Mechanical behavior of tensile fracture for multiple asperities with the same asperity height. Similar to a single asperity model, in multiple asperities model, we study the relationship between the axial stress and the fracture deformation. In this study, Eqn. 3.15 is used and is applied to Iwai's (1976) sample (Sierra white granite). The sample dimensions and the artificially made fracture are shown. Two different values of f_c are used. It can be seen through the figure that as the contact area become larger, the total stress needed to effect the same deformation with the smaller contact area increases (see caption of Figure 3.4).

Chapter 4
Hydraulic behavior of tensile fractures

We have developed and studied a model that describes the mechanical behavior of a rough-walled fracture in response to external stress and internal/pore pressure (Chapter 3). We now investigate the hydraulic properties of a fracture described by this mechanical model.

4.1 Mathematical expression of fractured rock bulk permeability

We define the permeability for a single fracture as (et al., 1960):

$$k_f = \frac{w^2}{12} \tag{4.1}$$

where k_f is the fracture permeability and w is the hydraulic width of the fracture.

Equation 4.1 is obtained from a cubic law and from an analogy of cubic law to Darcy's equation. In the cubic law, the fracture is conceptualized as the void space between two smooth parallel plates. The vertical separation between the two plates (w) is constant and the plates are oriented horizontally. The steady-state equation for laminar, incompressible flow for this system (fluid flow in a medium bounded by two-parallel plates) is the two-dimensional Stokes equation. With a horizontal fracture of constant cross section in x-direction and for 1-D flow (x-direction), Stokes equation can be integrated to form the cubic law as:

$$q = -b \frac{w^3}{12\mu} \frac{dp}{dx} \tag{4.2}$$

where q is the volumetric flow rate, b is the width of the fracture perpendicular to the flow, μ is the viscosity of the fluid, and dp/dx is the pressure gradient applied to the

fluid along the x-direction. By analogy to Darcy's law $q = \frac{kA_x}{\mu}\frac{dp}{dx}$ (neglecting depth gradient) where $A_x = bw$, the fracture permeability (k_f) can be defined as in Eqn. 4.1.

If the permeability of the surrounding rock (matrix) is assumed zero or much less than the fracture permeability then the bulk rock permeability can be determined from:

$k_f = \frac{w^3}{12s}$ where s is the fracture spacing.

Figure 4.1 describes fractured rock with spacing s and fracture width w. The minimum horizontal force that pushed the fracture to close is represented by F_{hmin}, and the forces that maintain the fracture to open are represented by F_p and F_a.

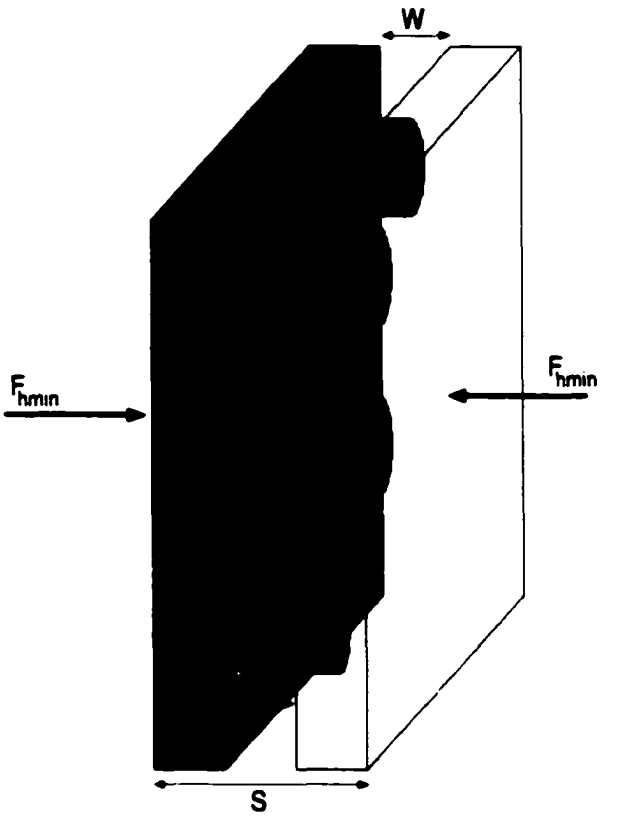

Figure 4.1: 3-D, physical representation of fractured rock.

4.1.1 Bulk permeability for multiple fractures

Now consider a rock with multiple fractures as shown in Figure 4.2. A rock with length L_b has multiple fractures spaced s apart. The horizontal effective stress σ_{hmin}, which we approximate as $\sigma_{hmin} = S_{hmin} - \alpha p_p$ where $\alpha = (1 - f_c)$ and f_c is the fractional contact area, can decrease by one of two mechanism: p_p could increase or S_{hmin} could decrease. We assume a constant stress (S_{hmin} = constant) boundary condition. Thus when p_p increases, the fractures expand freely and independently as described in Chapter 3.

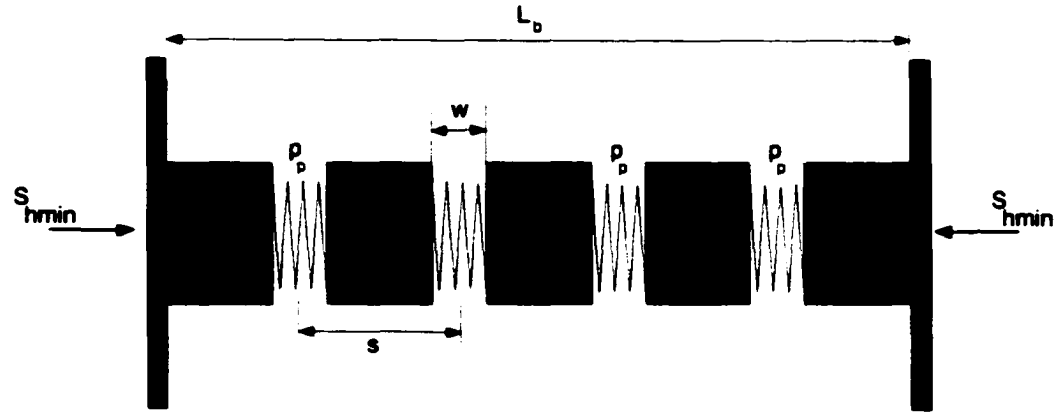

Figure 4.2: Model of a rock with multiple fractures spaced at an interval s. A constant stress boundary is applied. The spring of length w describes the mechanical behavior of the asperity model. The horizontal effective stress (σ_{hmin}) will change if either the pore pressure p_p or the minimum horizontal stress S_{hmin} changes. We assume a constant stress boundary, thus when p_p increases or decreases the fractures will dilate or close, respectively.

4.1.2 Bulk permeability in 3-D

Consider horizontal flow in the x-direction with no depth gradient (Figure 4.3). The representative cross-sectional area of the fractures perpendicular to the flow is given by:

$$A_x = s_y w_z + s_z w_y - (w_z w_y) \tag{4.3}$$

where A_x is the cross-sectional area, s_y and s_z are the spacings, and w_z and w_y are the fracture widths. For a simple case where fractures are parallel to the flow and assuming $w_z w_y \ll s_y w_z + s_z w_y$, the rate through the fracture is given by:

$$q_x = \left(s_y w_z \frac{-w_z^2}{12\mu} + s_z w_y \frac{-w_y^2}{12\mu} \right) \frac{dp}{dx} \tag{4.4}$$

where q_x is the flow rate through the fracture, μ is the viscosity, and dp/dx is the pressure gradient in the x-direction.

Recall Darcy's equation for horizontal flow (neglecting gravity):

$$q_x = (s_y s_z) \frac{-k_x}{\mu} \frac{dp}{dx} \tag{4.5}$$

q_x is the horizontal flow rate in x direction and k_x is the bulk permeability. In Darcy's equation, the cross-sectional area perpendicular to flow is represented by the total area, thus the cross-sectional area is $A_x = s_y s_z$

By comparing Eqn. 4.4 and 4.5, the bulk permeability k_x can be obtained from:

$$k_x = \frac{w_y^3}{12 s_y} + \frac{w_z^3}{12 s_z} \tag{4.6}$$

k_y and k_z can be obtained in a similar fashion:

$$k_y = \frac{w_x^3}{12s_x} + \frac{w_z^3}{12s_z} \tag{4.7}$$

$$k_z = \frac{w_x^3}{12s_x} + \frac{w_y^3}{12s_y} \tag{4.8}$$

Figure 4.3 below shows the 3-D model used to describe fracture permeability. Three sets of orthogonal fractures are assumed to be present. The hydraulic fracture width in x, y, and z direction are represented by w_x, w_y, and w_z. The fracture spacing are represented by s_x, s_y, and s_z and the minimum horizontal, maximum horizontal, and vertical forces are represented by F_{hmin}, F_{hmax}, and F_v, respectively.

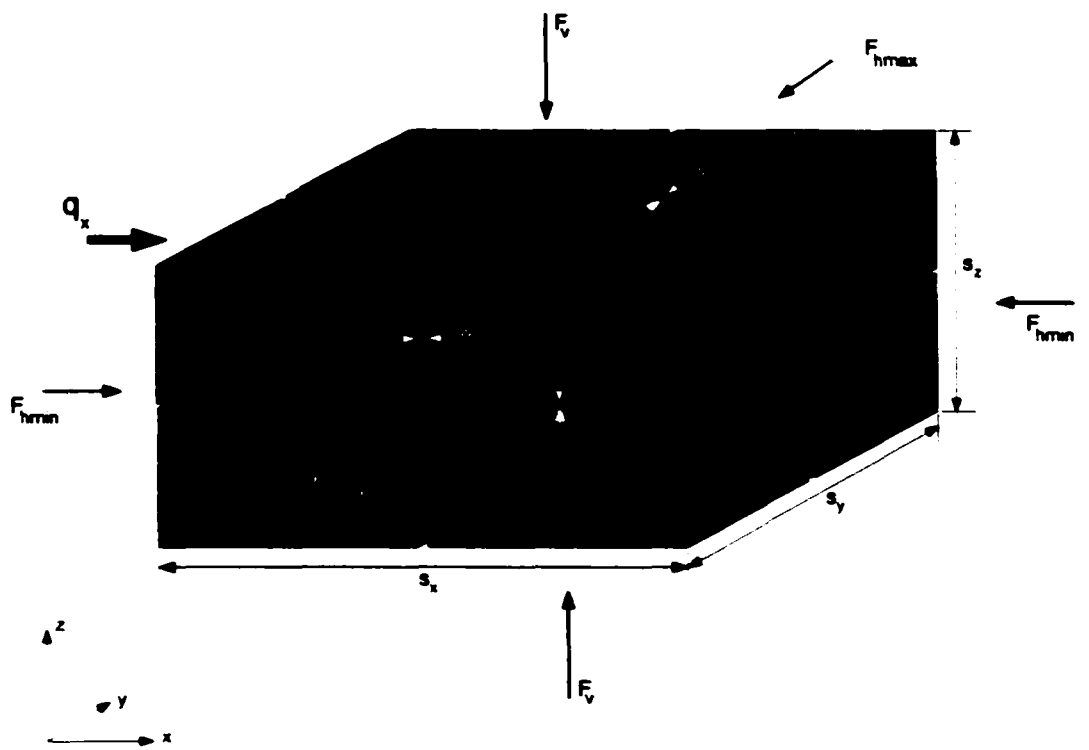

Figure 4.3: 3-D model to describe fracture permeability. In the figure, q_x represents fluid flow in x-direction.

Equations 4.6, 4.7, and 4.8 are similar to the equation derived by Elsworth and Mase (1993) for the conductivity of a fractured media. In their derivation, they consider flow through the fractured and add matrix permeability directly into their derivation by assuming that there is no discrepancy between the actual and the equivalent hydraulic aperture. In the case where the fracture conductivities dominate matrix conductivities, the matrix permeability can be neglected. In this research, we assume flow through the matrix is negligible.

4.2 Experimental data vs. asperity model

We now use the asperity model to describe the behavior of a clay caprock. We use Fisher and Zwart (1996) data to calibrate and scale the model. Fisher and Zwart (1996) measured bulk permeability along a plate boundary fault in the decollement zone between North American and Caribbean plates. They calculated bulk permeability from data derived from pulse tests, flow tests, recovery tests, and slug tests. Based on their data (Figure 4.4 and Table 4.1), they developed a correlation between bulk permeability and vertical stress. Their best fit correlation is $k = 10^{-8.3 - 1.6\sigma_v}$ where k is bulk permeability in cm^2 and σ_v is the vertical effective stress in MPa.

Figure 4.4 shows their experimental results taken from Leg 156 packer and ODPNaut tests. Open symbols indicate the effective stresses at the start of test periods while solid symbols indicate effective stresses at the end of test periods. Circles and diamonds are results for pulse tests and triangles-upward and squares are results for flow and recovery tests. These data were calculated during Leg 156 packer tests. The triangles-right are results from slug tests calculated during ODPNaut tests. The solid line is their best fit of log permeability to vertical effective stress. Table 4.1 provides the values the Leg 156 packer tests and ODPNaut tests. The effective stresses at the start and at the end of test periods and the calculated permeability are also given.

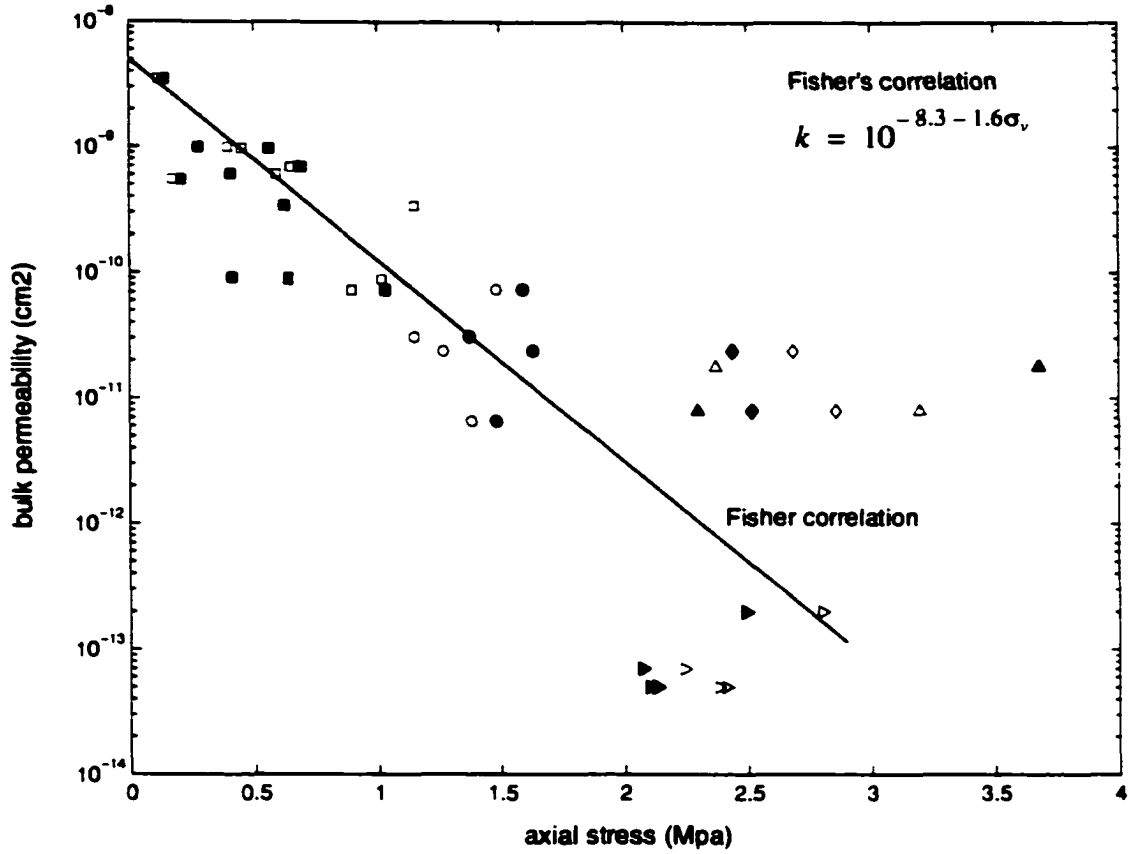

Figure 4.4: Permeability vs. vertical effective stress in a plate-boundary fault. In the figure, open symbols represent the effective stresses at the start of the test periods and solid symbols represent the effective stresses at the end of test periods. Circles and diamonds are results from pulse tests and triangles-upward are results from flow and recovery tests. The triangles-right are results from the slug tests calculated during the ODPNaut tests. The solid line represents their best fit correlation of the effective stress and the permeability (after Fisher and Zwart, 1996).

Table 4.1: Actual Fisher and Zwart (1996) data

σ_v at start (MPa)	σ_v at end (MPa)	k (cm^2)
2.685	2.440	2.4×10^{-11}
2.860	2.520	8.0×10^{-12}
2.372	3.678	1.8×10^{-11}
3.200	2.300	8.0×10^{-12}
1.268	1.632	2.4×10^{-11}
1.485	1.589	7.4×10^{-11}
1.384	1.484	6.6×10^{-12}
1.148	1.375	3.1×10^{-11}
1.148	0.621	3.4×10^{-10}
0.647	0.691	6.9×10^{-10}
0.895	1.031	7.3×10^{-11}
1.017	0.637	8.9×10^{-11}
0.637	0.412	9.2×10^{-11}
0.451	0.559	9.7×10^{-10}
0.591	0.405	6.1×10^{-10}
0.394	0.276	1.0×10^{-09}
0.118	0.141	3.5×10^{-09}

Table 4.1: Actual Fisher and Zwart (1996) data

σ_v at start (MPa)	σ_v at end (MPa)	k (cm^2)
0.172	0.207	5.5×10^{-10}
2.130	2.380	5.0×10^{-14}
2.070	2.240	7.0×10^{-14}
2.100	2.410	5.0×10^{-14}
2.490	2.800	2.0×10^{-13}

Sims et al. (1996) conducted laboratory experiments to investigate the stress-dependent flow through fractured clay till. In their experiments, they took shallow buried clays (up to a depth of 16 meters) and found natural fracture planes within them. They measured the conductivities of clays in a flexible permeameter and found that the conductivities were in the range $1.\times10^{-07}$ to $1.\times10^{-08}$ cm/s which is on the order of magnitude as the clay matrix ($1.\times10^{-08}$ cm/s). Using the cubic law relationship (Witherspoon et al., 1980) and the known residual flow volumes, they back calculated the fracture apertures and found that the equivalent hydraulic apertures were in the range of zero to 5 um.

Based on this, in our asperity model we assign the maximum crack aperture (W_o) for a clay to 10 um. The fractional contact area (f_c) is assigned to 4.65×10^{-05}. Gangi (1978) has reported that to match Nelson's (1975) data for fractures in sample sandstones, the contact area is about 4 % of the total fracture wall and to match Jones' (1975) data for fractures in carbonate rocks, the fractional contact area (f_c) is much

less than 4 % (f_c « 4 %). Based on this knowledge and in order to scale our asperity model, we assign a small fractional contact area (f_c) which is on the order of 1×10^{-05} of the total fracture wall.

The fracture spacing (s) is varied. The spacing is commonly much greater than the individual aperture of the fractures. In order to study and to scale the model, we choose fracture spacings that have one and two orders of magnitude higher than the values of the maximum crack aperture. Fracture spacings of 100 and 1000 *um* are used. Table 4.2 shows the parameters we use for our asperity model.

Table 4.2 : Parameters used by asperity model when spacing are varied

fixed parameters			matching parameters
E *MPa*	W_o *um*	f_c	s *um*
1.8×10^{04}	10	4.65×10^{-05}	100
1.8×10^{04}	10	4.65×10^{-05}	1000

The comparisons of measured and modeled bulk permeability versus the axial stress between our model and Fisher and Zwart's (1996) data are shown in Figure 4.5. Through the study we observe that by adjusting fracture spacing, the asperity model can match both Fisher and Zwart's (1996) data and their correlation. We observe that by increasing the spacing (s), the fracture permeability for a given axial stress decreases. This is expected since the fracture permeability is inversely proportional to the fracture spacing. In Figures 4.6 and 4.7, we investigate the behavior of the modeled

bulk permeability as we vary the fractional contact area (f_c) and the maximum crack aperture (W_o).

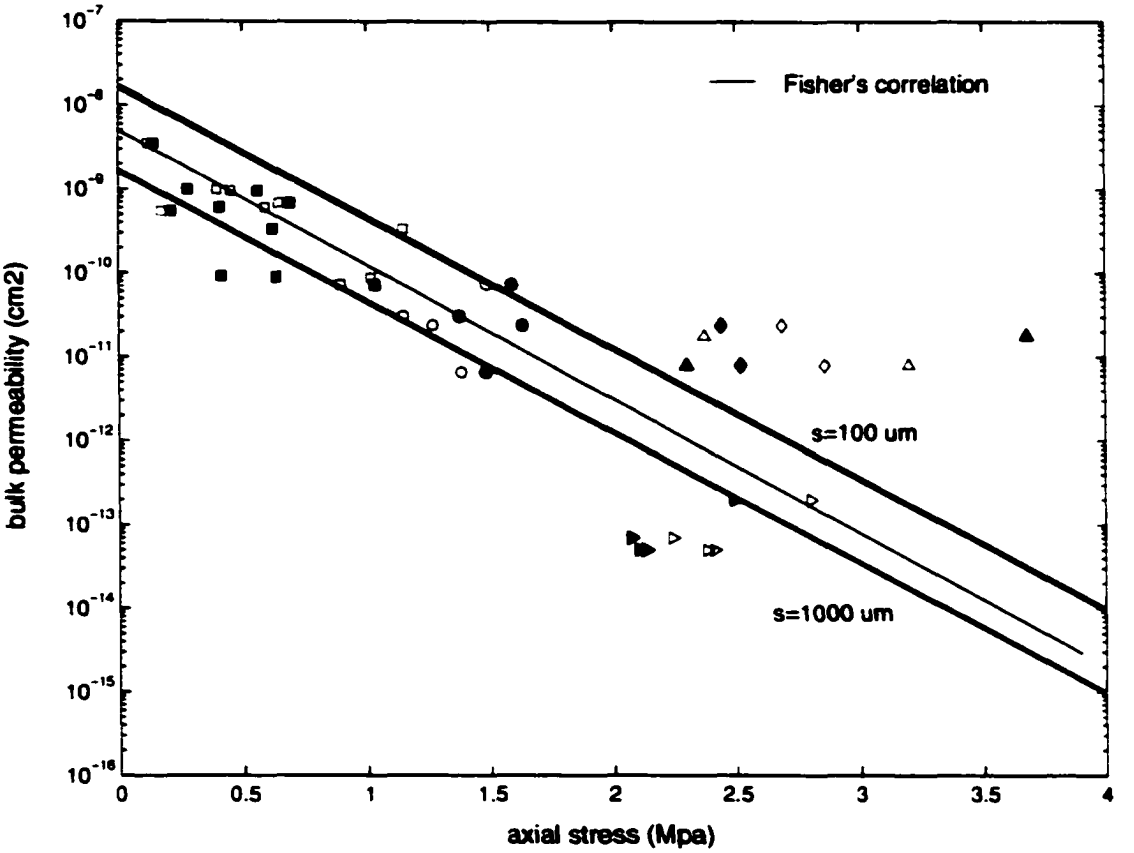

Figure 4.5: Comparison of measured and modeled bulk permeability vs. axial stress for different fracture spacings (s) (see caption of Figure 4.4).

Figure 4.6 shows the behavior of the modeled bulk permeability as we vary the fractional contact area (f_c). It can be seen that as the fractional contact area (f_c) increases, the modeled bulk permeability for a given axial stress also increases. The fracture spacing for this study is fixed and equal to 1000 um.

Table 4.3: Parameter used by asperity model when fractional contact area are varied

fixed parameters			matching parameters
E MPa	W_o um	s um	f_c
1.8×10^{04}	10	1000	2.2×10^{-05}
1.8×10^{04}	10	1000	4.6×10^{-05}
1.8×10^{04}	10	1000	6.7×10^{-05}

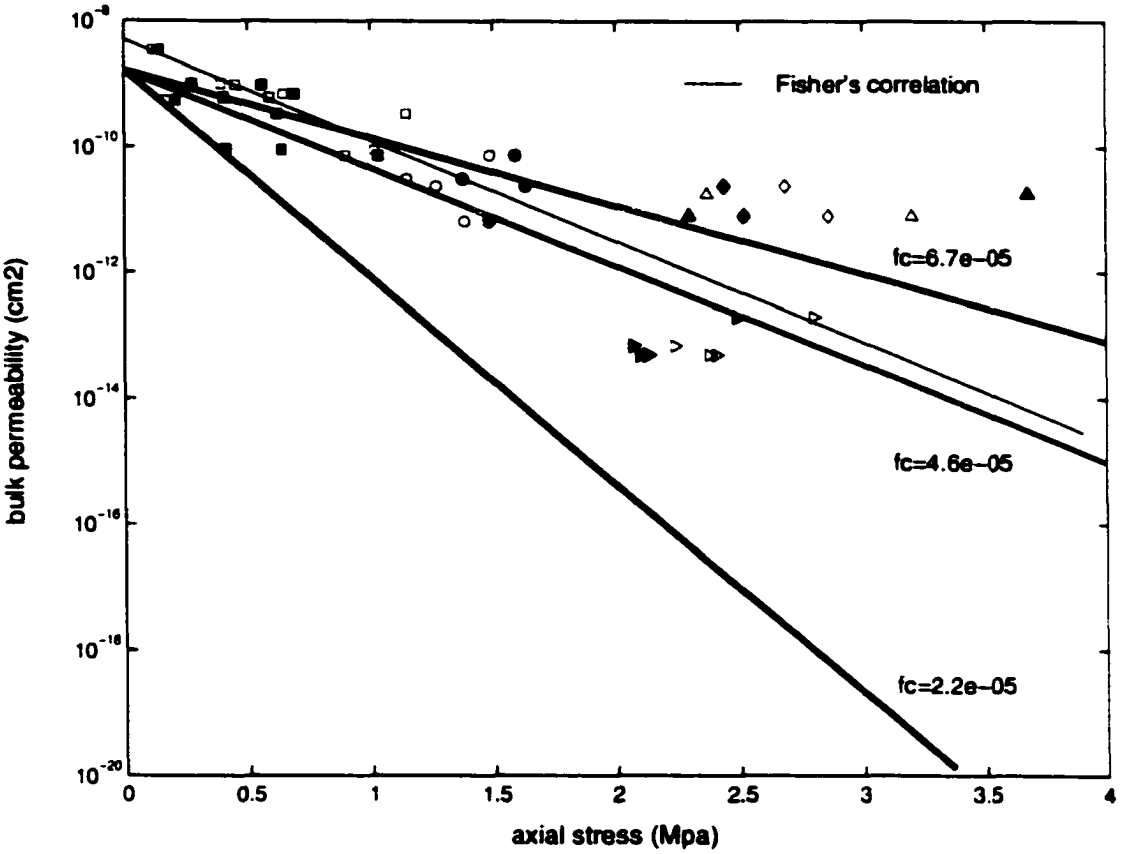

Figure 4.6: Comparison of measured and modeled bulk permeability vs. axial stress for different fractional contact areas (f_c) (see caption of Figure 4.4).

Figure 4.7 shows the behavior of the modeled bulk permeability as we vary the maximum crack aperture. We observe that as the maximum crack aperture increases, the bulk permeability increases. This is expected since the permeability is a function of the fracture aperture thus as the fracture aperture increases, the bulk permeability must also increase. The fracture spacing for this study is fixed at 1000 um.

Table 4.4: Parameter used by asperity model when crack aperture are varied

fixed parameters			matching parameters
E MPa	f_c	s um	W_o um
1.8×10^{04}	4.65×10^{-05}	1000	5
1.8×10^{04}	4.65×10^{-05}	1000	10

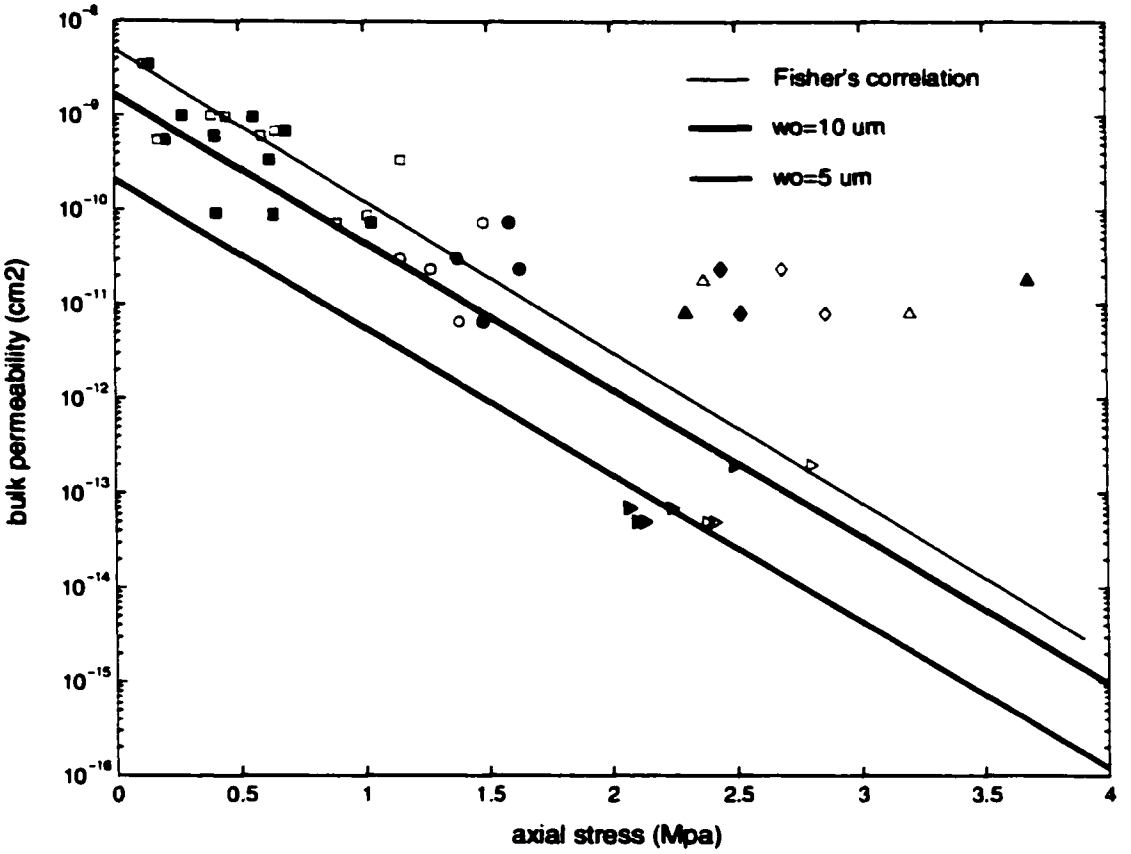

Figure 4.7: Comparison of measured and modeled bulk permeability vs. axial stress for different maximum crack apertures (W_o) (see caption of Figure 4.4).

Chapter 5

Steady-State model

We now combine our mechanical and hydraulic fracture models to evaluate hydrocarbon migration. We begin by developing a 1-D, analytical steady-state model of vertical hydrocarbon migration. This simple model describes single and two-phase steady-state flow through a fractured caprock and predicts the resulting hydrocarbon height in the underlying reservoir sand. In this model, we investigate a case where a potential reservoir is being charged from below by water and gas. Our purpose is to simulate flow due to the compaction of hydrocarbon expulsion from underlying source rocks (Figure 5.1).

In this model, water is injected into a reservoir to simulate flow from the underlying sediments and gas is injected to simulate hydrocarbon migration from underlying source rocks. We assume that there are pre-existing fractures in the seal due to tectonic and fluid stresses.

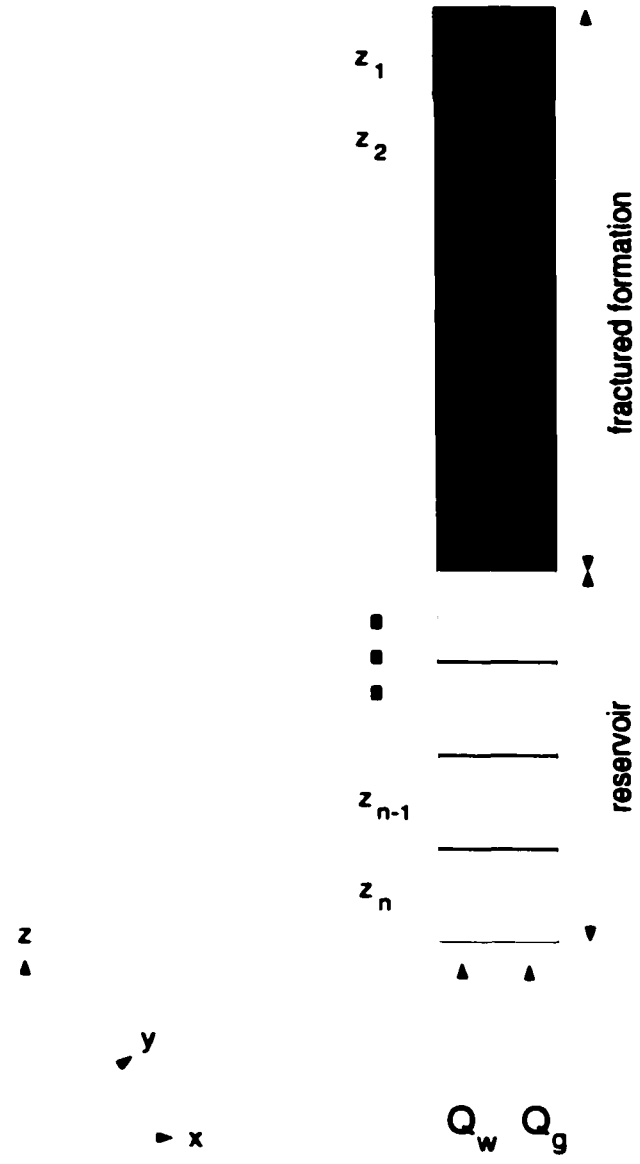

Figure 5.1: Physical representation of the 1-D system. The system is designed to have two different formations: a low permeability fractured caprock and a high permeability reservoir.

In Chapters 3 and 4, we developed mechanical and hydraulic models for rocks containing tensile fractures. We then calibrated those models with experimental data for soft rock. We now insert the asperity model into a hydrocarbon migration model by starting with the 1-D form of Darcy's equation for vertical flow:

$$q_l = \frac{-k_z A_z}{\mu_l}\left(\frac{dp_l}{dz} - \rho_l g\right) \tag{5.1}$$

where q_l is the fluid flow rate, k_z is the bulk rock permeability, A_z is the cross-sectional area which is perpendicular to the flow, μ_l is the fluid viscosity, ρ_l is the fluid density, dp_l/dz is the vertical fluid pressure gradient with z vertical, positive downward and g is the constant of gravity.

5.1 One-dimensional, single-phase (water) fracture flow development

We solve the single-phase problem by applying a finite-difference approximation to Eqn. 5.1. The discretized form of the equation for flow between two adjacent blocks is:

$$q_w = \frac{-k_z A_z}{\mu_w}\left(\frac{p_{w_i} - p_{w_{i+1}}}{z_i - z_{i+1}} - \rho_w g\right) \tag{5.2}$$

where i and $i+1$ are the block indexes.

Evaluating Eqn. 5.2, we have ten terms (q_w, k_z, A_z, μ_w, p_{w_i}, $p_{w_{i+1}}$, z_i, z_{i+1}, ρ_w, and g). The value of A_z, z_i and z_{i+1} are given as a function of the system geometry. The gravitational constant (g) is given and assumed constant. The volumetric flow rate (q_w) is an input variable. That leaves us with five unknowns and one equation. We enter PVT data from standard correlations to relate μ_w and ρ_w to p_w, leaving us with five unknowns and three equations. Using the models we have developed in Chapters 3 and 4, we can relate k_z and minimum horizontal effective stress σ_{hmin}. We have

added one equation ($k_z = f(\sigma_{hmin})$) but also another unknown σ_{hmin}. We assume that S_{hmin} is a function of depth (z) as follows:

$$S_{hmin} = \beta z \tag{5.3}$$

and assign a constant value to β and take z from the system geometry. We now have five unknowns and four equations.

We want to solve for all values of p_{w_i} for $i = 1 \ldots n$. We do this by assuming that the pressure at the top of the fractured formation (p_{w_1}) equals hydrostatic pressure, and then solve for p_{w_i} for $i = 2 \ldots n$.

Since k_z, μ_w, and ρ_w are all function of p_{w_i}, we must solve Eqn. 5.2 iteratively. This is accomplish by a bisection technique where an initial guess value of $p_{w_i}^{\circ}$ is determined by taking a value half way between $p_{w_{i-1}}$ and S_{hmin}. Values of k_z, μ_w, and ρ_w are then determined from $p_{w_i}^{\circ}$. We solve q_w and compare to the given q_w. If q_w is greater than the given value, $p_{w_i}^{\circ}$ becomes our new upper bound and we bisect the range from $p_{w_{i-1}}$ to $p_{w_i}^{\circ}$. Conversely if the calculated value of q_w is less than the given value, we set $p_{w_i}^{\circ}$ as the lower bound and bisect the range from $p_{w_i}^{\circ}$ to S_{hmin}. We re-calculate k_z, μ_w, and ρ_w. We then calculate q_w and continue the process until the change in the value of $p_{w_i}^{\circ}$ is within some error limit. We then step to the next block, continuing until all n values of p_w have been determined.

We now examine the behavior of a fractured caprock in response to water expulsion from below. We inject water with two different flow rates (low and high flow rates). Water density assigned at standard condition is 67 $lb/cu \cdot ft$. The system is divided into two different formations (caprock and reservoir). From −8950 to −10050 ft depth is the caprock and from −10050 to −11050 ft depth is the reservoir. Water is injected into the bottom of reservoir. For low-rate case, we inject 1.0×10^{-09} $STB/D \cdot ft^2$ water into a system and 1.0×10^{-06} $STB/D \cdot ft^2$ for high-rate case. The gradient of the least principal stress S_{hmin} is assigned a value of 0.8 psi/ft.

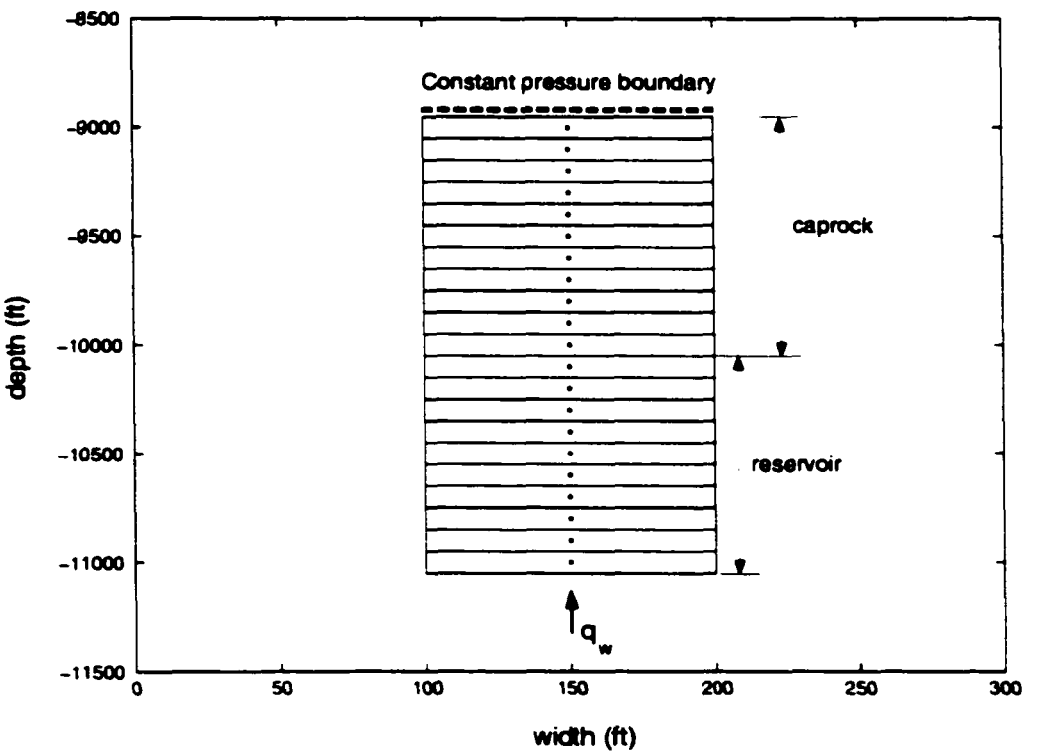

Figure 5.2: Physical representation of 1-D system describing finite-difference gridding and boundary condition.

The rates of secondary migration are poorly known, however it is presumed extremely variable with estimates ranging from a few meter per thousand years to a kilometer per thousand years (England and Fleet, 1991). These rates depend partly on the rates at which hydrocarbon (petroleum) is generated. Laboratory experiments (Thomas and Clouse, 1995) with glass columns packed with water-saturated sand or glass beads where oil was supplied at the base and allowed to rise buoyantly suggest that migration is highly efficient and that migration rates are high, as much as 50 cm per hour. However, we must be cautious in extending experimental results to actual migration processes. If those high rates are applicable to actual hydrocarbon migration then the secondary migration process would be nearly instantaneous.

In sedimentary sequences, actual migration rates are much lower than those in experiments. The sedimentary sequences tends to be heterogeneous caused by compaction. This affects permeability and pore entry pressure. England et al. (1987) have estimated the rates of migration from rock and petroleum properties. They concluded that the rates are small and in order of $1\times10^{-07}\ STB/D\cdot ft^2$.

Figure 5.3 shows the results of the study. The reservoir pressure gradient is nearly hydrostatic for both cases due to the high permeability and low flow rate. The figure also shows a direct correlation between water flux and pressure. As the water flux increases, pressure in the system increases. Recall Eqn. 5.2, the only variables that can change to affect a higher q_w are k_z and Δp. Near the upper boundary of the caprock where the pressure is set to hydrostatic, the curvature of the pressure field or the vertical change in the pressure gradient is large. In this zone, the minimum horizontal effective stress ($\sigma_{hmin} = S_{hmin} - \alpha p_w$) and the pressure gradient (dp_w/dz) both increase upward. Beneath this boundary layer effect, the pressure gradient parallels the least principle stress and there is little curvature in the pressure field. The greater the flow rate, the closer the pressure is to the least principle stress.

The pressure profile near the caprock and sand interface is shown in Figure 5.4. In the figure, σ_1 and σ_2 represent the effective stresses for each case. For a caprock, the permeability depends on the effective stress (σ_{hmin}) thus the smaller the effective stress, the larger the permeability. The permeability of reservoir is constant and equal to 3 md. The fracture spacing in a caprock is assigned to 1000 um. Fracture parameters and the flow-rates used in this study are tabulated in Tables 5.1 and 5.2.

Table 5.1: Parameters for fracture permeability model.

Spacing (s) um	Maximum asperity length (W_o) um	Fractional contact area (f_c)
1000	10	4.6×10^{-05}

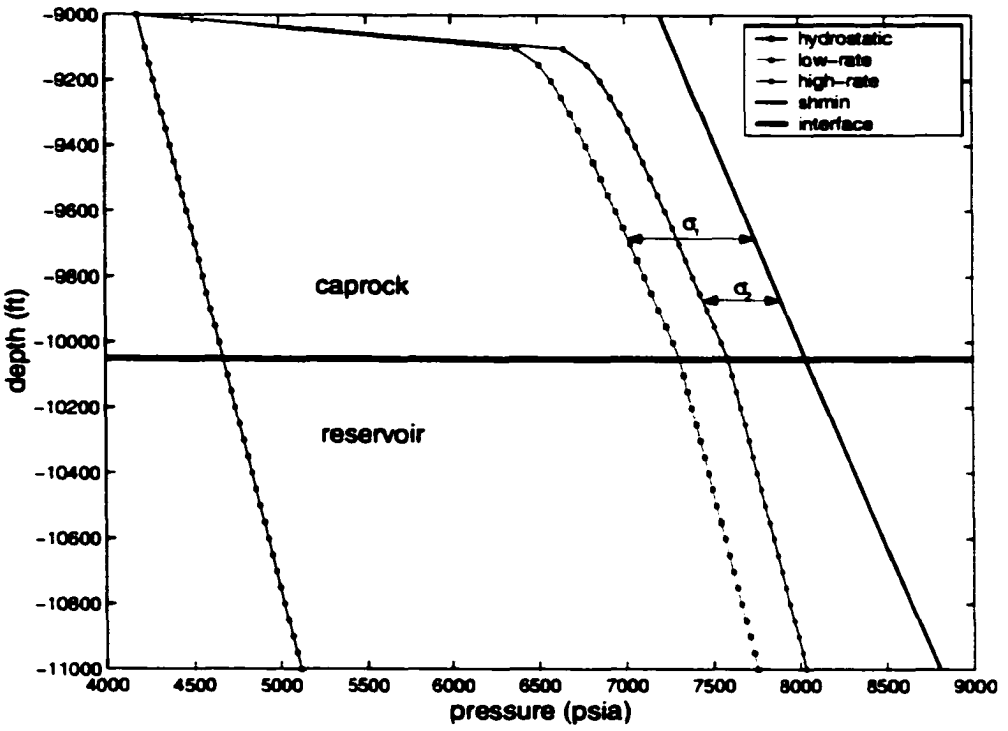

Figure 5.3: Predicted pressure across a caprock and reservoir in 1-D, single-phase system.

Table 5.2: Flow-rates used in 1-D, single-phase flow model.

Case type	Water injection rate at reference depth (q_w) $STB/D \cdot ft^2$ [a]
low rate	1.0×10^{-09}
high rate	1.0×10^{-06}

a. reference depth is at $-9000\ ft$

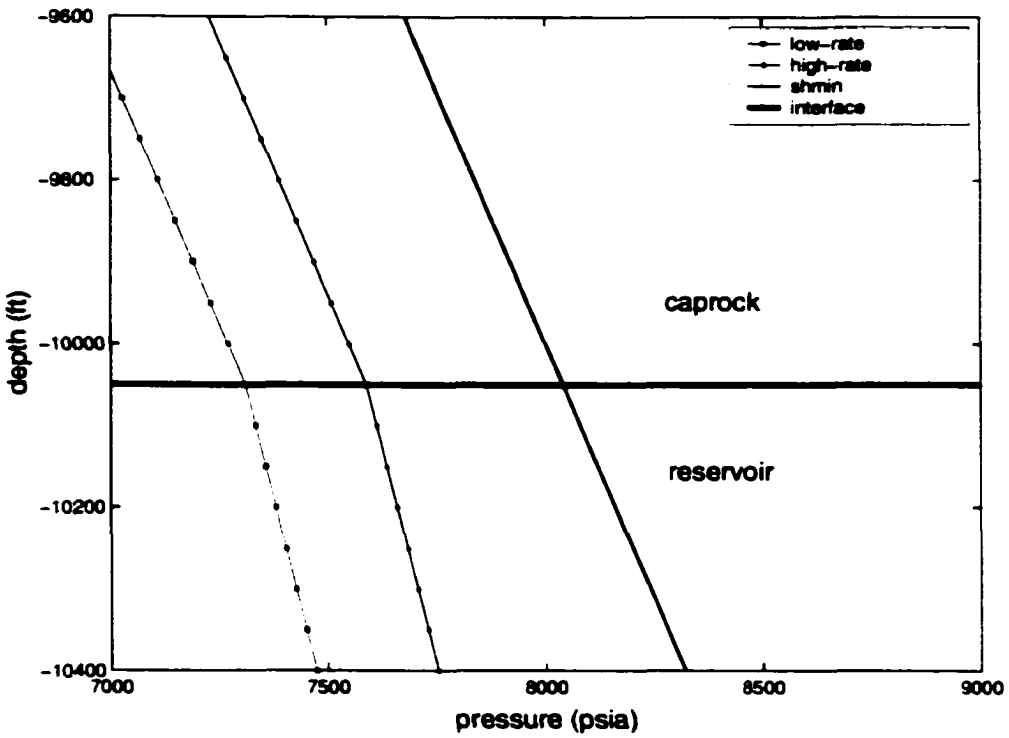

Figure 5.4: Predicted pressure near the interface of a caprock and reservoir in 1-D, single phase system.

5.2 One-dimensional, two-phase fracture flow development

In the 1-D, steady-state, two-phase model, we apply a finite-difference approximation to Eqn. 5.1 and add a relative permeability term (k_{r_l}).

water:

$$q_w = \frac{-k_{\sim} k_{r_w} A_{\sim}}{\mu_w}\left(\frac{P_{w_i} - P_{w_{i+1}}}{z_i - z_{i+1}} - \rho_w g\right) \tag{5.4}$$

gas:

$$q_g = \frac{-k_z k_{r_g} A_z}{\mu_g}\left(\frac{p_{g_i} - P_{g_{i+1}}}{z_i - z_{i+1}} - \rho_g g\right) \tag{5.5}$$

where k_{r_w} and k_{r_g} are the relative permeabilities for water and gas, respectively.

Evaluating Eqn. 5.4 and 5.5, we have seventeen terms. The values of A_z, z_i and z_{i+1} are taken from the system geometry. The gravitational constant (g) is given and assumed to be constant. The volumetric flow rates (q_w and q_g) are input variables. That leaves us with eleven unknowns and two equations. We enter PVT data from standard correlation to relate μ_w and ρ_w to p_w and μ_g and ρ_g to p_g, leaving us with eleven unknowns and six equations. Using the relationship established in Chapters 3 and 4, we can determine permeability (k_z) and minimum horizontal effective stress (σ_{hmin}). We also can establish the relationships between relative permeability, water (k_{r_w}) and gas (k_{r_g}), to saturations. This relationships can be expressed as: $k_{r_w} = f(S_w)$ and $k_{r_g} = f(S_w)$. We have added four equations: (a) equation to relate k_z to σ_{hmin}; (b) equation to relate σ_{hmin} to p_w; (c) equation to relate k_{r_w} to S_w; (d) equation to relate k_{r_g} to S_w, leaving us with thirteen unknowns and ten equations

We also can obtain two more equations from saturation relationship and the relationship between gas and water pressure:

$$S_w + S_g = 1 \tag{5.6}$$

$$P_c = p_g - p_w \tag{5.7}$$

and one more equation that relates P_c to S_w:

$$P_c = f(S_w, \sigma_{hmin}) \tag{5.8}$$

We want to solve for all values of p_{w_i} and p_{g_i} for $i = 1 \ldots n$. Similar to 1-D, single-phase analytical model, we are assuming hydrostatic pressure at the top of the caprock (p_{w_1}) and then solving for p_{w_i} and p_{g_i} for $i = 2 \ldots n$.

Since k_z, μ_w, and ρ_w are all function of p_w, and μ_g and ρ_g are function of p_g, we must solve the equations iteratively. Similar to the single-phase model, this is accomplished by a bisection technique where an initial guess value of $p_{w_i}^{\circ}$ is determined by taking a value half way between $p_{w_{i-1}}$ and S_{hmin}. Values of k_z, μ_w, and ρ_w are then determined from $p_{w_i}^{\circ}$. Given water flow rate (q_w) and obtained k_z and water properties, the water relative permeability ($k_{r_{w_i}}$) can be obtained. Using the relationship $k_{r_w} = f(S_w)$, the saturation S_{w_i} is obtained. We use Eqn. 5.8 to determine capillary pressure and Eqn. 5.7 to determine gas pressure $p_{g_i}^{\circ}$. Based on $p_{g_i}^{\circ}$ we obtain gas properties and solve for gas flow rate (q_g) and compare to the given gas rate. If q_g is greater than the given gas rate value, $p_{w_i}^{\circ}$ becomes our new upper bound and we bisect the range from $p_{w_{i-1}}$ to $p_{w_i}^{\circ}$.

Conversely if the calculated value of q_g is less than the given value, we set $p_{w_i}^{\circ}$ as the lower bound and bisect the range from $p_{w_i}^{\circ}$ to S_{hmin}. We re-calculate k_z, μ_w, and ρ_w. We then calculate $p_{g_i}^{\circ}$ and obtain q_g and continue the process until the change in the value of $p_{w_i}^{\circ}$ is within some error limit. We then step to the next block, continuing until all n values of p_w and p_g have been determined.

5.2.1 Capillary pressure in the fractured caprock

Because we want to study two-phase flow, we need to explore the capillary pressure relationship between the two phases. Capillary pressure is the pressure difference between the two immiscible phases (gas and water) as shown in Eqn. 5.7. The molecular attraction between similar molecules in each fluid is greater than the attraction between molecules of the different fluids. This causes a curved interface to exist between the phases. The strength of these forces can be described in terms of the principal radii of curvature of the interface between the phases (Amyx et al., 1960):

$$P_c = \gamma\left(\frac{1}{r_1} + \frac{1}{r_2}\right) \tag{5.9}$$

where P_c is the capillary pressure, γ is the interfacial tension, r_1 and r_2 are the two principal radii of curvature of the interface between the phases.

In a parallel plate fracture of aperture w, principal radii of curvature of the interface between the phases are $r_1 = \frac{w}{2\cos\theta}$ and $r_2 = \infty$ (Pruess and Tsang, 1990). Therefore the capillary pressure equation shown in Eqn. 5.9 reduces to:

$$P_c = \frac{2\gamma\cos\theta}{w} \tag{5.10}$$

where w is the aperture and θ is the contact angle.

Eqn. 5.10 shows that capillary pressure depends on the aperture w. Thus when aperture w becomes smaller, the capillary pressure becomes higher. Eqn. 5.10 can also be seen as a displacement pressure or the pressure required to overcome the interfacial forces to force the non-wetting phase into aperture w to displace the wetting phase. We now construct capillary pressure functions for the fractured formation based on Eqn. 5.10. In Figure 5.5, $\sigma_{hmin} = 0\ MPa$ describes capillary pressure in fracture formation at the maximum fracture aperture. We assume that at the maximum aperture,

the minimum horizontal effective stress (σ_{hmin}) is zero. In addition to capillary pressure at zero effective stress, we calculate capillary pressure at different effective stress. Figure 5.5 shows that capillary pressure strongly depends on the aperture. At high effective stress, the aperture becomes small and the capillary pressure becomes high.

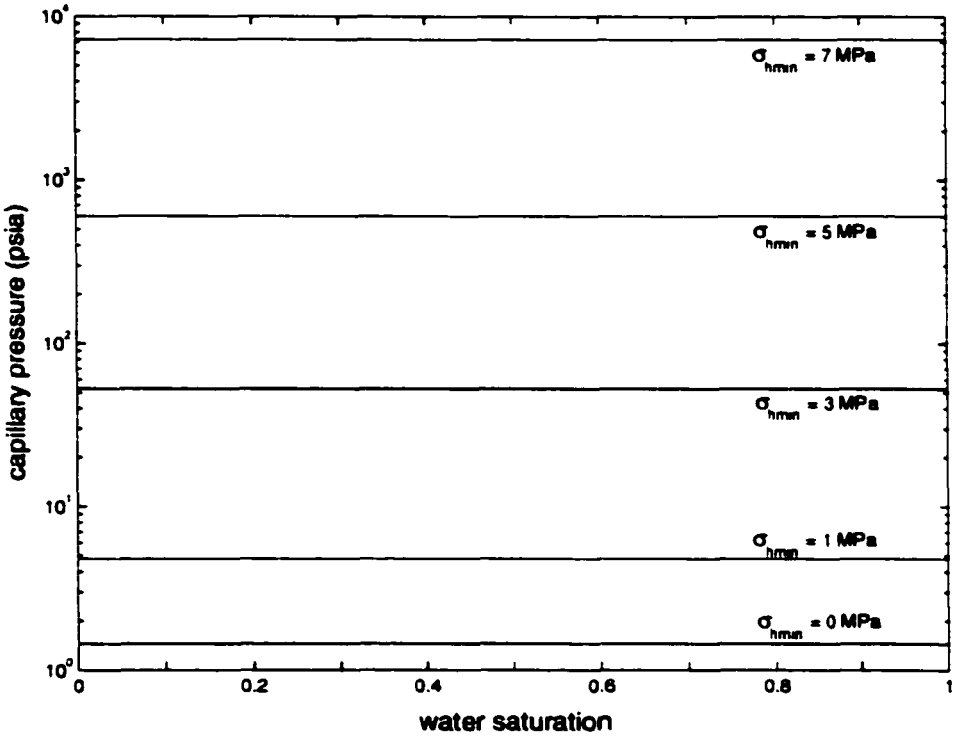

Figure 5.5: Variation of capillary pressure in a caprock at different effective stresses. Capillary pressure in a caprock depends on the effective stress. As the effective stress increases, the fracture width decreases and the capillary pressure increases.

5.2.2 Capillary pressure in the reservoir

We construct a capillary pressure-saturation function for the reservoir using Thomeer's (1960) equation. Thomeer (1960) expresses capillary pressure in terms of pore geometry and displacement pressure:

$$P_c = P_d \, 10^{\left(\frac{-G}{\ln\left(\frac{S_g}{1-S_{w_{irr}}}\right)}\right)} \tag{5.11}$$

where P_c is a capillary pressure, P_d is a displacement pressure, G is pore geometrical factor, S_g is gas saturation, and $S_{w_{irr}}$ is irreducible water saturation. Figure 5.6 describes this relationship for reservoir sand. The pore geometrical factor (G) is assigned to 0.3, the irreducible water saturation ($S_{w_{irr}}$) is assigned to 0.15, and the displacement pressure (P_d) is assigned to 5 psi.

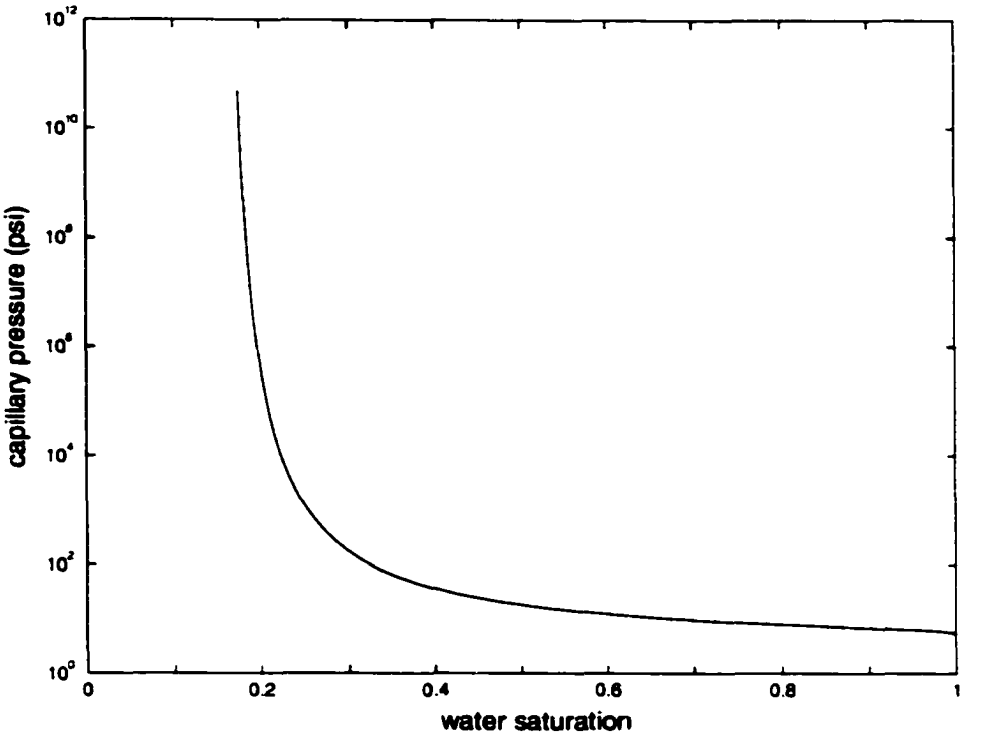

Figure 5.6: Capillary pressure in the reservoir. To generate the plot, Thomeer's equation is used with $G = 0.3$, $S_{w_{irr}} = 0.15$, and $P_d = 5$ psi.

5.2.3 Gas and Water relative permeability

In a smooth-walled fracture, it is usually assumed that neither phase interferes with the flow of the other. This assumption means that the sum of wetting (k_{r_w}) and non-wetting phase (k_{r_g}) relative permeability is equal to one. This assumption is based on the experimental work by Romm (1966) who used parallel plate fractures with surfaces of mixed wettability and also on analysis of field data (Pruess et al., 1984). However, theoretical analysis and numerical simulations of two-phase flow in fractures with a variable aperture by Pruess and Tsang (1990) show that significant phase interference

occurs in a rough fracture and $k_{r_w} + k_{r_g} \leq 1$. This was also confirmed by the experimental work of Persoff et al. (1991).

Persoff and Pruess (1995) measured relative permeability in natural rough walled fractures. Their measurements indicate a strong phase interference with relative permeability reduced to very small values at intermediate saturations for both wetting and non-wetting phases. Their results challenged a conventional view of fracture relative permeability that assumes relative permeability of each phase is equal to its saturation, but they are consistent with a recent model that views fractures as a two-dimensional heterogeneous porous media (Pruess and Tsang, 1990). Persoff and Pruess (1995) also make a comparison of experimental data and Corey's (1954) equation. They showed that Corey's (1954) equation can approximate the experimental data. Based on this literature study, we use Corey's (1954) equation to assign k_r as a function of S_w for both fractured and reservoir formations.

Corey's (1954) equation is given as:

$$k_{r_w} = \left(\frac{S_w - S_{w_{irr}}}{1 - S_{w_{irr}} - S_{g_{irr}}} \right)^4 \tag{5.12}$$

$$k_{r_g} = \left[1 - \left(\frac{S_w - S_{w_{irr}}}{1 - S_{w_{irr}} - S_{g_{irr}}} \right)^2 \right] \left[1 - \frac{S_w - S_{w_{irr}}}{1 - S_{w_{irr}} - S_{g_{irr}}} \right]^2 \tag{5.13}$$

where k_{r_w} and k_{r_g} are water and gas relative permeability, S_w and S_g are water and gas saturations, and $S_{w_{irr}}$ and $S_{g_{irr}}$ are water and gas irreducible saturations.

Figures 5.7 and 5.8 show the water (k_{r_w}) and gas (k_{r_g}) relative permeability functions assigned to the sand and shale formations. $S_{w_{irr}}$ for the sand is set to 0.15 and $S_{g_{irr}}$ is set to 0.02. For the shale, $S_{w_{irr}}$ and $S_{g_{irr}}$ are set to 0 and 0.02, respectively.

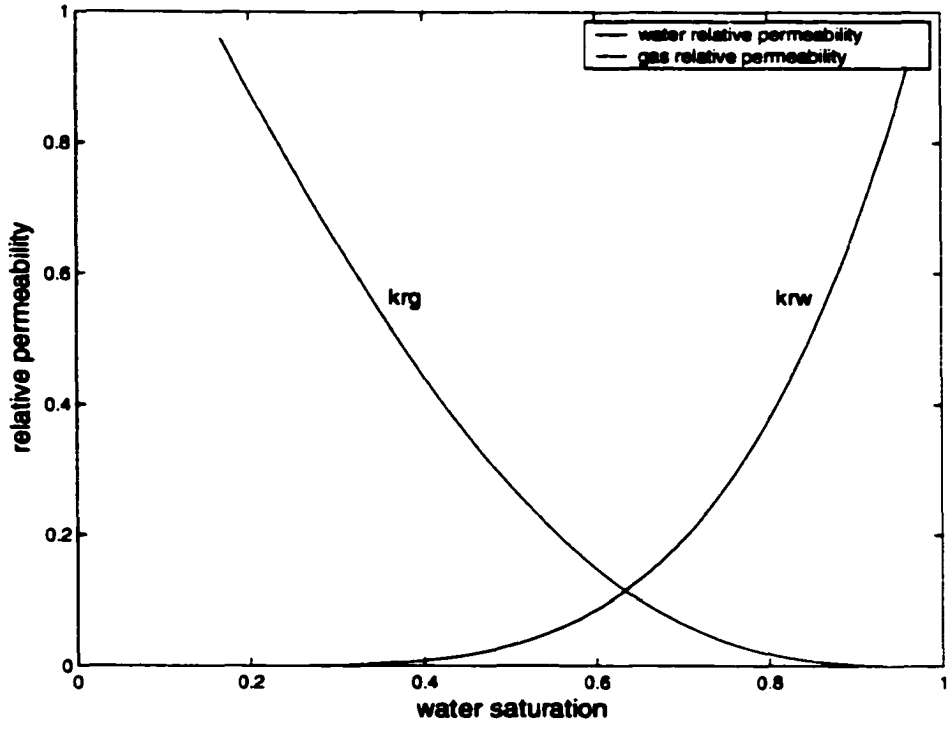

Figure 5.7: Water and gas relative permeability in the reservoir. To generate the figure, Corey's equation is used with $S_{w_{irr}} = 0.15$ and $S_{g_{irr}} = 0.02$.

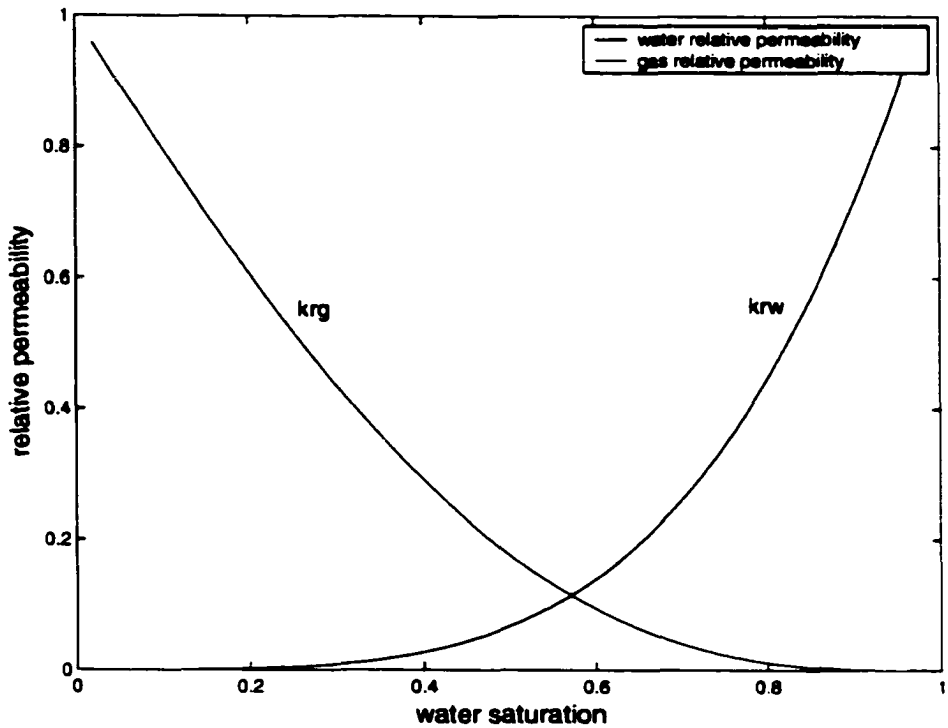

Figure 5.8: Water and gas relative permeability in a caprock. To generate the figure, Corey's equation is used with $S_{w_{irr}} = 0.$ and $S_{g_{irr}} = 0.02$.

We now simulate 1-D, two-phase steady-state flow. In a single-phase, we use two different flow rates to study flow through the fractures, however in a two-phase flow we only use one flow rate. Figure 5.9 shows the predicted pressures.

Water and gas are injected into the base of the reservoir. A low injection rate given in Table 5.3 is used. Boundary conditions for the system are hydrostatic pressure in the water phase at the top of the caprock and constant water and gas fluxes at the base of the reservoir. Fracture permeability is generated using fracture spacing of 1000 um.

Table 5.3: Flow-rates used in 1-D, two-phase flow model.

Water injection rate $STB/D \cdot ft^2$	Gas injection rate $SCF/D \cdot ft^2$	Gas injection rate at reference depth[a] $STB/D \cdot ft^2$
1.0×10^{-09}	1.0×10^{-04}	5.7×10^{-08}

a. reference depth is at $-9000\ ft$.

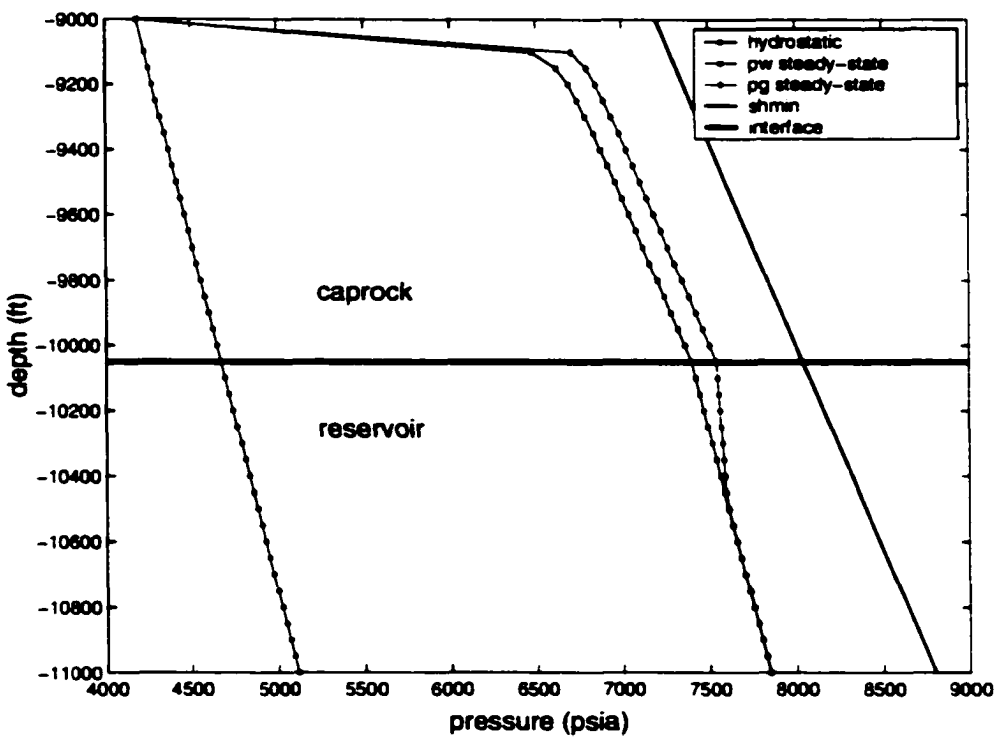

Figure 5.9: Predicted pressure across a caprock and reservoir in a 1-D, two-phase system.

Predicted pressures near the interface of a caprock and reservoir are given in Figure 5.10. In the figure, the gas column height measured from the GWC (gas water contact) to the interface between a caprock and reservoir is shown.

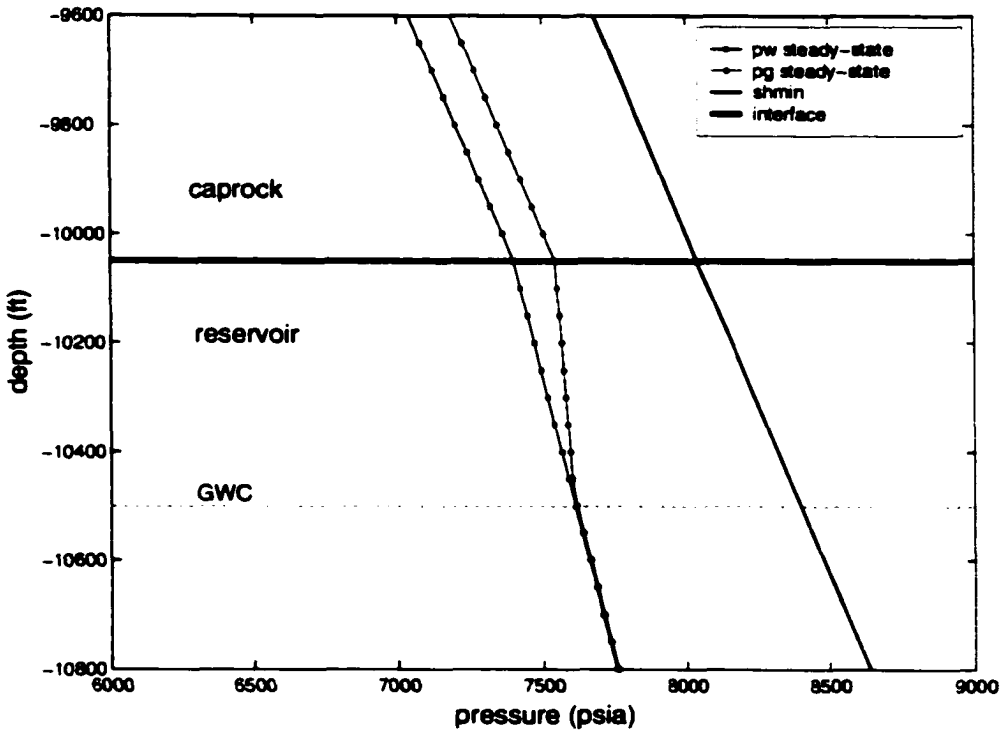

Figure 5.10: Predicted pressures near the interface of a caprock and reservoir in 1-D, two-phase system. In the figure, GWC represents the gas-water contact at steady-state.

Figure 5.11 shows saturation within the caprock and the reservoir. For the low rate case, gas is trapped in the reservoir as recorded by high gas saturations. This is expected due to the small fracture width in the caprock.

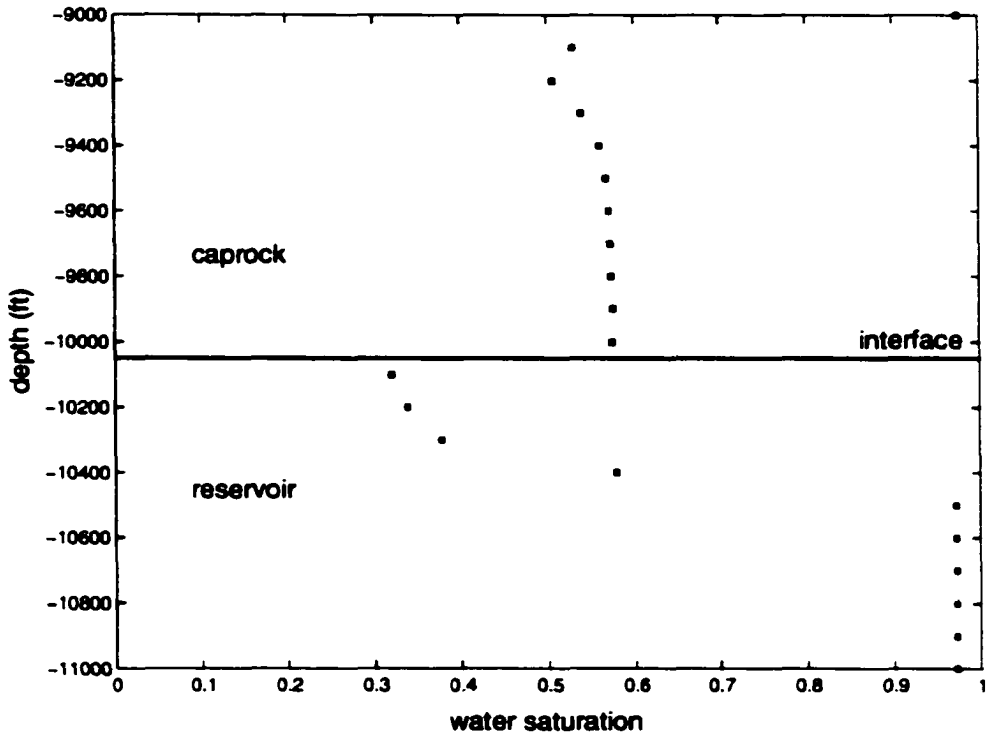

Figure 5.11: Predicted water saturation across a caprock and reservoir in 1-D, two-phase system.

5.2.4 Understanding system behavior

We now extend the study by injecting several different water rates (q_w) into the system while keeping the gas injection rate (q_g) constant. Our purpose is to investigate the effect of water flux on the gas column height.

Figure 5.12 shows the results of the study. In this study, water injection rates are varied while the gas rate is kept constant at $1\times10^{-04}\ SCF/D\cdot ft^2$. The change of water rate has a drastic effect on gas column height. At a small water injection rate, the gas column is large due to a small fracture width. As discussed previously, fracture width in a caprock depends strongly on the effective stress. At small water injection rate, the effective stress is high and the fracture width is small.

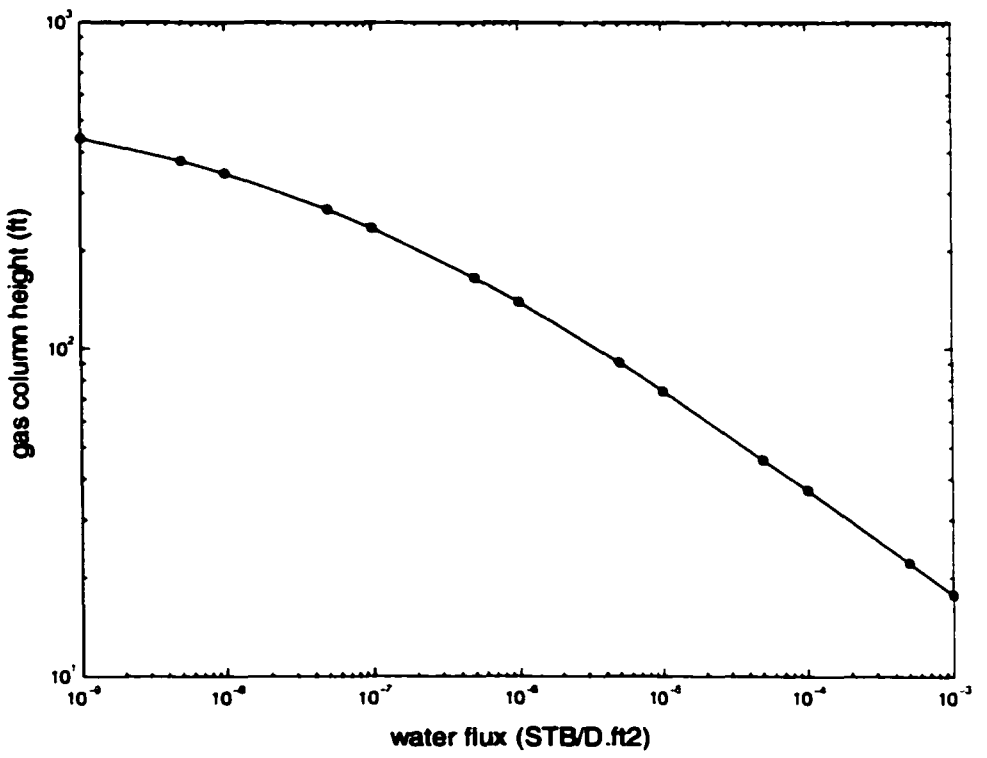

Figure 5.12: Gas column as a function of water flux at a constant gas rates.

Figure 5.13 shows the effect of varying the ratio of injection rates Q_g/Q_w, while maintaining a constant total injection rate, on gas column height. Total injection rate at a reference depth of -9, 000 ft is maintained at 5.0×10^{-08} $RB/D\cdot ft^2$. By increasing gas flow rate and keeping total flow rates constant, we have reduced the water injection rate. Thus at this low water injection rate, the effective stress at the interface is high and hydraulic fracture width is small. We observed this phenomenon in the previous study. The results of this phenomenon is the large gas column height in the reservoir.

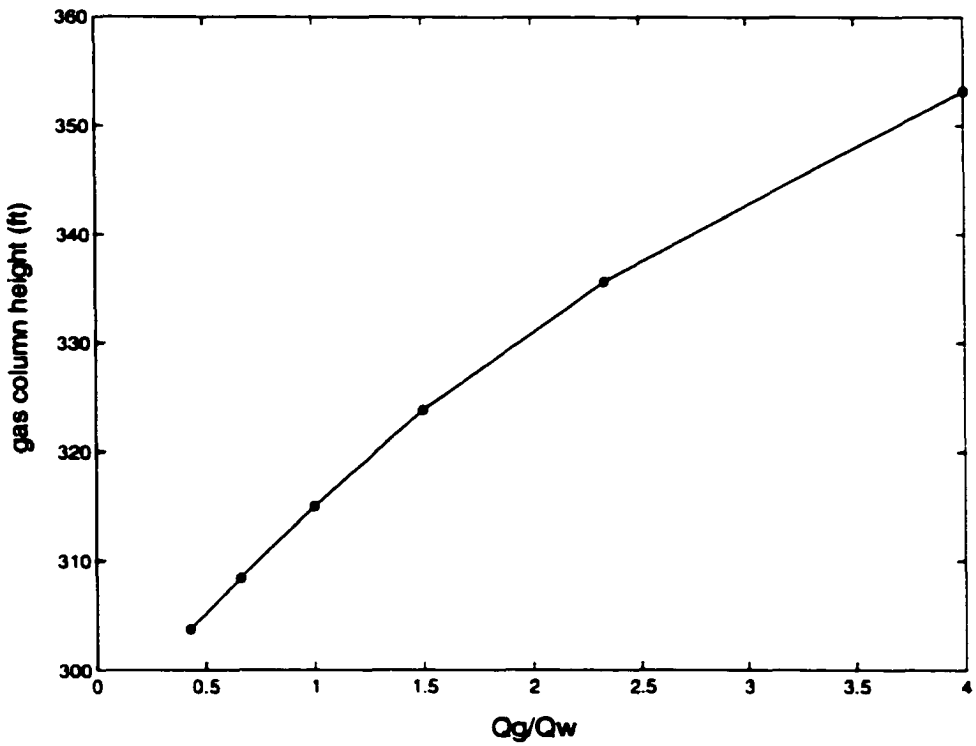

Figure 5.13: Gas column as a function of ratio injection rates at a constant total flux.

We now study the case where we vary total flow rates and keep the ratio of injection rates Q_g/Q_w constant. We study the influence of changing total flow rates on the gas column height. In this study, the ratio of gas to water injection rate at reference depth $-9,000\ ft$ is assigned to be equal to 45. Figure 4.14 shows that as we lower total injection rate, the gas column height increases. This is expected since at low total injection rate, the hydraulic fracture width is small because of the high effective stress. We also observe that even small increases in total charge rate greatly reduce the ability of the caprock to trap hydrocarbon for the 1-D case.

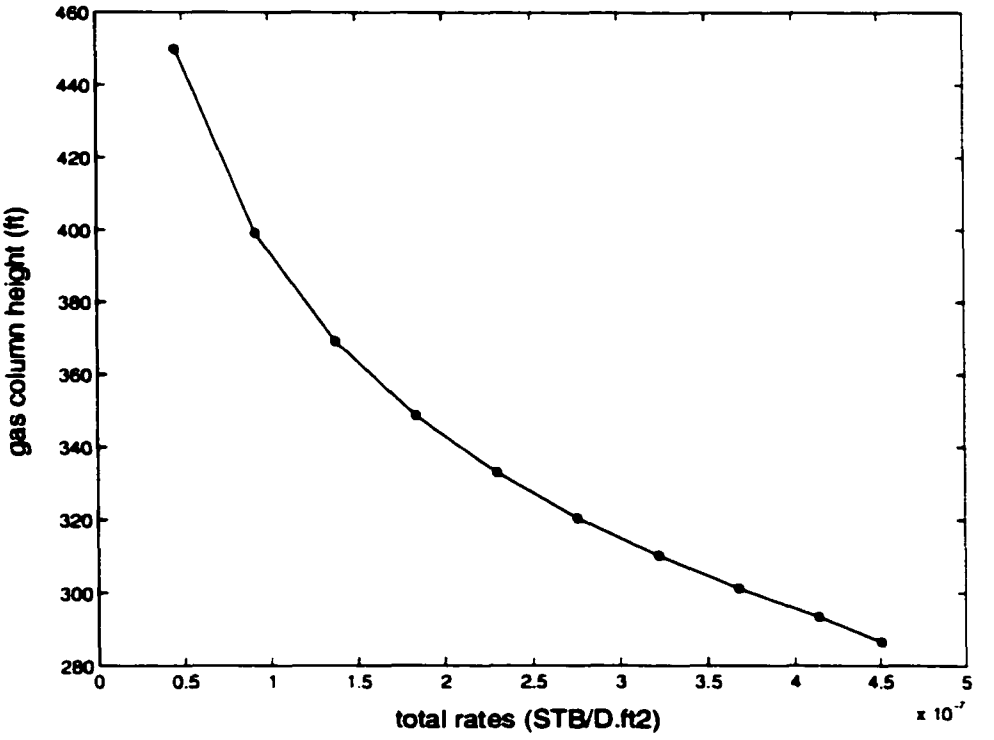

Figure 5.14: Gas column as a function of total flux at a constant Q_g/Q_w.

5.2.5 Parametric study (varying fracture spacing)

We now study the effect of varying fracture spacing on the pressure build-up in the underlying reservoir and gas column height. In this study we consider the spacing that have one and two order of magnitude greater than the maximum asperity height. Table 5.4 summarizes the input parameters for fracture permeability model.

Table 5.4: Parameters for fracture permeability.

Spacing (s) um	Maximum asperity length (W_o) um	Fractional contact area (f_c)
100	10	4.65×10^{-05}
1000	10	4.65×10^{-05}

5.2.5.1 Varying fracture spacing in a single-phase system

Figure 5.15 shows the results of single-phase flow. Water is injected into the bottom of the reservoir. The 1-D system is shown in Figure 5.1. Two different injection rates are used (low and high-rate) to study the effect of varying the spacing. The rates are tabulated in Table 5.2 (Section 5.1).

We observe that by reducing the spacing from 1000 to 100 um, the pressure build-up in the reservoir at steady-state reduces. This indicates that as the spacing decreases, the effective stress (σ_{hmin}) increases. Since the width of the fracture depends on the σ_{hmin}, the increase of σ_{hmin} results in a decrease in the fracture width.

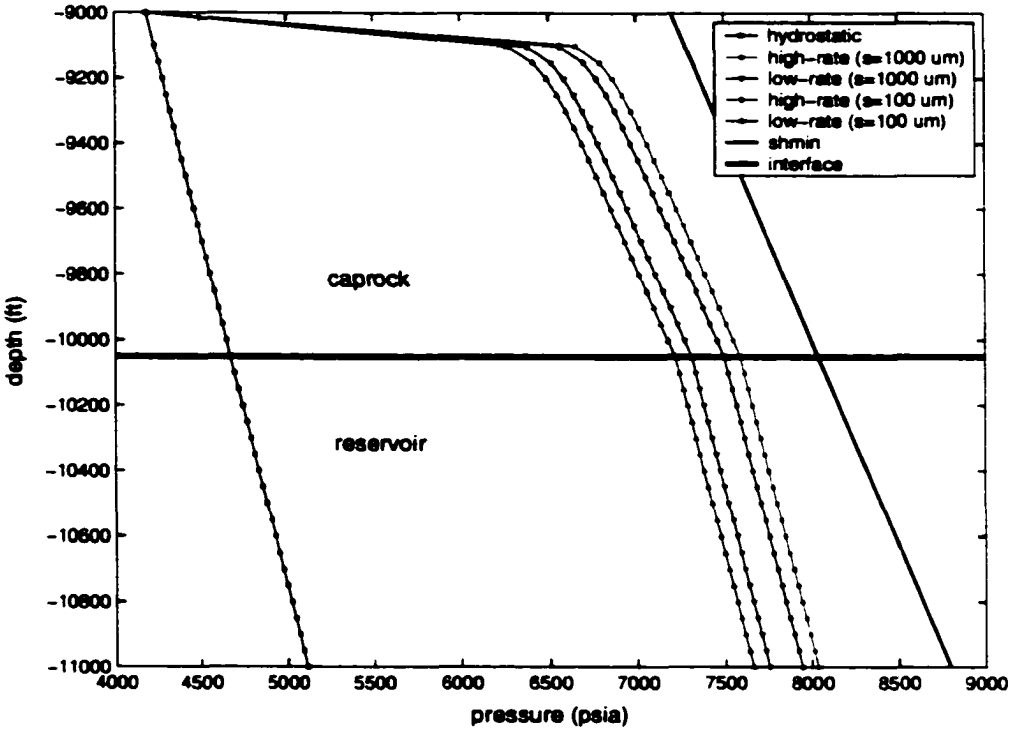

Figure 5.15: Predicted pressure across a caprock and reservoir for 1-D, single-phase system. In this study, two different fracture spacings (s) with two different injection rates are considered. Parameters for fracture permeability model and the rates are given in Tables 5.2 and 5.4.

5.2.5.2 Varying fracture spacing in a two-phase system

Figure 5.16 and 5.17 show the results for two-phase flow. Water and gas are injected into the bottom of the reservoir simultaneously. Table 5.3 summarizes the rates used. Similar to a single-phase case, we observe that the pressure build-up in the reservoir decreases as the spacing decreases. As discussed previously, the capability of the caprock to trap gas depends strongly on the fracture width. At small fracture widths, the gas columns are large. When the pressure build-up decreases as we decrease the spacing from 1000 to 100 um, the effective stress increases. This increase in effective stress results in an increase in the gas column heights in the reservoir.

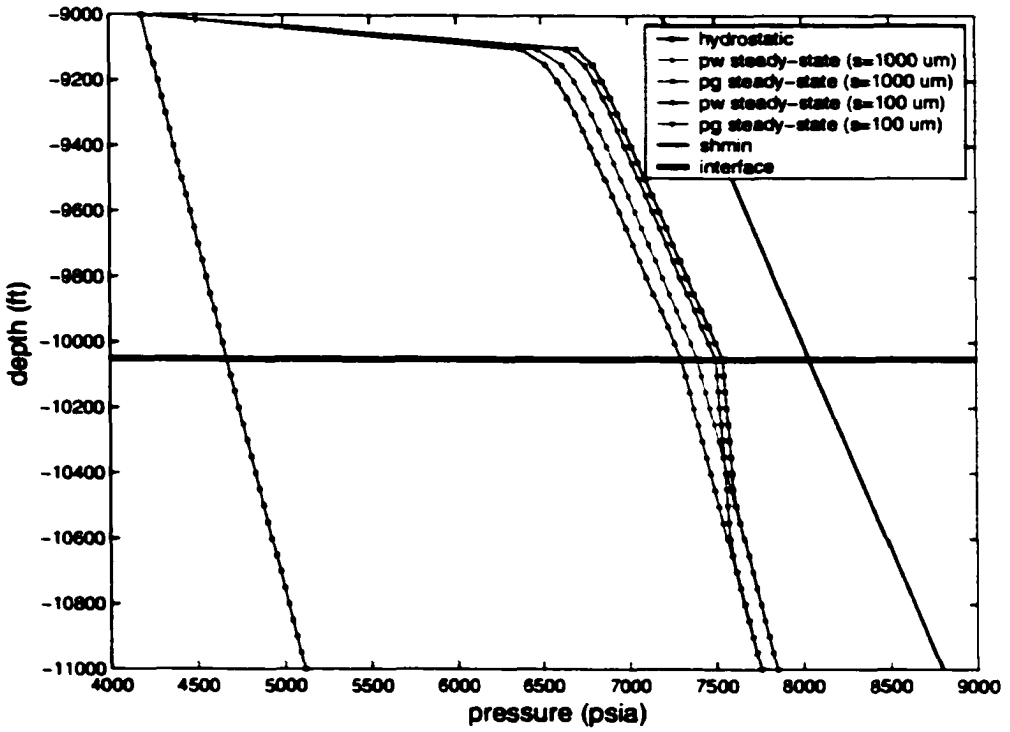

Figure 5.16: Predicted pressure across a caprock and reservoir for 1-D, two-phase system. In this study, two different spacings (s) are used. Parameters for fracture permeability model and the rate are given in Tables 5.3 and 5.4.

Figure 5.17 shows the predicted pressure near the interface of a caprock and reservoir. In the figure, gas column heights measured from gas-water contact to the interface of a caprock and reservoir are shown. The values of gas column heights are given in Table 5.5. It can be seen that as the spacing decreases, the gas column height increases.

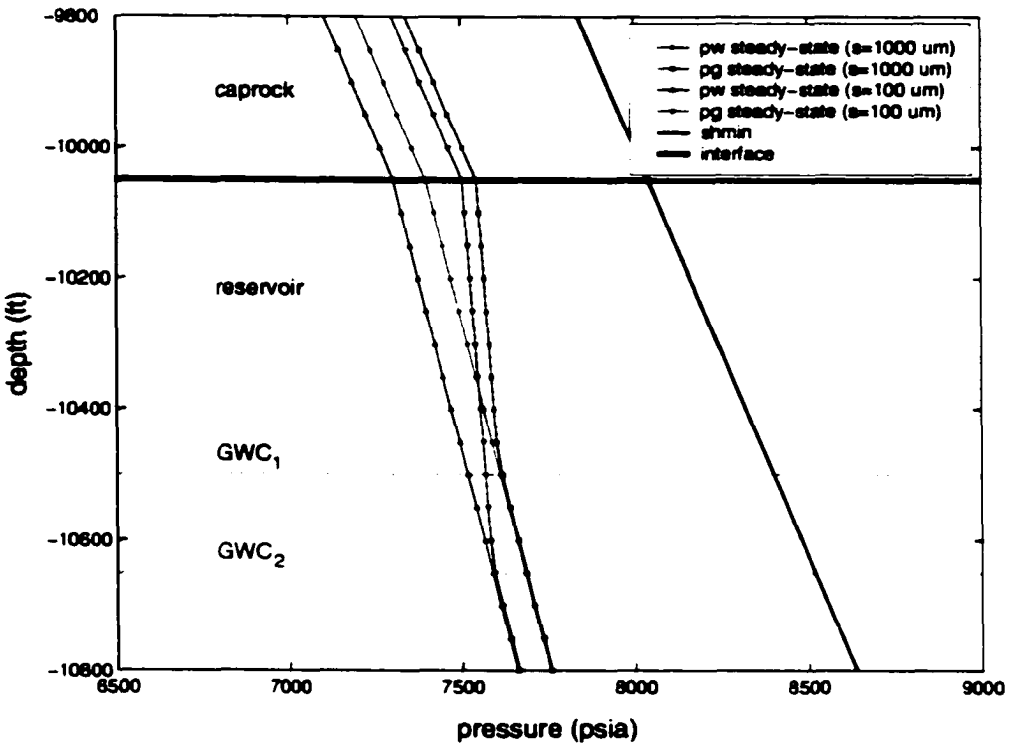

Figure 5.17: Predicted pressure across a caprock and reservoir in a 1-D, two-phase system. In the figure, GWC_1 and GWC_2 represent the gas-water contacts for two different spacings (see also caption of Figure 5.16).

Table 5.5: Gas column heights for two different spacings

Spacing (s) *um*	Gas column height *ft*
100	600
1000	450

5.2.6 Parametric study (varying the maximum asperity height)

We now study the effect of varying the maximum asperity height on the pressure build-up in the underlying reservoir and gas column height. Two different maximum asperity height are considered. Table 5.6 summarizes the input parameters for fracture permeability model.

Table 5.6: Parameters for fracture permeability.

Spacing (s) um	Maximum asperity length (W_o) um	Fractional contact area (f_c)
1000	5	4.65×10^{-05}
1000	10	4.65×10^{-05}

5.2.6.1 Varying the maximum asperity height in a single-phase system

Figure 5.18 shows the results of single-phase flow. Through this study, we found that by decreasing the maximum asperity height, the pressure build-up in the reservoir increases. This behavior is expected since at smaller fracture width, the permeability of the fracture is smaller which causes pressure build-up in the sand increases. This phenomenon is different compare to the previous case when we decrease the fracture spacing. When we decrease the fracture spacing, the pressure build-up also decreases.

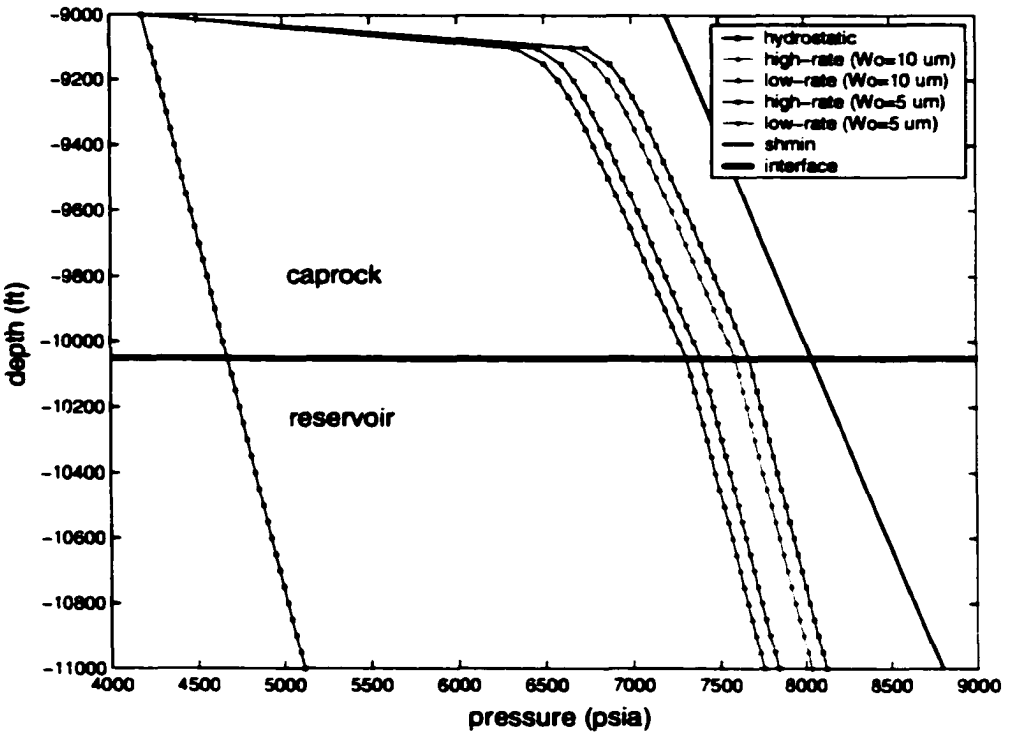

Figure 5.18: Predicted pressure across a caprock and reservoir in 1-D, single-phase system. In this study, two different maximum asperity height (W_o) with two different injection rates are considered. Parameters for fracture permeability model and the rates are given in Tables 5.2 and 5.6.

5.2.6.2 Varying the maximum asperity height in a two-phase system

Figures 5.19 and 5.20 show the results for two-phase flow. Similar to the previous case where we varied the spacing, water and gas are injected into the bottom of the reservoir simultaneously. The rates used are tabulated in Table 5.3. We observe that as the maximum asperity height decreases, the pressure build-up in the reservoir increases. This behavior is similar to what we found in a single-phase flow study. The low permeability in a caprock resulting from the decrease in the maximum asperity height contributes to the increased pressure build-up in the underlying reservoir.

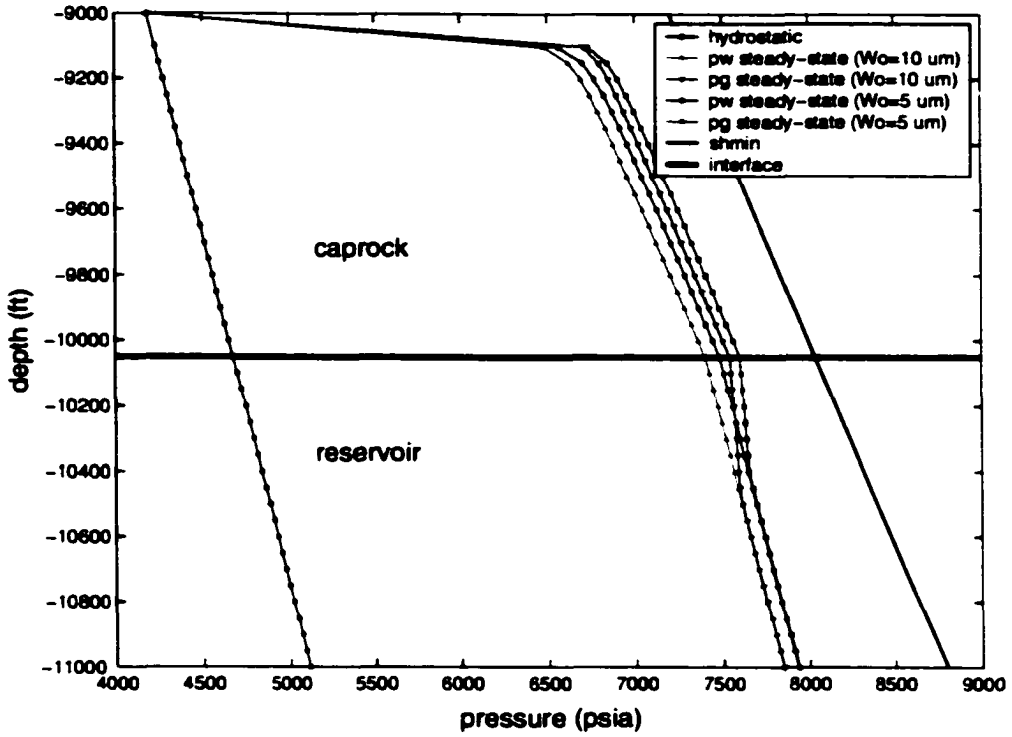

Figure 5.19: Predicted pressure across a caprock and reservoir in 1-D, two-phase system. In this study, two different maximum asperity heights (W_o) with one injection rate are considered. Parameters for fracture permeability model and the rate used are given in Tables 5.3 and 5.6.

Predicted pressure near the interface between a caprock and reservoir are given in Figure 5.20. The gas column heights measured from the gas-water contact to the interface of a caprock and reservoir for two different maximum asperity height (W_o) are given in Table 5.7. It can be seen that as W_o increases, the gas column decreases.

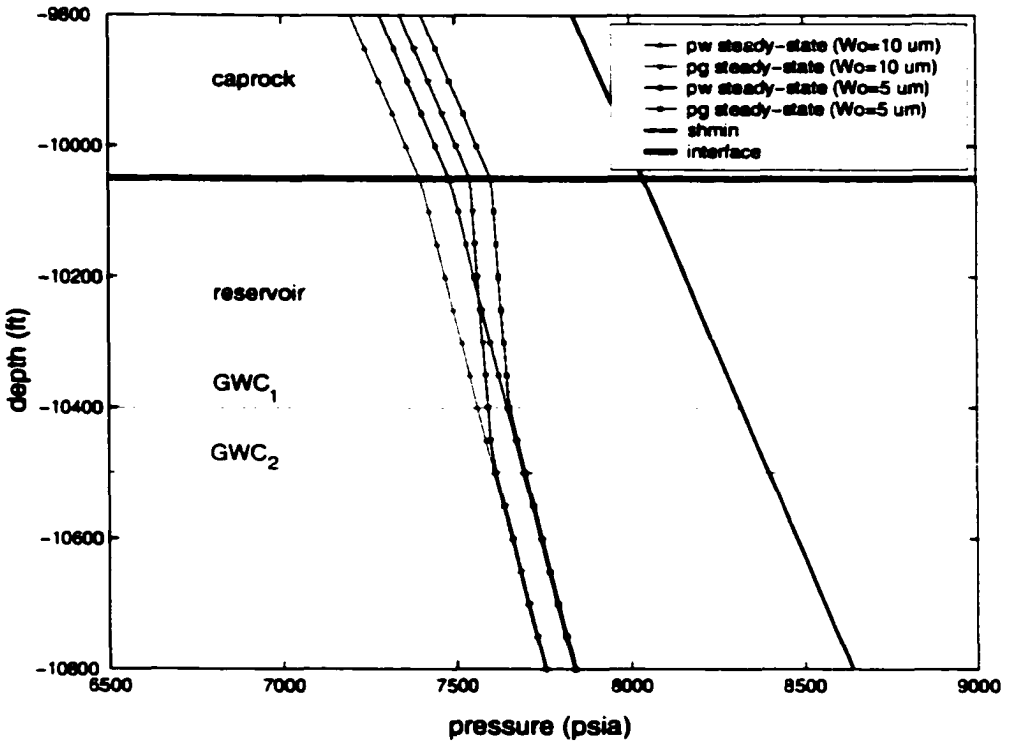

Figure 5.20: Predicted pressure across a caprock and reservoir in a 1-D, two-phase system. In the figure, GWC_1 and GWC_2 represent gas-water contact for two different W_o (see also caption of Figure 5.19).

Table 5.7: Gas column heights for two different Wo

Maximum asperity height (W_o) *um*	Gas column height *ft*
5	350
10	450

5.2.7 Parametric study (varying fractional contact area)

We now study the effect of varying the fractional contact area on pressure build-up in the underlying reservoir and gas column height. Two different fractional contact area are considered. Table 5.8 summarizes the input parameters for fracture permeability model.

Table 5.8: Parameters for fracture permeability.

Spacing (s) um	Maximum asperity length (W_o) um	Fractional contact area (f_c)
1000	10	4.65×10^{-05}
1000	10	6.70×10^{-05}

5.2.7.1 Varying fractional contact area in a single-phase system

Figure 5.21 shows the result of this study. We observe that as the fractional contact area (f_c) increases, the pressure build-up in the sand at the steady-state decreases. This behavior can be described through Figure 4.6 (Chapter 4). In Figure 4.6 we vary the f_c and have shown the corresponding fracture permeability for a given effective stress. It shows that as the f_c increases, the fracture permeability for a given stress also increases thus the phenomenon shown in Figure 5.21 is expected. As the f_c increases, the fracture permeability increases and decreases the pressure build-up in the reservoir.

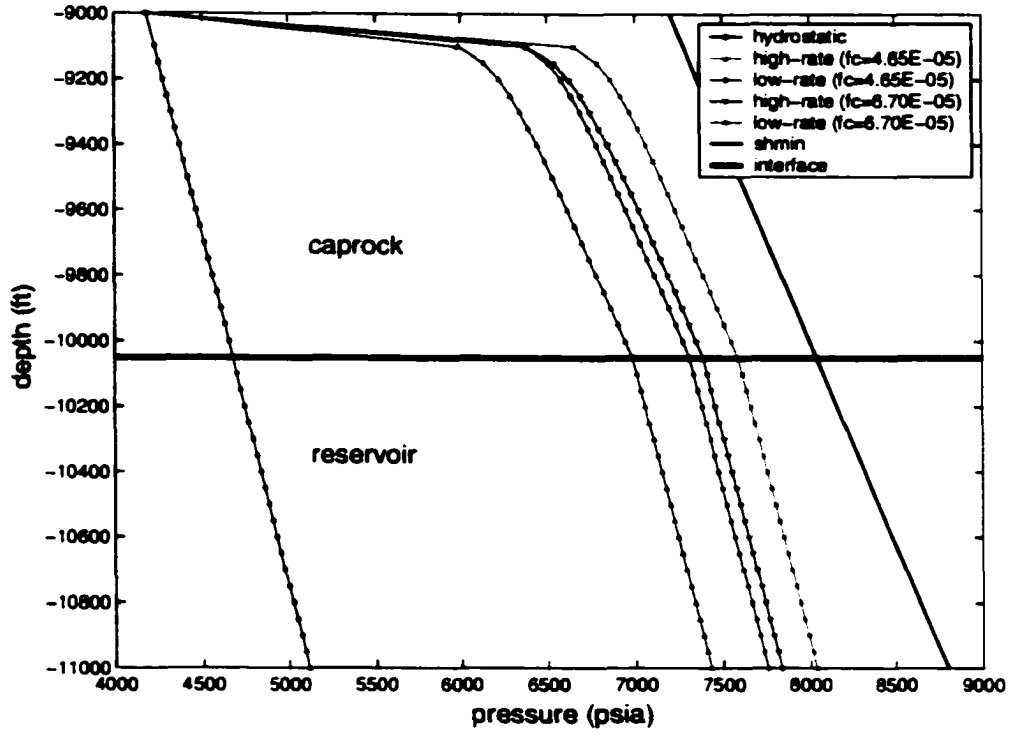

Figure 5.21: Predicted pressure across a caprock and reservoir in 1-D, single-phase system. In this study, two different fractional contact areas (f_c) and two different injection rates are considered. Parameters for fracture permeability model and the rates are given in Tables 5.2 and 5.8.

5.2.7.2 Varying fractional contact area in a two-phase system

Figures 5.22 and 5.23 show the results for two-phase flow. Similar to the previous cases where we varied the spacing and the maximum asperity height, water and gas are injected into the bottom of the reservoir simultaneously. The rates used are given in Table 5.3. We observe that as the fractional contact area increases, the pressure build-up in the reservoir decreases which indicates the increase of the effective stress.

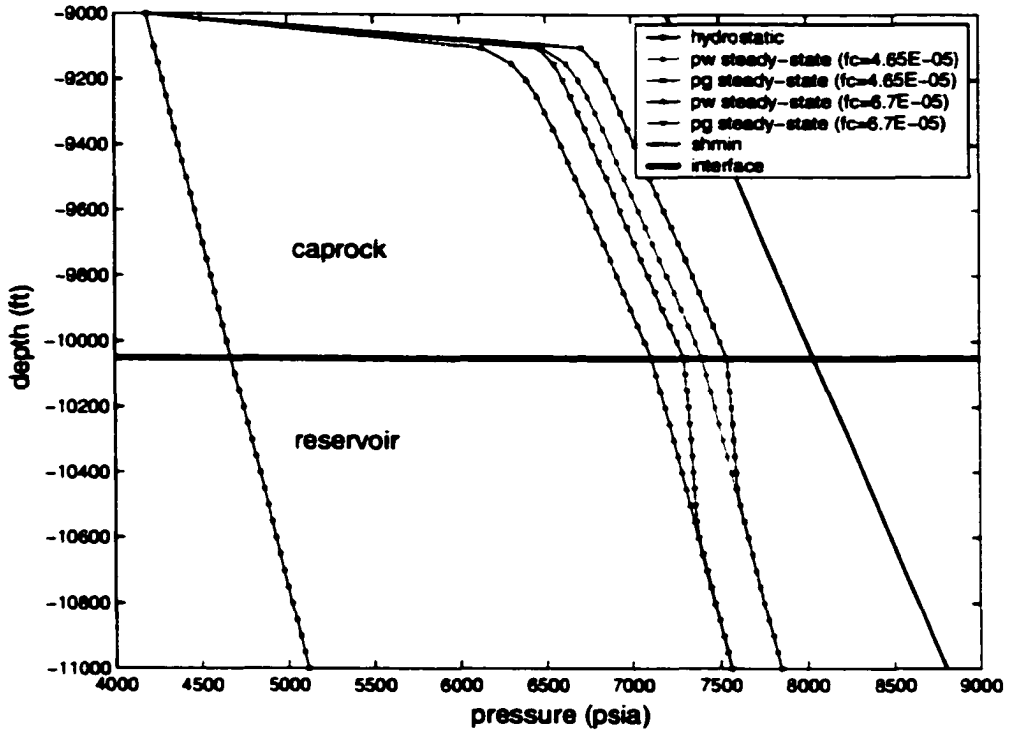

Figure 5.22: Predicted pressure across a caprock and reservoir in 1-D, two-phase system. In this study, two different fractional contact areas (f_c) are considered. Parameters for fracture permeability model and the rates used are given in Tables 5.3 and 5.8.

Predicted pressure near the interface between a caprock and reservoir are given in Figure 5.23. The gas column heights measured from the gas-water contact to the interface of a caprock and reservoir for different f_c are given in Table 5.9. It can be seen that as the f_c increases, the gas column height also increases.

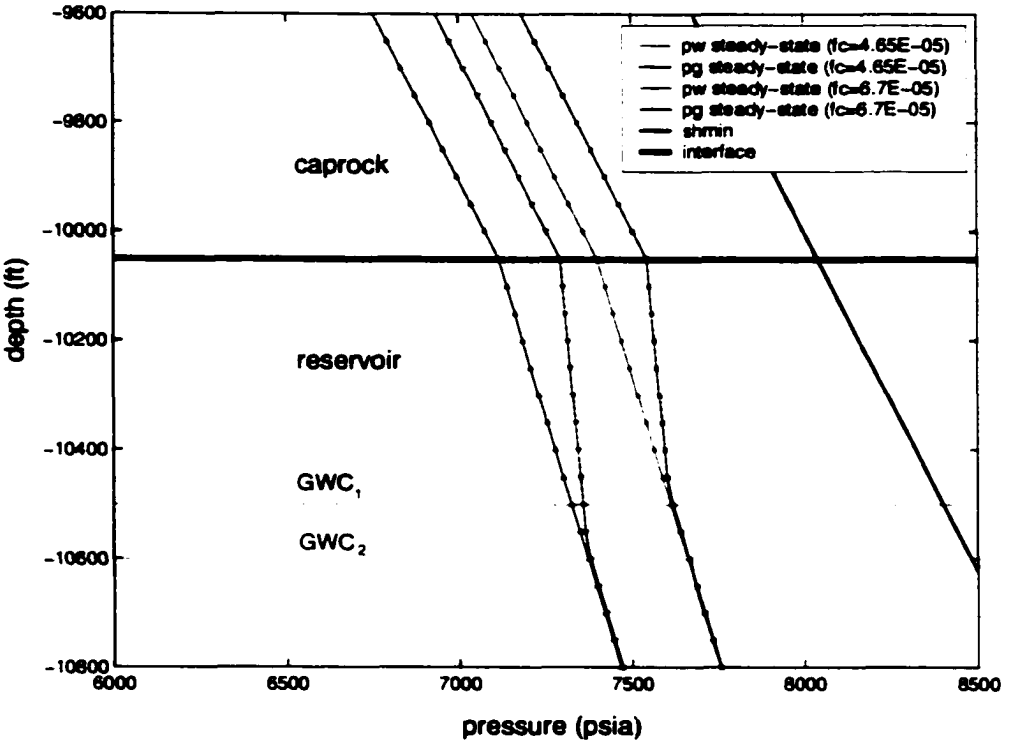

Figure 5.23: Predicted pressure across a caprock and reservoir in a 1-D, two-phase system. In the figure, GWC_1 and GWC_2 represent gas-water contact for two different f_c (see also caption of Figure 5.22).

Table 5.9: Gas column heights for two different contact areas

Fractional contact area (f_c)	Gas column height ft
4.65×10^{-05}	450
6.7×10^{-05}	550

5.3 Summary

1-D, single and two-phase steady-state models to simulate the flow through the fractures and to study the trap integrity in secondary gas migration are developed. The developed models combine the developed mechanical and hydraulic models into the Darcy's law. To study the behavior of a fractured caprock in respond to the water expulsions from the source rocks, a 1-D, single-phase (water) case is designed. In this case, water with constant flow-rate is injected into the bottom of the reservoir. Through the study we found that when the water influx increases, the pressure of the system increases. Near the upper boundary, the curvature of the pressure field is large due to the large minimum effective stress near the boundary. Beneath this boundary layer effect, the pressure gradient parallels to the least principle stress. The greater the flow-rate, the closer the pressure is to the least principal stress. In the reservoir, the pressure is found to parallel to the hydrostatic pressure due to the small injection rate and the high reservoir permeability.

In order to study the ability of a caprock to trap gas, 1-D two-phase (water and gas) cases are designed. In these cases, water and gas are injected into the bottom of the reservoir simultaneously. Similar to a single-phase model, in a two-phase model we found that the pressure of the system increases as the water and gas fluxes increase. Near the upper boundary, the curvature of the pressure field is large due to the large minimum effective stress and beneath this boundary layer effect, the pressure gradient (for both water and gas) parallels to the least principle stress which indicates the uniform of the fracture width.

The capillary pressure in a caprock is developed by assuming the fracture as a smooth parallel plate fracture. The capillary pressure with this model depends strongly on the fracture width and the minimum horizontal effective stress. When the fracture width is small, the capillary pressure is large.

The capacity of a caprock to trap gas depends strongly on the water influx and the fracture permeability. At large water influx, the gas column in the reservoir is small due to the small effective stress and the large fracture width.

Fracture permeability is found to play an important role in controlling the trap. We observe that by increasing the fracture spacing, the permeability of the fracture increases and the gas column height decreases. The maximum asperity height (W_o) also affects the permeability. At large W_o, the permeability of the fracture is large and this reduces the capability of the caprock to trap gas. We also found that as the fractional contact area increases, the pressure build-up in the reservoir decreases. This causes the effective stress in the caprock to increase and reduces the fracture width and the permeability and increases the gas column height.

Chapter 6

Time dependent flow

We now develop a numerical fluid-flow model to evaluate hydrocarbon migration through the reservoir and caprock system. We begin by developing a 1-D, numerical model of vertical hydrocarbon migration (Figure 5.1). This model describes single-phase and two-phase flow through a fractured caprock and predicts the resulting hydrocarbon column height in the underlying reservoir sand.

6.1 Governing equations

In developing a numerical model, we use the asperity model to describe a stress-dependent fracture permeability and combine the model with a numerical fluid-flow model. Two basic principles are used to derive the governing equation: mass conservation and Darcy's law. Mass conservation over the representative reservoir volume (Figure 6.1) is stated as:

$$[\textit{mass inflows - mass outflows}] + [\textit{source/sink}] = [\textit{mass accumulation}] \qquad (6.1)$$

where mass inflows is the sum of mass inflows across the control volume surfaces at $x - \Delta x/2$, $y - \Delta y/2$, and $z - \Delta z/2$ over the time interval Δt, mass outflows is the sum of mass outflows across control volume surfaces at $x + \Delta x/2$, $y + \Delta y/2$, and $z + \Delta z/2$ over the time interval Δt, source/sink is the sum of mass depletion over the time interval Δt, and mass accumulation is the mass accumulated due to the compressibility and fluid saturation changes in the control volume over the time interval Δt.

For rectangular coordinate system and for multi-phase flow, Eqn. 6.1 can be mathematically expressed as:

$$-\frac{\partial}{\partial x}\left(\dot{m}_{l_x} A_x\right)\Delta x - \frac{\partial}{\partial y}\left(\dot{m}_{l_y} A_y\right)\Delta y - \frac{\partial}{\partial z}\left(\dot{m}_{l_z} A_z\right)\Delta z + \tilde{q}_l = V_b\left(\frac{\partial m_l}{\partial t}\right) \quad (6.2)$$

where $\dot{m}_l$ is the mass flux, A is the area perpendicular to flux, m_l is the mass of fluid l per unit volume of porous media, $\tilde{q}_l$ is the rate of mass depletion, l is the phase index, and V_b is the bulk volume of control volume.

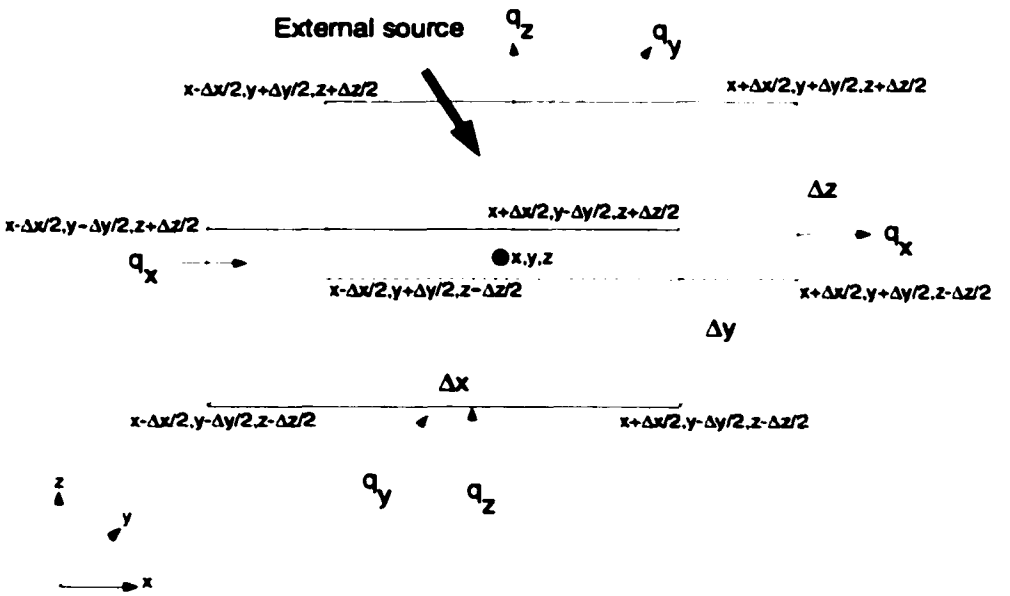

Figure 6.1: Control volume representation in cartesian coordinates. In the figure, the control volume is represented by the rectangular prism having dimensions Δx, Δy, and Δz with its center at (x, y, z). q_x, q_y, and q_z represent the fluid flow-rate in the x, y, and z directions (after Ertekin et al., 2001).

By expressing mass flux ($\dot{m}_l$) as a product of density and Darcy's velocity, mass flow rate ($\tilde{q}_l$) as the product of phase volumetric flow rate and phase density both at standard conditions, and mass per unit volume (m_l) as the product of porosity, phase saturation and density, Eqn. 6.2 can be expressed as (Ertekin et al., 2001):

$$-\frac{\partial}{\partial x}\left(\frac{A_x}{B_l}\upsilon_{l_x}\right)\Delta x-\frac{\partial}{\partial y}\left(\frac{A_y}{B_l}\upsilon_{l_y}\right)\Delta y-\frac{\partial}{\partial z}\left(\frac{A_z}{B_l}\upsilon_{l_z}\right)\Delta z+Q_{l_{sc}}=\frac{V_b}{\alpha_c}\frac{\partial}{\partial t}\left(\frac{\phi S_l}{B_l}\right) \quad (6.3)$$

where υ_l is the Darcy's velocity, B_l is the formation volume factor to convert volumes at reservoir pressure and temperature to their equivalent volumes at standard conditions and can be formulated as $B_l = \frac{\rho_{l_{sc}}}{\rho_l}$ where $\rho_{l_{sc}}$ and ρ_l represent the density of the fluid at the standard and reservoir conditions, $Q_{l_{sc}}$ is the volumetric flow rate at standard condition, ϕ is the porosity, S_l is the saturation of phase l, and α_c is a constant for unit conversion.

For a two-phase (gas and water system), the mass conservation equation for each phase can be written as:

water:

$$-\frac{\partial}{\partial x}\left(\frac{A_x}{B_w}\upsilon_{w_x}\right)\Delta x-\frac{\partial}{\partial y}\left(\frac{A_y}{B_w}\upsilon_{w_y}\right)\Delta y-\frac{\partial}{\partial z}\left(\frac{A_z}{B_w}\upsilon_{w_z}\right)\Delta z$$
$$+Q_{w_{sc}}=\frac{V_b}{\alpha_c}\frac{\partial}{\partial t}\left(\frac{\phi S_w}{B_w}\right) \quad (6.4)$$

gas:

$$-\frac{\partial}{\partial x}\left(\frac{A_x}{B_g}\upsilon_{g_x}+\frac{R_{sw}A_x}{B_w}\upsilon_{w_x}\right)\Delta x-\frac{\partial}{\partial y}\left(\frac{A_y}{B_g}\upsilon_{g_y}+\frac{R_{sw}A_y}{B_w}\upsilon_{w_y}\right)\Delta y$$

$$-\frac{\partial}{\partial y}\left(\frac{A_z}{B_g}\upsilon_{g_z}+\frac{R_{sw}A_z}{B_w}\upsilon_{w_z}\right)\Delta z+Q_{g_{sc}}=\frac{V_b}{\alpha_c}\frac{\partial}{\partial t}\left(R_{sw}\frac{\phi S_w}{B_w}+\frac{\phi S_g}{B_g}\right) \tag{6.5}$$

where $Q_{g_{sc}} = Q_{g_{f_{sc}}} + R_{sw}Q_w$; R_{sw} is the volume of gas in solution per unit volume of water; and $Q_{f_{sc}}$ is the free gas flow rate.

For multi-phase flow, Darcy's velocity for each phase $l = w, g$ is defined as:

$$\vec{\upsilon}_l = -\beta_c \frac{kk_{r_l}}{\mu_l}(\nabla\Phi) \tag{6.6}$$

where $\vec{\upsilon}_l$ is the Darcy's velocity (fluid flow rate per unit cross-sectional area), k is the bulk permeability, k_{r_l} is the relative permeability, μ_l is the fluid viscosity, $\nabla\Phi$ is the potential gradient, and β_c is the unit conversion.

To solve Eqn. 6.4 and 6.5 above we utilize IMPES (Implicit Pressure Explicit Saturation) method. In this method, water and gas equations are combined to form one single equation. This single equation is then solved implicitly to obtain the pressure distribution (p_w). Once the pressure is obtained, the saturation values are computed explicitly by substituting p_w into an appropriate saturation equation.

We combine water and gas equations by adding the two equations together in such a way that the final equation only has one principle unknown, water pressure (p_w). The right-hand side of the water equation is expanded:

$$\frac{V_b}{\alpha_c}\frac{\partial}{\partial t}\left(\frac{\phi S_w}{B_w}\right) = \frac{V_b}{\alpha_c}\left(\left(\frac{\phi}{B_w}\frac{\partial S_w}{\partial t}\right)+\left(\frac{S_w}{B_w}\frac{\partial \phi}{\partial p_g}-\frac{\phi S_w}{B_w^2}\frac{\partial B_w}{\partial p_g}\right)\frac{\partial p_g}{\partial t}\right) \tag{6.7}$$

Similarly, the right-hand side of gas equation is expanded:

$$\begin{aligned}\frac{V_b}{\alpha_c}\frac{\partial}{\partial t}\left(R_{sw}\frac{\phi S_w}{B_w}+\frac{\phi S_g}{B_g}\right) = \frac{V_b}{\alpha_c}\Bigg(&\left(\frac{\phi}{B_g}\frac{\partial S_g}{\partial t}\right)+\left(\frac{S_g}{B_g}\frac{\partial \phi}{\partial p_g}-\frac{\phi S_g}{B_g^2}\frac{\partial B_g}{\partial p_g}\right)\frac{\partial p_g}{\partial t}\\ &+\frac{R_{sw}\phi}{B_w}\frac{\partial S_w}{\partial t}+\left(\frac{R_{sw}S_w}{B_w}\frac{\partial \phi}{\partial p_g}-\frac{R_{sw}\phi S_w}{B_w^2}\frac{\partial B_w}{\partial p_g}+\frac{\phi S_w}{B_w}\frac{\partial R_{sw}}{\partial p_g}\right)\frac{\partial p_g}{\partial t}\Bigg)\end{aligned} \tag{6.8}$$

To obtain one single equation with one principle unknown, the time dependent saturation need to be removed from the right-hand side of the equations. Multiplying gas equation by $\left(-\frac{1}{\left(R_{sw}-\frac{B_w}{B_g}\right)}\right)$ and adding the two equations together will result in one equation with one principle unknown p_w (after substituting Eqn. 6.6 into 6.9 for Darcy's velocity and after substituting $p_w + P_{c_{ew}}$ for p_g).

$$\left(-\frac{1}{\left(R_{sw}-\frac{B_w}{B_g}\right)}\right)\left(-\frac{\partial}{\partial x}\left(\frac{A_x}{B_g}\upsilon_{g_x}+\frac{A_xR_{sw}}{B_w}\upsilon_{w_x}\right)\Delta x-\frac{\partial}{\partial y}\left(\frac{A_y}{B_g}\upsilon_{g_y}+\frac{A_yR_{sw}}{B_w}\upsilon_{w_y}\right)\Delta y\right.$$

$$\left.-\frac{\partial}{\partial z}\left(\frac{A_z}{B_g}\upsilon_{g_z}+\frac{A_zR_{sw}}{B_w}\upsilon_{w_z}\right)\Delta z+Q_{g_{sc}}\right)+\left(-\frac{\partial}{\partial x}\left(\frac{A_x}{B_w}\upsilon_{w_x}\right)\Delta x-\frac{\partial}{\partial y}\left(\frac{A_y}{B_w}\upsilon_{w_y}\right)\Delta y\right.$$

$$\left.-\frac{\partial}{\partial z}\left(\frac{A_z}{B_w}\upsilon_{w_z}\right)\Delta z+Q_{w_{sc}}\right)=\frac{V_b}{\alpha_c}\left(\left(\frac{S_g}{B_g}\frac{\partial\phi}{\partial p_g}-\frac{S_g\phi}{B_g^2}\frac{\partial B_g}{\partial p_g}+\frac{R_{sw}S_w}{B_w}\frac{\partial\phi}{\partial p_g}\right.\right. \tag{6.9}$$

$$\left.-\frac{R_{sw}\phi S_w}{B_w^2}\frac{\partial B_w}{\partial p_g}+\frac{S_w\phi}{B_w}\frac{\partial R_{sw}}{\partial p_g}\right)\left(-\frac{1}{\left(R_{sw}-\frac{B_w}{B_g}\right)}\right)\left(\frac{\partial p_w}{\partial t}+\frac{\partial P_{c_{gw}}}{\partial t}\right)$$

$$\left.+\left(\frac{S_w}{B_w}\frac{\partial\phi}{\partial p_g}-\frac{S_w\phi}{B_w^2}\frac{\partial B_w}{\partial p_g}\right)\left(\frac{\partial p_w}{\partial t}+\frac{\partial P_{c_{gw}}}{\partial t}\right)\right)$$

We now solve the partial differential equation using a finite-difference scheme to obtain the solutions at discrete points. We use body-centered grid system. In this system, pressure and saturation values are defined at the center of grid blocks. The boundary blocks, for a rectangular grid, are placed half way between the two adjacent pressure or saturation points. A seven point (in 3-D) finite-difference scheme is used. The interblock transmissibility between block itself and its neighboring blocks in x, y, and z-directions for phase $l = w, g$ are defined as:

$$T_{l_{i\pm1/2,j,k}} = \beta_c\left(\frac{k_xA_x}{\Delta x}\right)_{i\pm1/2,j,k}\left(\frac{1}{\mu_lB_l}\right)_{i\pm1/2,j,k}k_{r_{l_{i\pm1/2,j,k}}} \tag{6.10}$$

$$T_{l_{y_{i,j\pm1/2,k}}} = \beta_c \left(\frac{k_y A_y}{\Delta y}\right)_{i,j\pm1/2,k} \left(\frac{1}{\mu_l B_l}\right)_{i,j\pm1/2,k} k_{r_{l_{i,j\pm1/2,k}}} \tag{6.11}$$

$$T_{l_{z_{i,j,k\pm1/2}}} = \beta_c \left(\frac{k_z A_z}{\Delta z}\right)_{i,j,k\pm1/2} \left(\frac{1}{\mu_l B_l}\right)_{i,j,k\pm1/2} k_{r_{l_{i,j,k\pm1/2}}} \tag{6.12}$$

where $T_{l_{x_{i\pm1/2,j,k}}}$, $T_{l_{y_{i,j\pm1/2,k}}}$, and $T_{l_{z_{i,j,k\pm1/2}}}$ are the transmissibilities. The subscripts plus and minus are to identify block boundaries in the positive and negative directions in the cartesian coordinates; k_x, k_y, and k_z are the permeability in x, y, and z-directions, respectively; k_{r_l} is the relative permeability; Δx, Δy, and Δz are the block size; μ_l is the viscosity; and B_l is the formation volume factor for phase $l = w, g$.

For irregular grid size distribution, the term $\left(\frac{k_x A_x}{\Delta x}\right)$, $\left(\frac{k_y A_y}{\Delta y}\right)$, and $\left(\frac{k_z A_z}{\Delta z}\right)$ are obtained from harmonic average between the computational blocks. In this average, those terms are calculated from:

$$\left(\frac{k_x A_x}{\Delta x}\right)_{i\pm1/2,j,k} = \frac{2A_{x_{i,j,k}} k_{x_{i,j,k}} A_{x_{i\pm1,j,k}} k_{x_{i\pm1,j,k}}}{(A_{x_{i,j,k}} k_{x_{i,j,k}} \Delta x_{i\pm1,j,k} + A_{x_{i\pm1,j,k}} k_{x_{i\pm1,j,k}} \Delta x_{i,j,k})} \tag{6.13}$$

$$\left(\frac{k_y A_y}{\Delta y}\right)_{i,j\pm1/2,k} = \frac{2A_{y_{i,j,k}} k_{y_{i,j,k}} A_{y_{i,j\pm1,k}} k_{y_{i,j\pm1,k}}}{(A_{y_{i,j,k}} k_{y_{i,j,k}} \Delta y_{i,j\pm1,k} + A_{y_{i,j\pm1}} k_{y_{i,j\pm1}} \Delta y_{i,j,k})} \tag{6.14}$$

$$\left(\frac{k_z A_z}{\Delta z}\right)_{i,j,k\pm1/2} = \frac{2A_{z_{i,j,k}} k_{z_{i,j,k}} A_{z_{i,j,k\pm1}} k_{z_{i,j,k\pm1}}}{(A_{z_{i,j,k}} k_{z_{i,j,k}} \Delta z_{i,j,k\pm1} + A_{z_{i,j,k\pm1}} k_{z_{i,j,k\pm1}} \Delta z_{i,j,k})} \tag{6.15}$$

The weak non-linearity term $\left(\frac{1}{\mu_l B_l}\right)$ is handled and computed with the midpoint weighting between the computational blocks. For example, the weak non-linearity $\left(\frac{1}{\mu_l B_l}\right)_{i+1/2,\,j,\,k}$ at the block boundary $(i + 1/2,\, j,\, k)$ between block $(i,\, j,\, k)$ and $(i + 1,\, j,\, k)$ is computed from:

$$\left(\frac{1}{\mu_l B_l}\right)_{i+1/2,\,j,\,k} = \frac{1}{2}\left(\left(\frac{1}{\mu_l B_l}\right)_{i,\,j,\,k} + \left(\frac{1}{\mu_l B_l}\right)_{i+1/2,\,j,\,k}\right) \tag{6.16}$$

The strong non-linearity term, k_{r_l}, is handled and computed from one-point upstream weighting. In this upstream weighting, k_{r_l} is determined based on the flow direction. Consider the strong non-linearity $k_{r_{l_{i+1/2,\,j,\,k}}}$ at the boundary $(i + 1/2,\, j,\, k)$ between blocks $(i,\, j,\, k)$ and $(i + 1,\, j,\, k)$ in the x-direction. Using one-point upstream weighting $k_{r_{l_{i+1/2,\,j,\,k}}}$ is determined from:

$$k_{r_{l_{i+1/2,\,j,\,k}}} = k_{r_{l_{i,\,j,\,k}}} \text{ if the flow from } (i,\, j,\, k) \text{ to } (i + 1,\, j,\, k) \tag{6.17}$$

$$k_{r_{l_{i+1/2,\,j,\,k}}} = k_{r_{l_{i+1,\,j,\,k}}} \text{ if the flow from } (i + 1,\, j,\, k) \text{ to } (i,\, j,\, k) \tag{6.18}$$

The flow direction of phase $l = w, g$ between grid blocks $(i,\, j,\, k)$ and $(i + 1,\, j,\, k)$ is determined according to the phase potential difference.

Eqn. 6.9 contains $\frac{\partial}{\partial x}\left(a(x)\,\frac{\partial p}{\partial x} \right)$ term. By using the finite-difference scheme for point i, this term can be expanded into:

$$\frac{\partial}{\partial x}\left(a(x)\,\frac{\partial p}{\partial x} \right) = \frac{1}{\Delta x^2}\left(a_{i+1/2}(p_{i+1} - p_i) - a_{i-1/2}(p_i - p_{i-1}) \right) \tag{6.19}$$

We now put Eqn. 6.9 into finite-difference scheme. We follow SIP (Strongly Implicit Procedure) notation for a 3-D case and express it as:

$$Z_{i,j,k} \cdot p^{n+1}_{w_{i,j,k-1}} + B_{i,j,k} \cdot p^{n+1}_{w_{i,j-1,k}} + D_{i,j,k} \cdot p^{n+1}_{w_{i-1,j,k}} + E_{i,j,k} \cdot p^{n+1}_{w_{i,j,k}} + F_{i,j,k} \cdot p^{n+1}_{w_{i+1,j,k}} + H_{i,j,k} \cdot p^{n+1}_{w_{i,j+1,k}} + S_{i,j,k} \cdot p^{n+1}_{w_{i,j,k+1}} = Q_{i,j,k} \tag{6.20}$$

where:

$$Z_{i,j,k} = \left(-\frac{1}{R_{sw} - \frac{B_w}{B_g}} \right)^{k}_{i,j,k} \left(T_{g_{z_{i,j,k-1/2}}} + R_{sw} T_{w_{z_{i,j,k-1/2}}} \right)^{k}_{n+\theta} + T^{k}_{w_{z_{i,j,k-1/2}}} \tag{6.21}$$

$$B_{i,j,k} = \left(-\frac{1}{R_{sw} - \frac{B_w}{B_g}} \right)^{k}_{i,j,k} \left(T_{g_{y_{i,j-1/2,k}}} + R_{sw} T_{w_{y_{i,j-1/2,k}}} \right)^{k}_{n+\theta} + T^{k}_{w_{y_{i,j-1/2,k}}} \tag{6.22}$$

$$D_{i,j,k} = \left(-\frac{1}{R_{sw} - \frac{B_w}{B_g}} \right)^{k}_{i,j,k} \left(T_{g_{x_{i-1/2,j,k}}} + R_{sw} T_{w_{x_{i-1/2,j,k}}} \right)^{k}_{n+\theta} + T^{k}_{w_{x_{i-1/2,j,k}}} \tag{6.23}$$

$$F_{i,j,k} = \left(-\frac{1}{R_{sw} - \frac{B_w}{B_g}} \right)^{k}_{i,j,k} \left(T_{g_{x_{i+1/2,j,k}}} + R_{sw} T_{w_{x_{i+1/2,j,k}}} \right)^{k}_{n+\theta} + T^{k}_{w_{x_{i+1/2,j,k}}} \tag{6.24}$$

$$H_{i,j,k} = \left(-\frac{1}{R_{sw} - \frac{B_w}{B_g}} \right)^{k}_{i,j,k} \left(T_{g_{y_{i,j+1/2,k}}} + R_{sw} T_{w_{y_{i,j+1/2,k}}} \right)^{k}_{n+\theta} + T^{k}_{w_{y_{i,j+1/2,k}}} \tag{6.25}$$

$$S_{i,j,k} = \left(-\frac{1}{R_{sw} - \frac{B_w}{B_g}} \right)^{n+\theta}_{i,j,k} \left(T_{g_{z_{i,j,k+1/2}}} + R_{sw} T_{w_{z_{i,j,k+1/2}}} \right)^{k}_{n+\theta} + T^{k}_{w_{z_{i,j,k+1/2}}}{}^{n+\theta} \tag{6.26}$$

$$E_{i,j,k} = -(Z + B + D + F + H + S)_{i,j,k} - \frac{\Gamma_{i,j,k}}{\Delta t} \tag{6.27}$$

$$\Gamma_{i,j,k} = \frac{V_b}{\alpha_c} \left(\left(-\frac{1}{R_{sw} - \frac{B_w}{B_g}} \right)^{n+\theta}_{i,j,k} \left(\frac{S_g}{B_g} \frac{\partial \phi}{\partial p_g} - \frac{\phi S_g}{B_g^2} \frac{\partial B_g}{\partial p_g} + \frac{R_{sw} S_w}{B_w} \frac{\partial \phi}{\partial p_g} \right.\right.$$
$$\left.\left. - \frac{R_{sw} \phi S_w}{B_w^2} \frac{\partial B_w}{\partial p_g} + \frac{\phi S_w}{B_w} \frac{\partial R_{sw}}{\partial p_g} \right)^{k}_{n+\theta} + \left(\frac{S_w}{B_w} \frac{\partial \phi}{\partial p_g} \right)^{k}_{n+\theta} - \left(\frac{\phi S_w}{B_w^2} \frac{\partial B_w}{\partial p_g} \right)^{k}_{n+\theta} \right) \tag{6.28}$$

and the right-hand side is:

$$Q_{i,j,k} = Z'_{i,j,k}\, G_{i,j,k-1} + B'_{i,j,k}\, G_{i,j-1,k} + D'_{i,j,k}\, G_{i-1,j,k}$$

$$+ E'_{i,j,k}\, G_{i,j,k} + F'_{i,j,k}\, G_{i+1,j,k} + H'_{i,j,k}\, G_{i,j+1,k} + S'_{i,j,k}\, G_{i,j,k+1}$$

$$-\left(-\frac{1}{R_{sw}-\frac{B_w}{B_g}}\right)^{n+\theta}_{k} \Delta(T_g \Delta P_{c_{gw}}) - \left(\frac{\Gamma_{i,j,k}\, P^n_{w_{i,j,k}}}{\Delta t}\right) + \left(\frac{\Gamma_{i,j,k}}{\Delta t}\right)(P^n_{c_{gw}} - P^{n-1}_{c_{gw}}) \tag{6.29}$$

$$-\left(-\frac{1}{R_{sw}-\frac{B_w}{B_g}}\right)^{n+\theta}_{k} Q^{n+\theta}_{g_{sc}} - Q^{n+\theta}_{w_{sc}}$$

where $G_{i,j,k}$ is the depth measured to the center of the block (i, j, k). Other coefficients are defined as:

$$Z'_{i,j,k} = \left(-\frac{1}{R_{sw}-\frac{B_w}{B_g}}\right)^{n+\theta}_{i,j,k} \left(T^{n+\theta}_{g_{z_{i,j,k-1/2}}} \rho^{n+\theta}_{g_{i,j,k-1/2}}\, g + R^{n+\theta}_{sw}\, T^{n+\theta}_{w_{z_{i,j,k-1/2}}} \rho^{n+\theta}_{w_{i,j,k-1/2}}\, g\right) + \left(T^{n+\theta}_{w_{z_{i,j,k-1/2}}} \rho_{w_{i,j,k-1/2}}\, g\right) \tag{6.30}$$

$$B'_{i,j,k} = \left(-\frac{1}{R_{sw}-\frac{B_w}{B_g}}\right)^{n+\theta}_{i,j,k} \left(T^{n+\theta}_{g_{y_{i,j-1/2,k}}} \rho^{n+\theta}_{g_{i,j-1/2,k}}\, g + R^{n+\theta}_{sw}\, T^{n+\theta}_{w_{y_{i,j-1/2,k}}} \rho^{n+\theta}_{w_{i,j-1/2,k}}\, g\right) + \left(T^{n+\theta}_{w_{y_{i,j-1/2,k}}} \rho_{w_{i,j-1/2,k}}\, g\right) \tag{6.31}$$

$$D'_{i,j,k} = \left(-\frac{1}{R_{sw} - \frac{B_w}{B_g}} \right)_{i,j,k}^{n+\theta} \left(T_{g_{x_{i-1/2,j,k}}}^{k\,n+\theta} \rho_{g_{i-1/2,j,k}}^{k\,n+\theta} g + R_{sw}^{k\,n+\theta} T_{w_{x_{i-1/2,j,k}}}^{k\,n+\theta} \rho_{w_{i-1/2,j,k}}^{k\,n+\theta} g \right) + \left(T_{w_{x_{i-1/2,j,k}}}^{k\,n+\theta} \rho_{w_{i-1/2,j,k}} g \right) \tag{6.32}$$

$$F'_{i,j,k} = \left(-\frac{1}{R_{sw} - \frac{B_w}{B_g}} \right)_{i,j,k}^{n+\theta} \left(T_{g_{x_{i+1/2,j,k}}}^{k\,n+\theta} \rho_{g_{i+1/2,j,k}}^{k\,n+\theta} g + R_{sw}^{k\,n+\theta} T_{w_{x_{i+1/2,j,k}}}^{k\,n+\theta} \rho_{w_{i+1/2,j,k}}^{k\,n+\theta} g \right) + \left(T_{w_{x_{i+1/2,j,k}}}^{k\,n+\theta} \rho_{w_{i+1/2,j,k}} g \right) \tag{6.33}$$

$$H'_{i,j,k} = \left(-\frac{1}{R_{sw} - \frac{B_w}{B_g}} \right)_{i,j,k}^{n+\theta} \left(T_{g_{y_{i,j+1/2,k}}}^{k\,n+\theta} \rho_{g_{i,j+1/2,k}}^{k\,n+\theta} g + R_{sw}^{k\,n+\theta} T_{w_{y_{i,j+1/2,k}}}^{k\,n+\theta} \rho_{w_{i,j+1/2,k}}^{k\,n+\theta} g \right) + \left(T_{w_{y_{i,j+1/2,k}}}^{k\,n+\theta} \rho_{w_{i,j+1/2,k}} g \right) \tag{6.34}$$

$$S_{i,j,k} = \left(-\frac{1}{R_{sw} - \frac{B_w}{B_g}} \right)_{i,j,k}^{n+\theta} \left(T_{g_{z_{i,j,k+1/2}}}^{k\,n+\theta} \rho_{g_{i,j,k+1/2}}^{k\,n+\theta} g + R_{sw}^{k\,n+\theta} T_{w_{z_{i,j,k+1/2}}}^{k\,n+\theta} \rho_{w_{i,j,k+1/2}}^{k\,n+\theta} g \right) + \left(T_{w_{z_{i,j,k+1/2}}}^{k\,n+\theta} \rho_{w_{i,j,k+1/2}} g \right) \tag{6.35}$$

$$E'_{i,j,k} = -(Z'_{i,j,k} + B'_{i,j,k} + D'_{i,j,k} + F'_{i,j,k} + H'_{i,j,k} + S'_{i,j,k}) \tag{6.36}$$

$$\Delta(T_g \Delta P_{c_{gw}}) = \Delta(T_{g_x} \Delta P_{c_{gw_x}}) + \Delta(T_{g_y} \Delta P_{c_{gw_y}}) + \Delta(T_{g_z} \Delta P_{c_{gw_z}}) \tag{6.37}$$

where:

$$\Delta\left(T_{g_x}\Delta P_{c_{gw_x}}\right) = T^{\,k}_{g_{x_{i+1/2,j,k}}}\left(P^{\,k}_{c_{gw_{i+1,j,k}}} - P^{\,k}_{c_{gw_{i,j,k}}}\right) - T^{\,k}_{g_{x_{i-1/2,j,k}}}\left(P^{\,k}_{c_{gw_{i,j,k}}} - P^{\,k}_{c_{gw_{i-1,j,k}}}\right) \quad (6.38)$$

$$\Delta(T_{g_y}\Delta P_{c_{gw_y}}) = T^{\,k}_{g_{y_{i,j+1/2,k}}}\left(P^{\,k}_{c_{gw_{i,j+1,k}}} - P^{\,k}_{c_{gw_{i,j,k}}}\right) - T^{\,k}_{g_{y_{i,j-1/2,k}}}\left(P^{\,k}_{c_{gw_{i,j,k}}} - P^{\,k}_{c_{gw_{i,j-1,k}}}\right) \quad (6.39)$$

$$\Delta(T_{g_z}\Delta P_{c_{gw_z}}) = T^{\,k}_{g_{z_{i,j,k+1/2}}}\left(P^{\,k}_{c_{gw_{i,j,k+1}}} - P^{\,k}_{c_{gw_{i,j,k}}}\right) - T^{\,k}_{g_{z_{i,j,k-1/2}}}\left(P^{\,k}_{c_{gw_{i,j,k}}} - P^{\,k}_{c_{gw_{i,j,k-1}}}\right) \quad (6.40)$$

The $n+\theta$ represents a time level between the old time level and the new time level. θ can be assigned from 0 to 1, if $\theta = 0$, the parameters which are a function of time are calculated at the previous time level and if $\theta = 1$, the parameters are evaluated at the new time level at one iteration behind. In our study, we use $\theta = 0.5$, thus the computed parameters are the average of the parameters computed at the new and previous time levels. k and $k+1$ represent the old and new iteration level.

In the IMPES method, water pressures are solved implicitly and saturation are determined explicitly. Eqn. 6.20 is solved implicitly for the unknown p_w. After solving Eqn. 6.20 for p_w, we determine saturation values explicitly by substituting p_w at new time level $n+1$ into an appropriate saturation equation. Re-write Eqn. 6.7 as:

$$\frac{V_b}{\alpha_c}\frac{\partial}{\partial t}\left(\frac{\phi S_w}{B_w}\right) = \frac{V_b}{\alpha_c}\left(\frac{\phi}{B_w}\frac{\partial S_w}{\partial t} + \frac{S_w}{B_w}\frac{\partial \phi}{\partial p_g}\frac{\partial p_g}{\partial t} - \frac{\phi S_w}{B_w^2}\frac{\partial B_w}{\partial p_g}\frac{\partial p_g}{\partial t}\right) \quad (6.41)$$

$$\frac{V_b}{\alpha_c}\frac{\partial}{\partial t}\left(\frac{\phi S_w}{B_w}\right) = \frac{V_b}{\alpha_c}\left(\frac{\phi}{B_w}\frac{S_w^{n+1} - S_w^n}{\Delta t}\right) + \frac{V_b}{\alpha_c}\left(\frac{S_w}{B_w}\frac{\partial \phi}{\partial p_g} - \frac{\phi S_w}{B_w^2}\frac{\partial B_w}{\partial p_g}\right) \left(\frac{\partial p_w}{\partial t} + \frac{\partial P_c}{\partial t}\right) \tag{6.42}$$

$$\frac{V_b}{\alpha_c}\frac{\partial}{\partial t}\left(\frac{\phi S_w}{B_w}\right) = \frac{V_b}{\alpha_c}\left(\frac{\phi}{B_w}\frac{S_w^{n+1} - S_w^n}{\Delta t}\right) + \frac{V_b}{\alpha_c}\left(\frac{S_w}{B_w}\frac{\partial \phi}{\partial p_g} - \frac{\phi S_w}{B_w^2}\frac{\partial B_w}{\partial p_g}\right) \left(\frac{p_w^{n+1} - p_w^n}{\Delta t} + \frac{P_c^{\,n} - P_c^{n-1}}{\Delta t}\right) \tag{6.43}$$

and then using Eqn. 6.4 solve for water saturation S_w^{n+1}:

$$\begin{aligned} S_{w_{i,j,k}}^{n+1} = {} & S_{w_{i,j,k}}^{n} + \frac{\alpha_c \Delta t}{V_b}\left(\frac{B_w}{\phi}\right)_{i,j,k}^{n+\theta}\left(\Delta(T_w \Delta p_w) - \rho_w g\,\Delta(T_w \Delta G) + Q_{w_{i,j,k}}\right) \\ & -\Delta t\left(\frac{B_w}{\phi}\right)_{i,j,k}^{n+\theta}\left(\frac{S_w}{B_w}\frac{\partial \phi}{\partial p_g} - \frac{\phi S_w}{B_w^2}\frac{\partial B_w}{\partial p_g}\right)_{i,j,k}^{n+\theta}\left(\frac{p_{w_{i,j,k}}^{n+1} - p_{w_{i,j,k}}^{n}}{\Delta t}\right) \\ & -\Delta t\left(\frac{B_w}{\phi}\right)_{i,j,k}^{n+\theta}\left(\frac{S_w}{B_w}\frac{\partial \phi}{\partial p_g} - \frac{\phi S_w}{B_w^2}\frac{\partial B_w}{\partial p_g}\right)_{i,j,k}^{n+\theta}\left(\frac{P_{c_{i,j,k}}^{n} - P_{c_{i,j,k}}^{n-1}}{\Delta t}\right) \end{aligned} \tag{6.44}$$

where:

$$\Delta(T_w \Delta P_w) = \Delta(T_{w_x} \Delta p_{w_x}) + \Delta(T_{w_y} \Delta p_{w_y}) + \Delta(T_{w_z} \Delta p_{w_z}) \tag{6.45}$$

$$\Delta(T_{w_x} \Delta p_{w_x}) = T_{w_{x_{i+1/2,j,k}}} \cdot (p_{w_{i+1,j,k}} - p_{w_{i,j,k}}) - T_{w_{i-1/2,j,k}} \cdot (p_{w_{i,j,k}} - p_{w_{i-1,j,k}}) \tag{6.46}$$

$$\Delta(T_{w_y} \Delta p_{w_y}) = T_{w_{y_{i,j+1/2,k}}} \cdot (p_{w_{i,j+1,k}} - p_{w_{i,j,k}}) - T_{w_{i,j-1/2,k}} \cdot (p_{w_{i,j,k}} - p_{w_{i,j-1,k}}) \tag{6.47}$$

$$\Delta(T_{w_z} \Delta p_{w_z}) = T_{w_{z_{i,j,k+1/2}}} \cdot (P_{w_{i,j,k+1}} - p_{w_{i,j,k}}) - T_{w_{z_{i,j,k-1/2}}} \cdot (p_{w_{i,j,k}} - p_{w_{i,j,k-1}}) \tag{6.48}$$

and

$$\Delta(T_w \Delta G) = \Delta(T_{w_x} \Delta G_x) + \Delta(T_{w_y} \Delta G_y) + \Delta(T_{w_z} \Delta G_z) \tag{6.49}$$

$$\Delta(T_{w_x} \Delta G_x) = T_{w_{x_{i+1/2,j,k}}} \cdot (G_{i+1,j,k} - G_{i,j,k}) - T_{w_{x_{i-1/2,j,k}}} \cdot (G_{i,j,k} - G_{i-1,j,k}) \tag{6.50}$$

$$\Delta(T_{w_y} \Delta G_y) = T_{w_{y_{i,j+1/2,k}}} \cdot (G_{i,j+1,k} - G_{i,j,k}) - T_{w_{y_{i,j-1/2,k}}} \cdot (G_{i,j,k} - G_{i,j-1,k}) \tag{6.51}$$

$$\Delta(T_{w_z} \Delta G_z) = T_{w_{z_{i,j,k+1/2}}} \cdot (G_{i,j,k+1} - G_{i,j,k}) - T_{w_{z_{i,j,k-1/2}}} \cdot (G_{i,j,k} - G_{i,j,k-1}) \tag{6.52}$$

Once the water pressure p_w and water saturation S_w are obtained, gas pressure can be calculated using capillary pressure relationship:

$$p_g^{n+1} = p_w^{n+1} + P_{c_{gw}}(S_w^{n+1}) \tag{6.53}$$

The gas saturation can be obtained from saturation relationship:

$$S_g^{n+1} = 1 - S_w^{n+1} \tag{6.54}$$

Eqn. 6.20 and 6.44 need to be solved iteratively. The non-linear parameters in the equations are handled by bringing the time-dependent terms one iteration behind. For the stress-dependent permeability, the value of permeability for each caprock block is updated before the convergence of the non-linear iterations.

6.2. Computational procedure

We now develop a procedure to solve the transient case numerically. The computational procedure we use is summarized below:

1. The extrapolation values are obtained. At this step, the guessed values of each block for the new time level ($n + 1$) are computed from the values at time level n and $n - 1$. The pressure and saturation values for each block are computed using the following extrapolation routine:

$$p_w^{n+1^*} = p_w^n + (p_w^n - p_w^{n-1}) \tag{6.55}$$

$$S_w^{n+1^*} = S_w^n + (S_w^n - S_w^{n-1}) \tag{6.56}$$

$$S_g^{n+1^*} = 1 - S_w^{n+1^*} \tag{6.57}$$

The gas pressure values $p_g^{n+1^*}$ are then computed using capillary pressure relationship.

2. After obtaining extrapolation values, we then calculate $n + \theta$ level values for pressure and saturation. We use the extrapolation values to obtain the $n + \theta$ level values by using Eqn. 6.58. The value of θ in general be any value between 0 and 1, but as described earlier is taken to be 0.5 in this work.

$$p_w^{n+\theta} = \theta\, p_w^{n+1^*} + (1-\theta)\, p_w^n \tag{6.58}$$

The water and gas saturation can be obtained with similar fashion.

3. Once we get pressure and saturation values at $n + \theta$ level, The transmissibility of each block is calculated. In this step, the transmissibility of each block and the stress-dependent permeability together with the capillary pressure are computed. The capillary pressure in a caprock depends on the effective stress. All values such as relative permeability and fluid properties are also computed at $n + \theta$ level.

4. After calculating the transmissibilities, we develop SIP coefficients for each block, we develop a system of linear algebraic equations and then we solve the equations using a direct solver. In this work we used the LEQT1B direct solver (IMSL, 1978).

5. After completing step 4, we explicitly calculate a water saturation for each block using the iteration pressure values from step 4. The gas saturation is then calculated from the water saturation. The capillary pressure is calculated from the effective stress (shale blocks) or from the water saturation (sand blocks). Both gas saturation and capillary pressure are calculated at the new iteration level.

6. The computed values from steps 4 and 5 are then compared with the extrapolated values. If they agree within a given set of tolerances, the computation proceed to the next time level. If they do not agree within pre-determined tolerances, the computation goes back to step 2 and the calculated values becomes the extrapolated values. The tolerances we used are 0.01 psia for pressure and $1.\times10^{-05}$ for saturation.

7. The last step before proceeding to the next time level is the material balance check. Here we perform a volume balance calculation. The amount of fluid that enter the system together with the amount of fluid that leave the system are compared with the change of the total fluid in the system. If the material balance does not agree with the accepted tolerance, the pressure and saturation tolerances are decreased and we proceed to the next time level.

The following algorithm is given to describe the computational procedure:

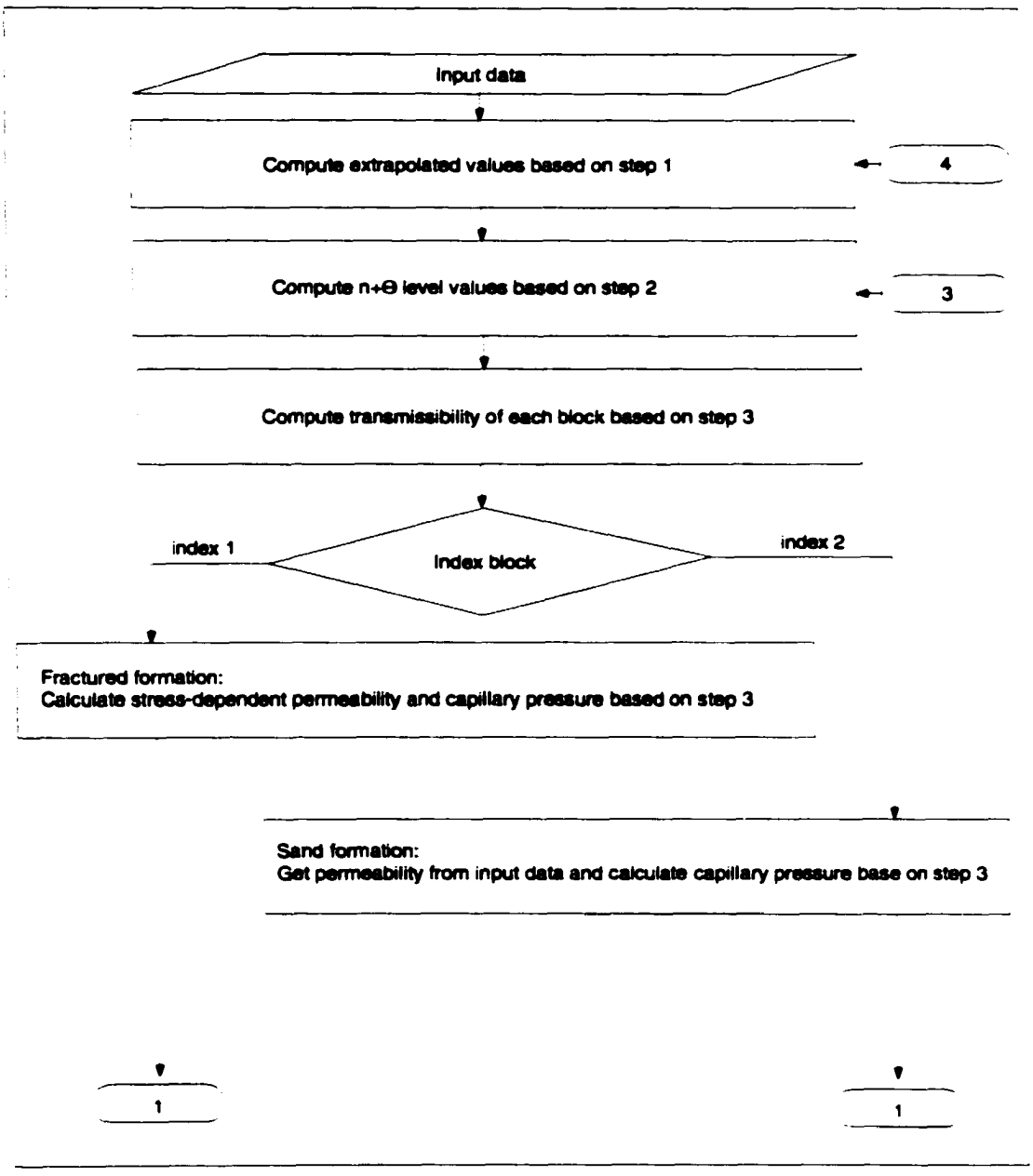

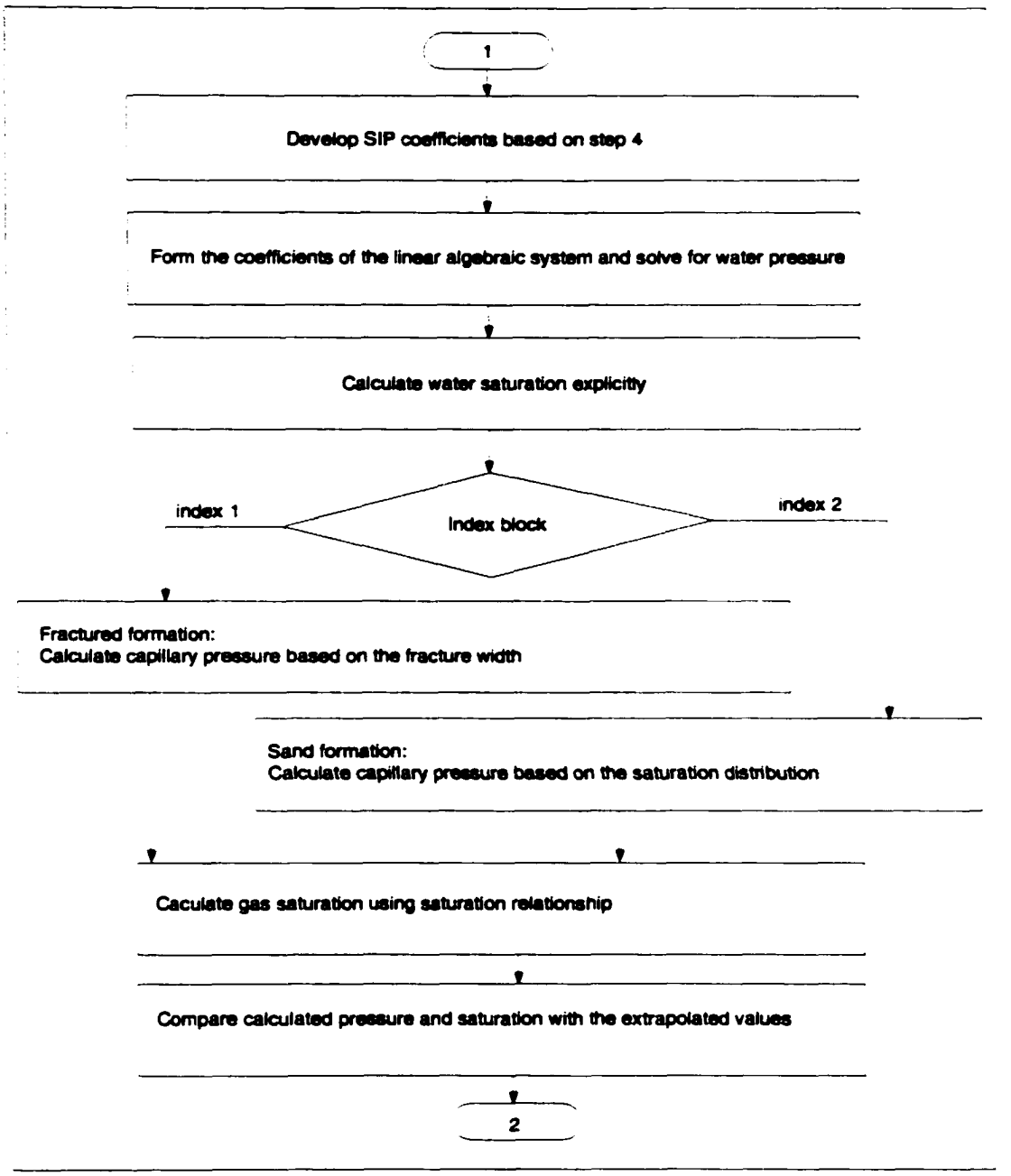

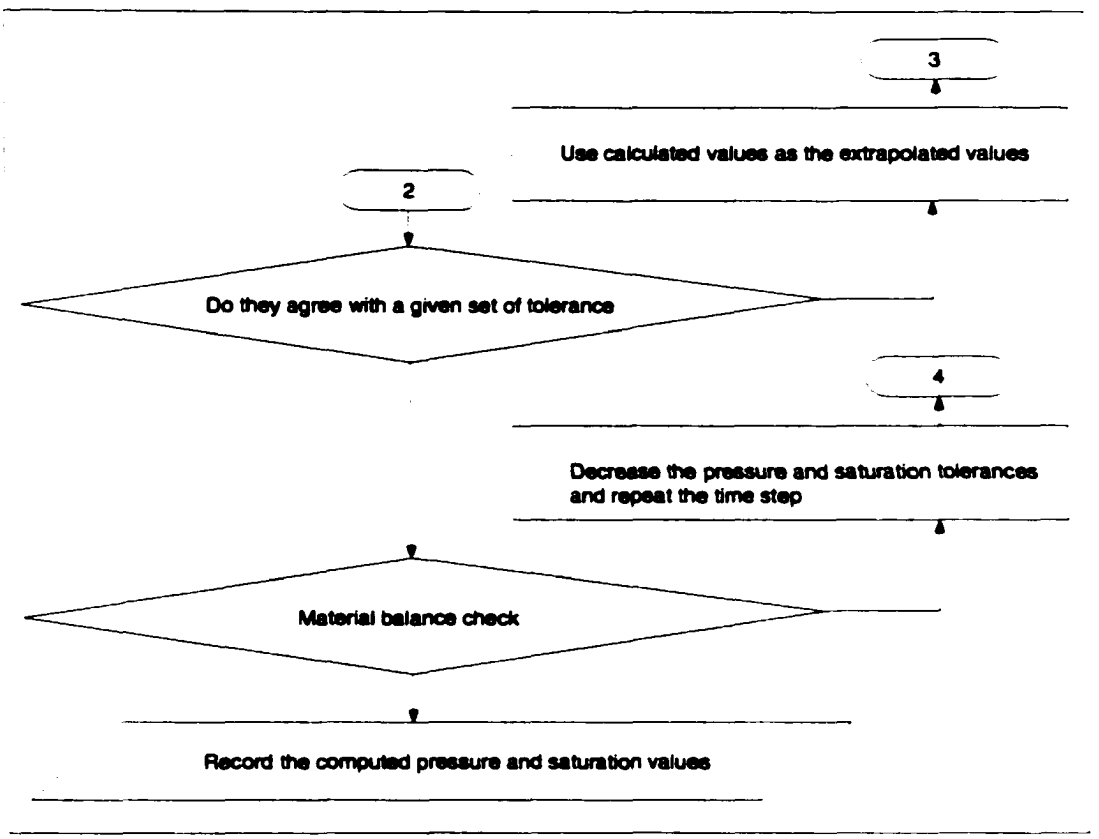

Figure 6.2: Algorithm of a numerical transient simulator.

6.3 Mathematical expression of bulk porosity (ϕ) in fractured rock

For a caprock, the porosity, ϕ, depends on the stresses and can be computed from:

$$\phi(S_{hmin}, S_{hmax}, S_v) = \frac{w_x(S_{hmin})}{s_x} + \frac{w_y(S_{hmax})}{s_y} + \frac{w_z(S_v)}{s_z} \tag{6.59}$$

where S_{hmin}, S_{hmax}, and S_v are the three principal stresses; w_x, w_y, and w_z are the hydraulic fracture widths; s_x, s_y, and s_z are the fracture spacings in x, y, and z directions, respectively.

Figure 6.3 describes the bulk porosity of a caprock containing vertical and horizontal fractures. The bulk porosity is computed based on Eqn. 6.59 with a fracture spacing of 1000 um and the maximum asperity height is 10 um in all three directions. The fractional contact area between asperities and fracture surface is 4.65×10^{-05} and the asperity Young's modulus is 1.8×10^{4} MPa.

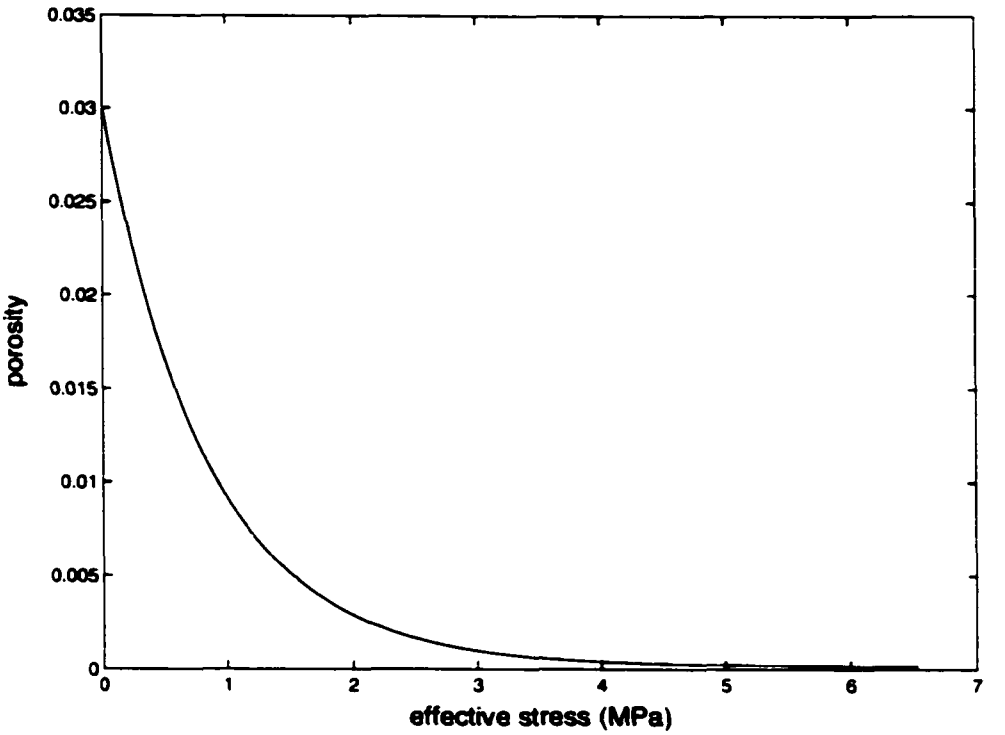

Figure 6.3: Bulk porosity vs. the effective stress of a caprock containing vertical and horizontal fractures. In this figure, it is assumed that the three principal stresses (S_v, S_{hmax}, and S_{hmin}) are equal.

6.4 Transient single-phase model.

We now apply the transient numerical model to 1-D and 2-D cases. We start with the 1-D case. The 1-D case is designed and is used as a tool to compare the steady-state and transient models. Figure 5.1 presented in the previous chapter is used. We extend the number of blocks in x-direction to perform a 2-D case. In addition we design 2-D case where the system has a dip-angle.

6.4.1 Comparison between steady-state and transient model in 1-D case

Figure 5.1 and Table 6.1 are used in this study. The system is divided into two different formations. The upper half is the caprock and the lower half is a sand formation. Water with flux $1.\times10^{-06}\ STB/D\cdot ft^2$ is injected into the system through the base of the sand formation. Hydrostatic pressure is maintained at the top of a caprock. This is the same boundary condition we imposed in the steady-state model presented previously. The initial system pressure is initially hydrostatic. In the caprock the minimum horizontal (S_{hmin}) stress is assumed to have a constant gradient of 0.8 psi/ft. The permeability of the caprock depends on the effective stress. For this study we assign fracture spacing of 1000 um (see Figure 4.5 for permeability model).

Table 6.1: Input data for 1-D case.

Parameter	Value
Size of the system	100 ft. x 100 ft. x 2000 ft.
Sand porosity	0.1
Sand permeability k_x [a]	30 md
Sand permeability k_y [b]	30 md
Sand permeability k_z	3 md
Initial pressure	hydrostatic
Initial saturation	100% water
Rock compressibility	3×10^{-06} 1/psi

a. in 1-D case this permeability is not used
b. in 1-D case this permeability is not used

The numerical model is run until steady state is reached. As shown in Figure 6.4, these steady state results are in good agreement with steady-state model results from Chapter 5. Because we assume that S_{hmin} constant, as the block pressure increases the effective stress decreases. This causes the fracture to open wider and increases permeability of the caprock. The pressure gradient in the sand is nearly hydrostatic due to the small flux and the relatively high permeability of the sand ($3\ md$).

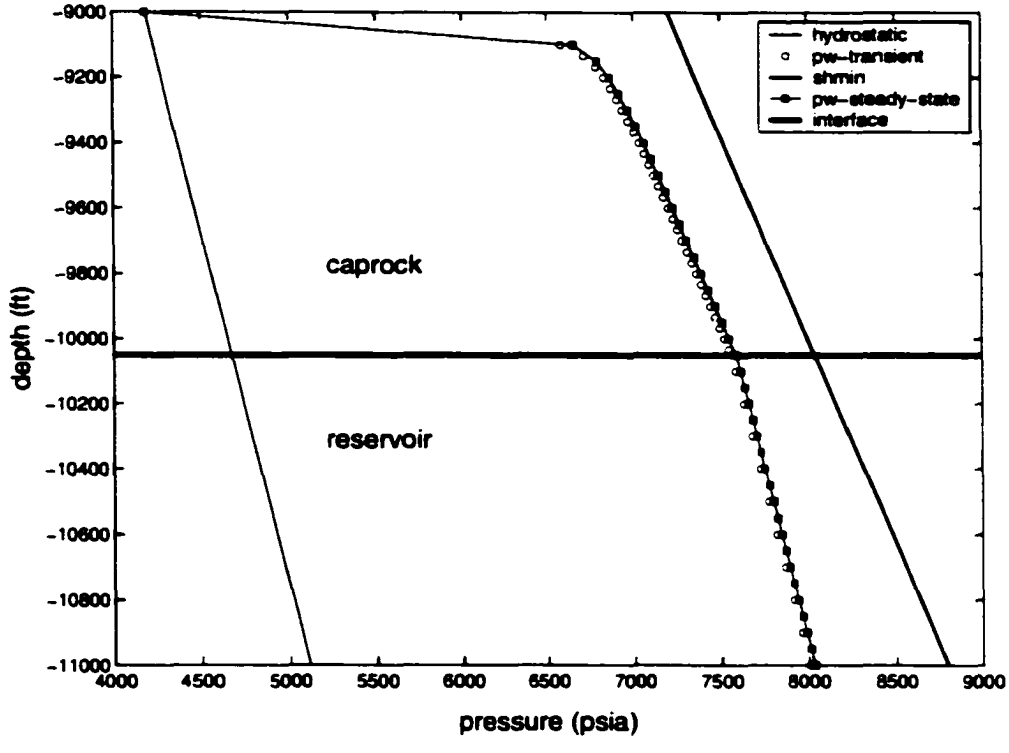

Figure 6.4: The comparison of pressure in a 1-D, single-phase system for a steady-state and transient models.

Figure 6.5 shows pressure profiles near the interface between the caprock and the sand. The good agreement between the two models (steady-state and transient models) is observed.

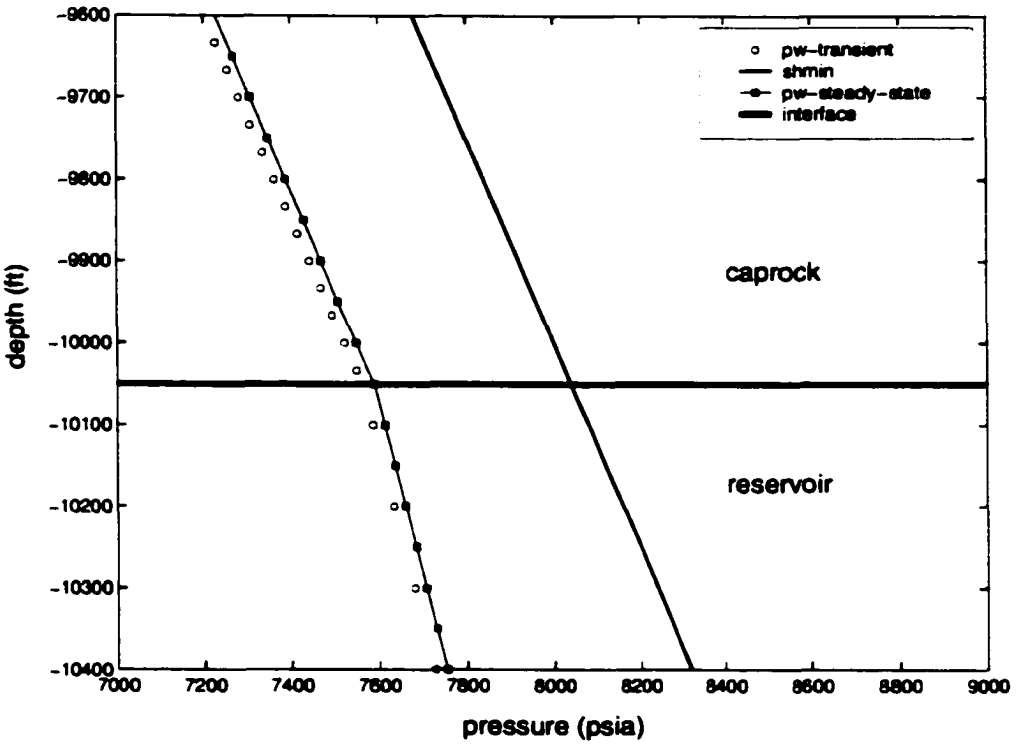

Figure 6.5: The comparison of pressure in a 1-D, single-phase system for a steady-state and transient models near the interface of a caprock and reservoir.

We now examine the pressure build-up at the interface of the caprock and the sand. Figure 6.6 shows the profile when pressure approaches steady state. The sand pressure increases rapidly from hydrostatic to the steady state solution. This behavior mainly is caused by the high permeability in the sand and low permeability in the caprock. The good agreement between the two models at steady state can be observed.

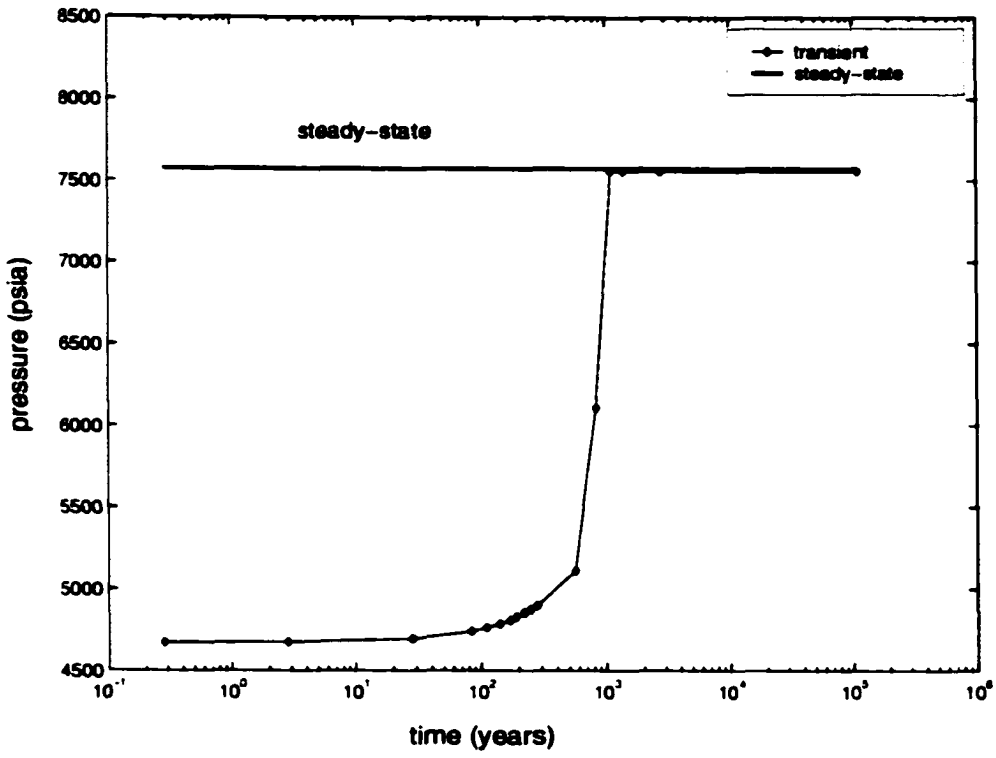

Figure 6.6: Pressure build-up at the interface of a caprock and reservoir in a 1-D, single-phase system for a steady-state and transient models.

6.4.2 Comparison between steady-state and transient models in 2-D case

The 2-D model is shown in Figure 6.7. Similar to the 1-D case, in the 2-D case the system is divided into two different formations. The upper half of the system is a caprock and the lower half is a sand. We then inject water into the base of the system at the three different blocks. Total water injection is $3.\times10^{-06}\ STB/D \cdot ft^2$. The pressure at the top of a caprock is maintained constant at hydrostatic. The initial pressure is hydrostatic and the S_{hmin} gradient is assumed constant 0.8 pst/ft. The fracture spacing is 1000 um.

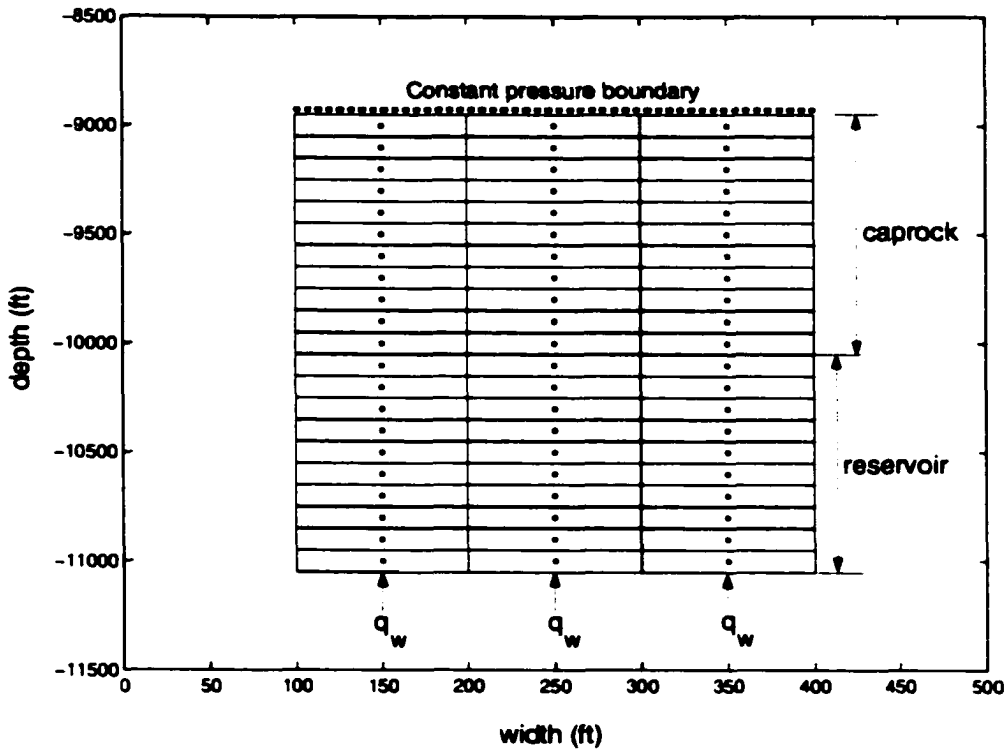

Figure 6.7: Physical representative of a 2-D model describing finite difference gridding and boundary condition.

Figure 6.8 shows the results. The pressure profiles for 2-D cases are given for both steady-state and transient (at steady state) models. In addition, we show the results of the 1-D case. We observe that pressure responses for 1-D and 2-D cases are similar. This is expected since in this case we inject the same flux as we used in 1-D case.

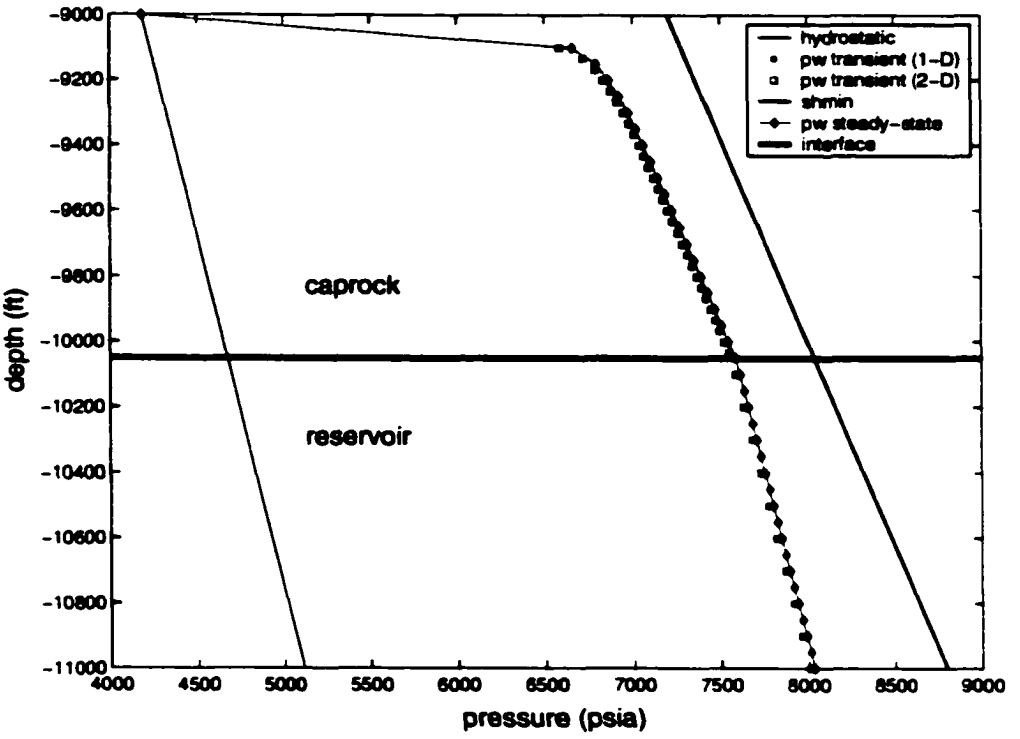

Figure 6.8: The comparison of pressure in steady-state and transient models for 1-D and 2-D systems.

The pressure profiles near the interface between a caprock and sand is given in Figure 6.9. The good agreement between steady-state and transient models is observed.

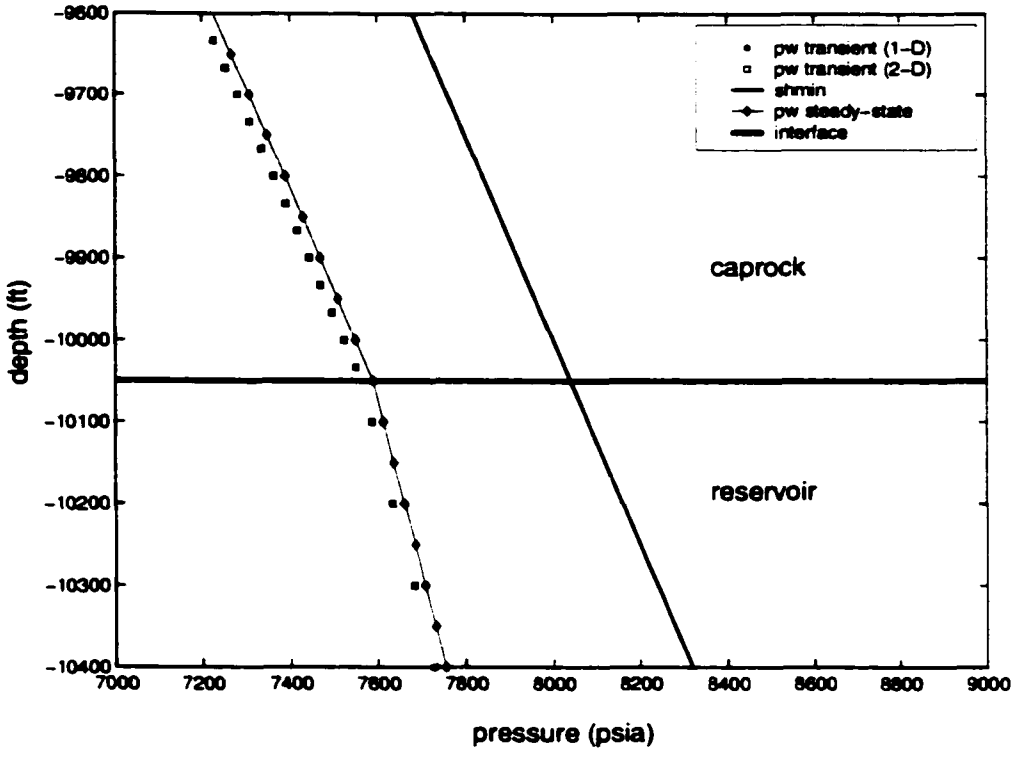

Figure 6.9: The comparison of pressure in 1-D and 2-D, single-phase system for a steady-state and transient models near the interface of a caprock and reservoir.

6.4.3 Transient model in 2-D case with a dip angle

We now present a 2-D case with a dip angle. Figure 6.10 illustrates the case. The dip angle is equal to 30^{o}. The system again is divided into two different formations. At the base and at the top, we assign sand layers and between those two sand layers we assign a caprock. Water ($1.\times10^{-06}$ $STB/D \cdot ft^{2}$) is injected into the system through the base at the deepest position.

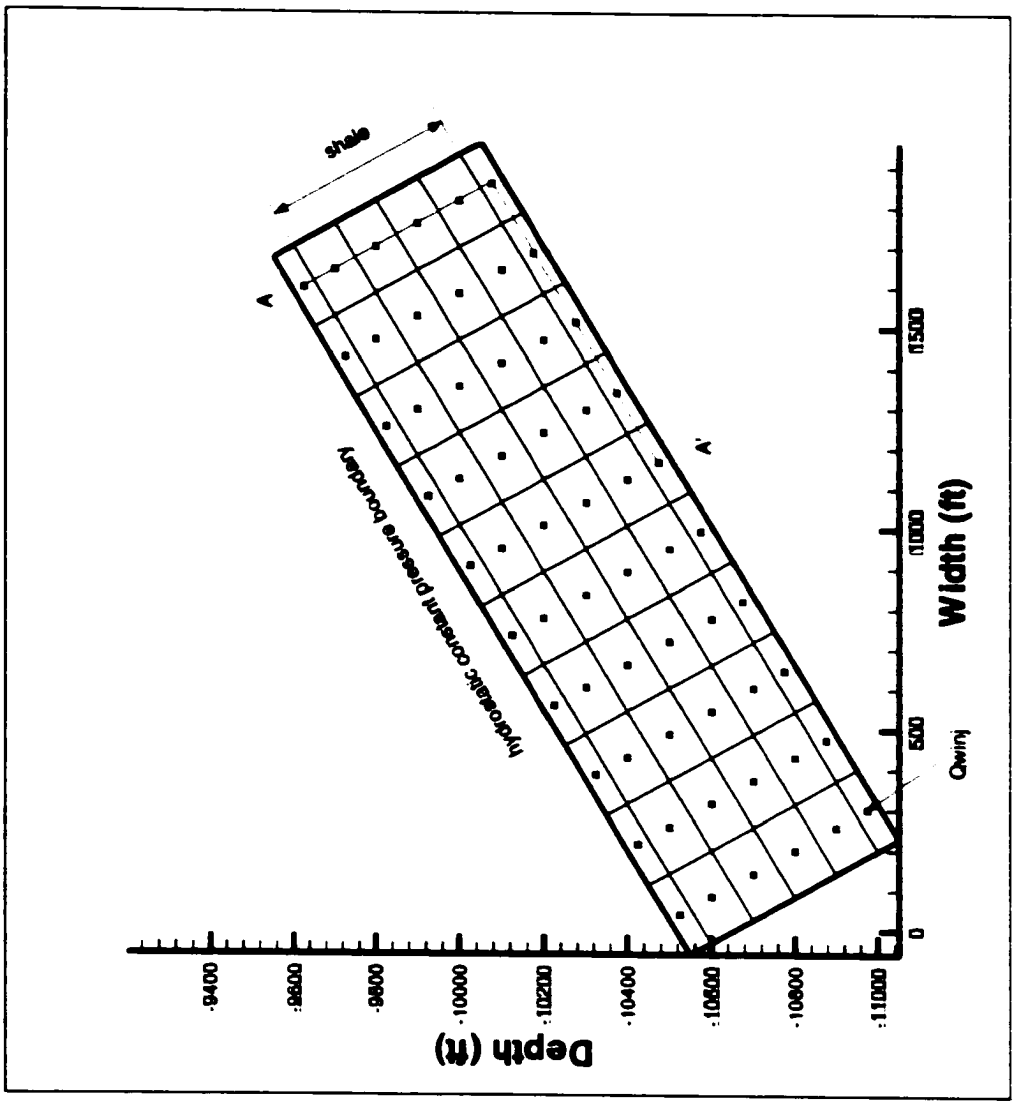

Figure 6.10: Physical representative of a 2-D system with a dip angle.

At the top of formation we impose a hydrostatic constant pressure boundary and at the base we impose a constant flux boundary condition. The S_{hmin} gradient across fractured formation is assumed constant 0.8 psi/ft. In Figure 6.10, the small squares represent the center of the blocks.

Figure 6.11 shows the calculated pressure along $A - A'$ (see Figure 6.10). As in 1-D run, the reservoir sand pressure increases rapidly from hydrostatic to the steady state solution. This behavior is caused by the low permeability of a caprock and the relatively high permeability of the reservoir sand. The pressure build-up in the sand causes the fracture to open wider and increases the permeability in the caprock.

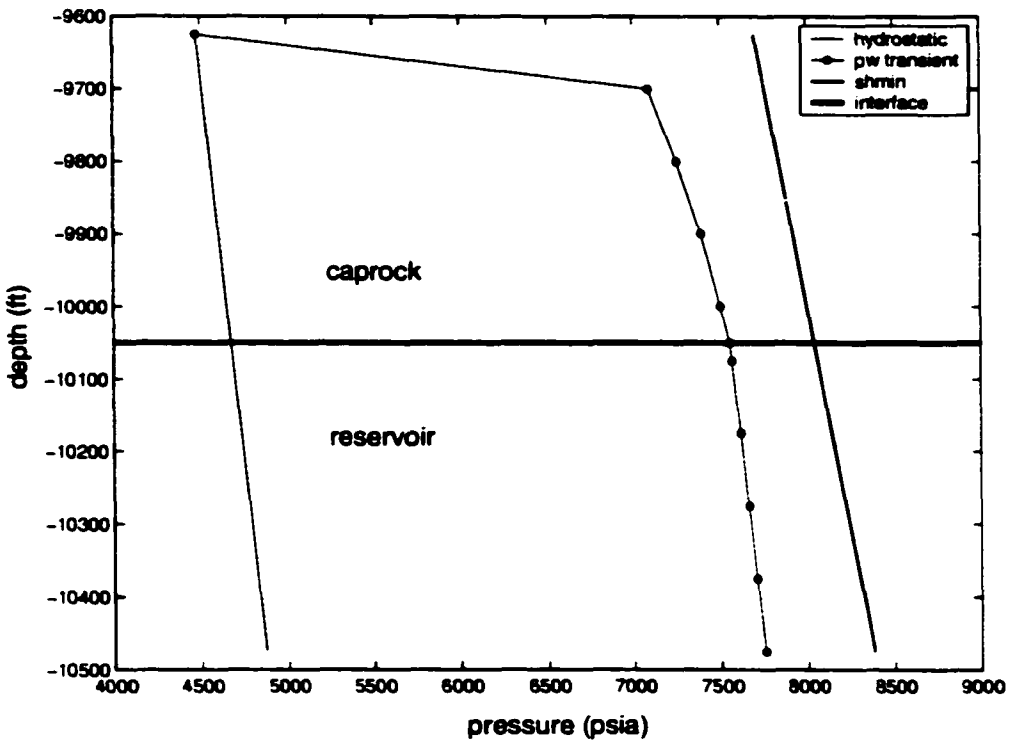

Figure 6.11: Predicted pressure in a 2-D, single-phase system with a dip along $A - A'$ (see also Figure 6.12).

Figures 6.12 to 6.16 show the overpressure and the effective stress distributions of the system at the initial time and steady state. Overpressure is defined as the pressure difference between water pressure and hydrostatic. The comparison between plots at the initial and steady state shows that the pressure of the system (caprock and reservoir) increases. The increased pressure causes the effective stress of the system to decrease.

Figures 6.12 and 6.14 show the distribution of the overpressure in the system. Overpressure at the initial time is equal to zero. We assign the initial pressure equal to the hydrostatic pressure. As the system reaches steady state, the pressure increases as recorded in the high pressure region. However near the upper boundary, the pressure is constant at hydrostatic pressure. This is due to the high permeability of the upper boundary layer and the constant hydrostatic pressure boundary. Comparing to 1-D case, we observe the similar behavior of the pressure respond in a caprock and in the reservoir. The pressure of the caprock increases and at the same time the effective stress (σ_{hmin}) decreases, this causes the permeability of the caprock to increase.

Figures 6.15 and 6.16 describe the distribution of the effective stress at the initial state and steady state. The σ_{hmin} at the initial time is large due to the initial pressure we assign. Figure 6.16 shows the variations of the σ_{hmin} in the system at steady state. We assume that the S_{hmin} is constant thus as the pressure of a caprock increases, the σ_{hmin} decreases. Near the upper boundary layer, the σ_{hmin} is large (area with the red color). However, near the base of the reservoir where we inject water, the σ_{hmin} decreases (area with the yellow color). When we inject water into the system, water moves laterally and vertically, the lateral permeability in the underlying reservoir layer is larger than the vertical permeability ($k_x > k_z$). Thus, water tends to migrate laterally along the underlying reservoir until it reaches the top of the reservoir. The pressure at the top of the reservoir then increases rapidly. This causes the permeability of a

caprock above the top of reservoir to increase and allows the water to breach and move through the caprock. This is indicated by the small σ_{hmin} at the caprock above the top of reservoir (area with the green color).

As given in Table 6.1, lateral permeability of the reservoir layer is 30 md and the vertical permeability is 3 md. For the caprock above reservoir sand layer, the permeabilities (lateral and vertical permeability) are varied depending on the effective stress. The average value of the vertical permeability in a caprock is in order of $1.\times10^{-03}$ md.

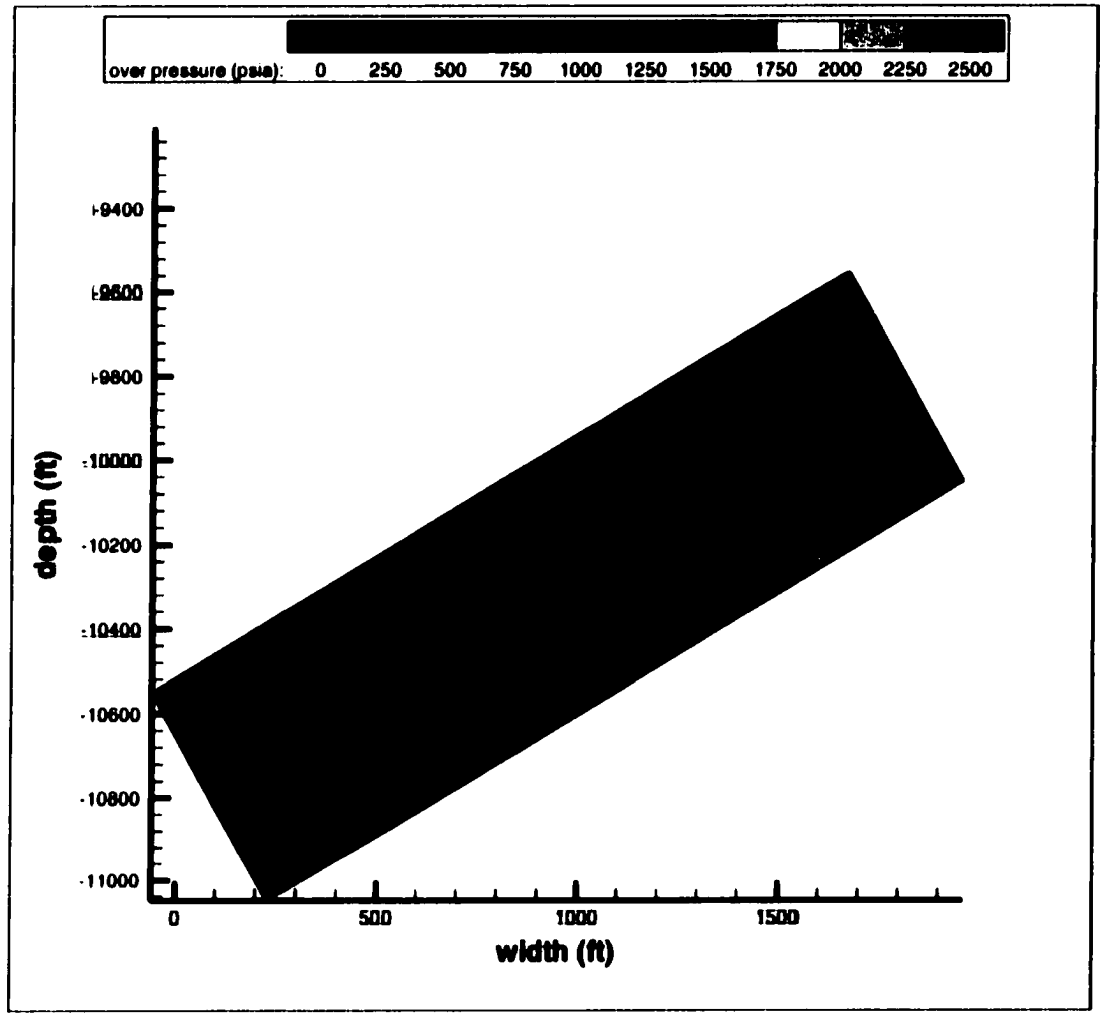

Figure 6.12: Overpressure distribution in a 2-D, single-phase system with a dip at initial time.

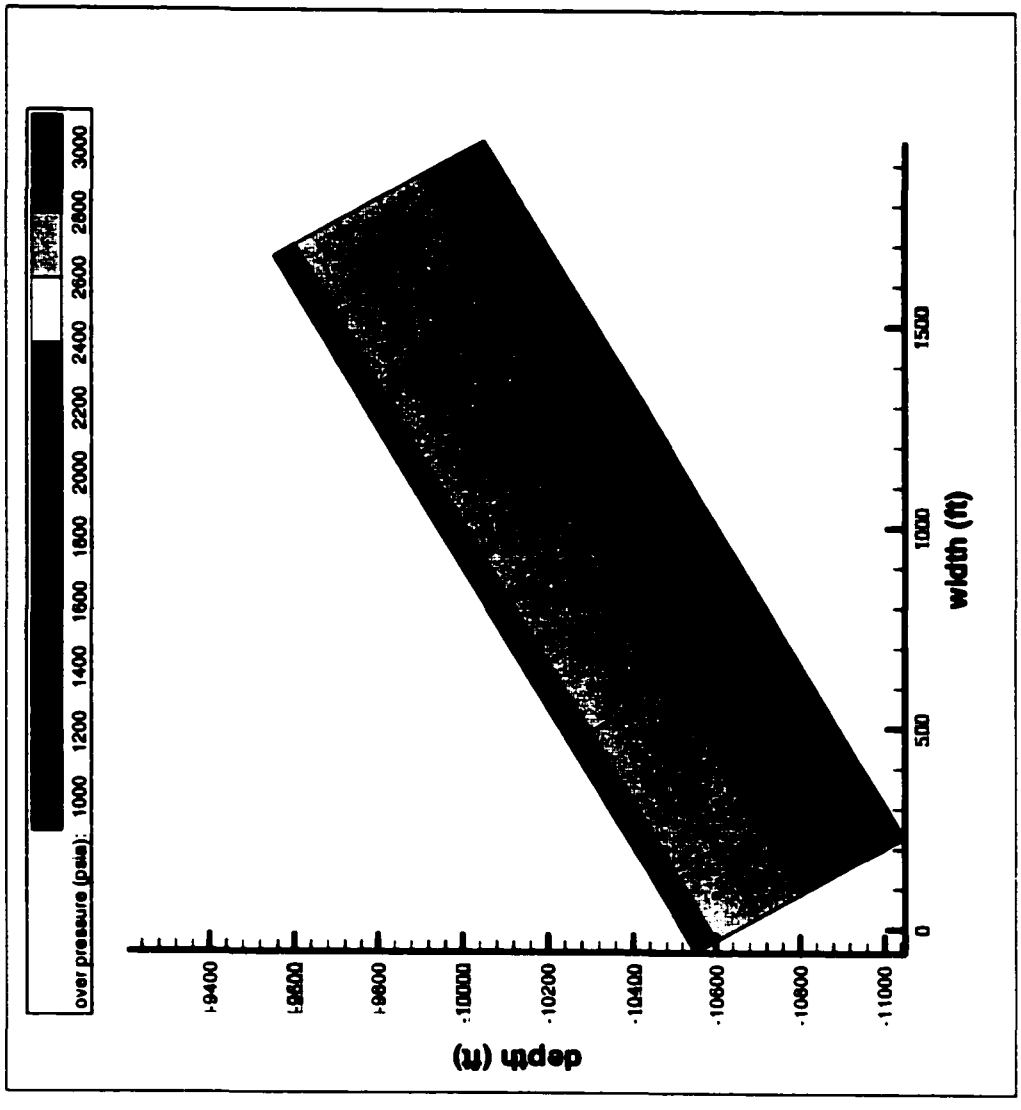

Figure 6.13: Overpressure in a 2-D, single-phase system with a dip at steady state.

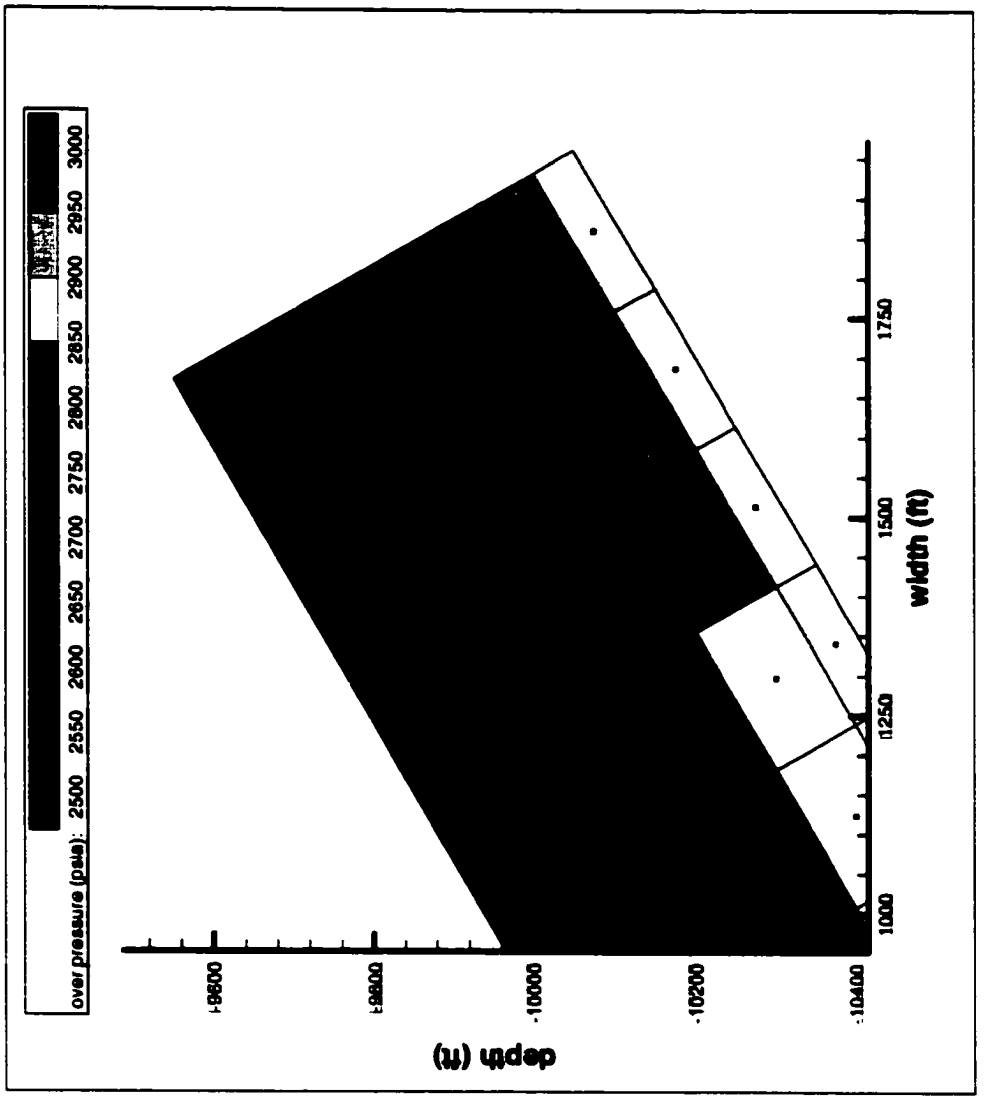

Figure 6.14: Overpressure in a 2-D, single-phase system with a dip at steady state (upper part of the system).

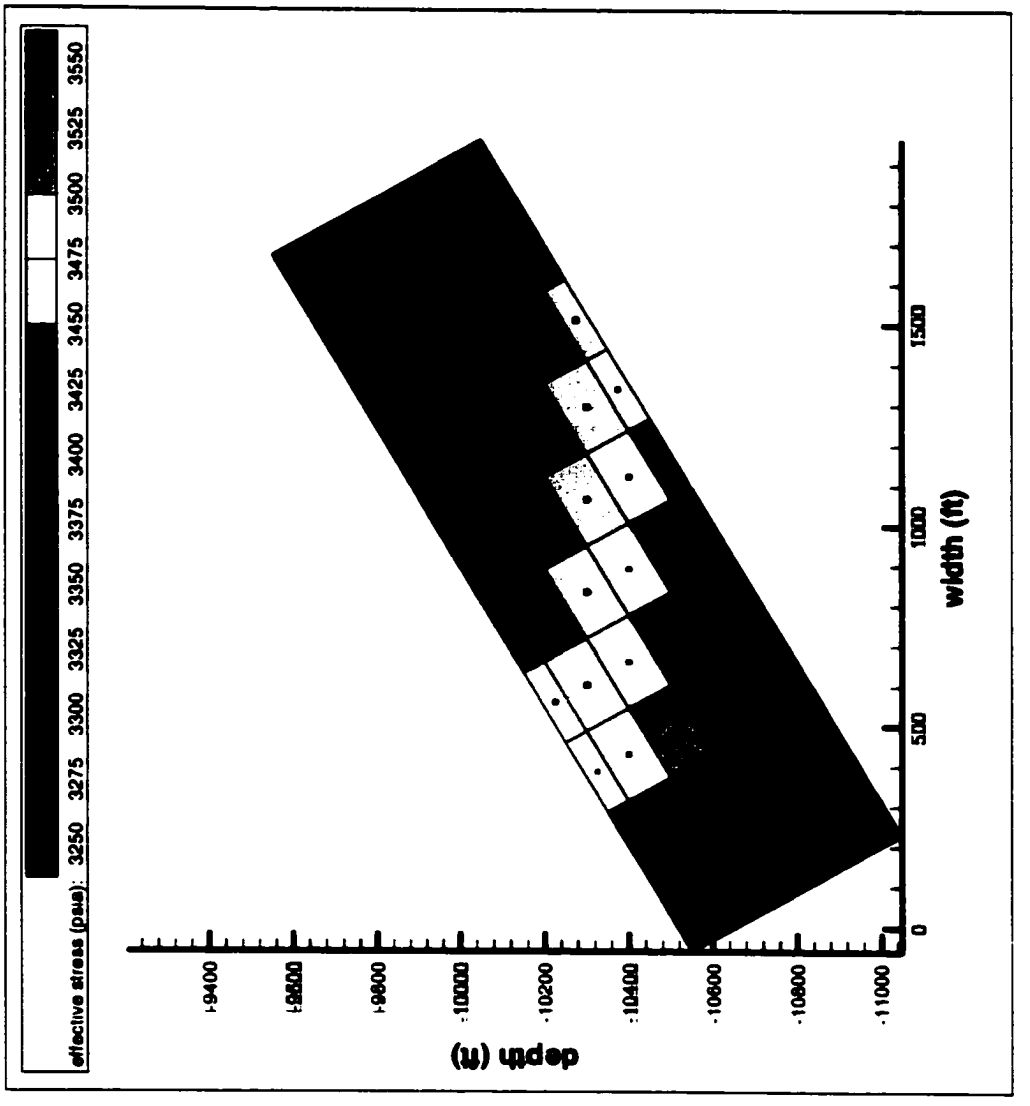

Figure 6.15: Effective stress in a 2-D, single-phase system with a dip at initial time.

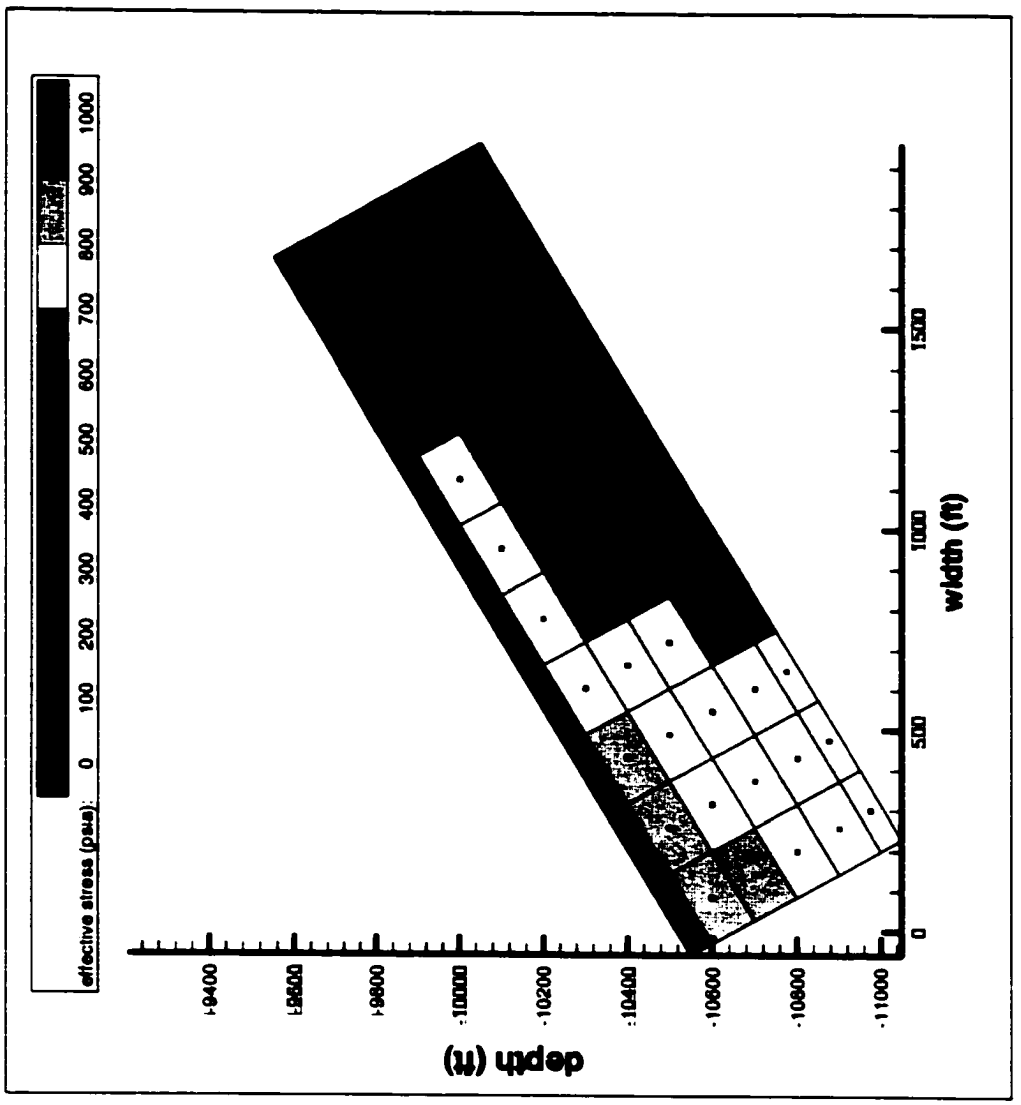

Figure 6.16: Effective stress in a 2-Dimensional system with a dip at steady state.

6.5 Transient two-phase case

We now study the two-phase case for the system presented in Chapter 5 (Figure 5.2) to simulate and to study the behavior of fractured caprock and the gas entrapment. The formation is again divided into sand and shale.

6.5.1 Comparison between steady-state and transient models in 1-D case

We start simulating the two-phase case by injecting water and gas simultaneously through the base of reservoir. $1.\times10^{-09}$ STB/D of water and $1.\times10^{-04}$ SCF/D of gas are injected into the system. The gradient of S_{hmin} is assumed a constant 0.8 psi/ft. A hydrostatic constant pressure boundary is imposed at the top and a constant injection rate for both gas and water is imposed at the base.

Figures 6.17 and 6.18 show the results of the study. The numerical simulation at steady state is compared with the steady-state model. As in the single phase case, the pressure in the sand builds up from the initial hydrostatic pressure to the steady state pressure. The pressure build-up (Figure 6.19) is due to the low permeability of the caprock. As the water pressure increases, the permeability of a caprock increases (Figure 6.20) allowing the fluid to flow. The caprock permeability increases due to the decrease in effective stress. This process continues until the system reaches steady state. Figure 6.20 describes the permeability of the caprock near to the interface.

From Figure 6.20, we also observe the rapid change of the caprock permeability as the system approaches steady state. The permeability of the caprock depends on the fracture width and the fracture width depends on the effective stress. We have known from the hydraulic behavior study (Chapter 4) that the permeability is proportional to the cube of the fracture width. Thus, the small change in the fracture width results in the big change in the permeability shown in Figure 6.20.

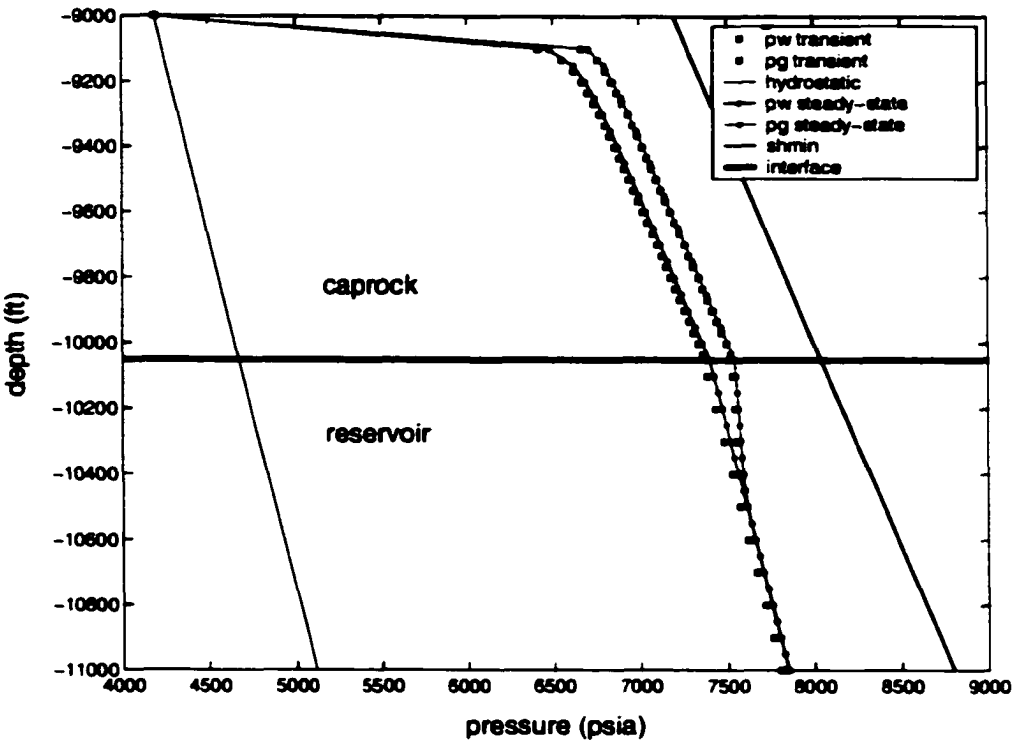

Figure 6.17: The comparison of pressure in 1-D, two-phase system for steady-state and transient models.

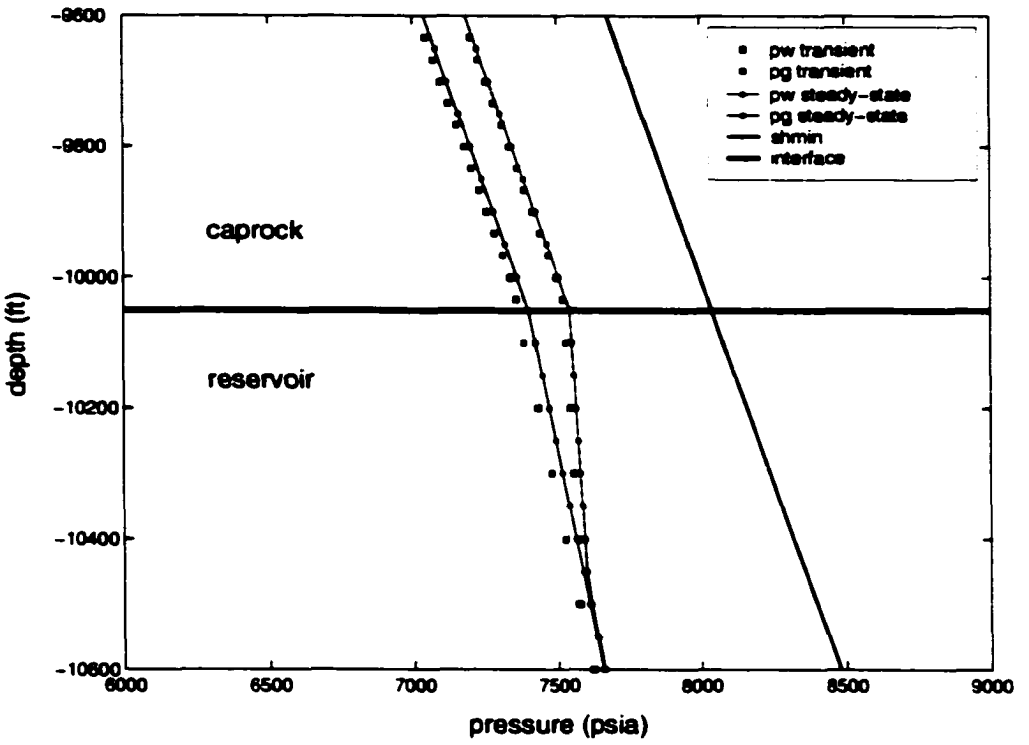

Figure 6.18: The comparison of pressure in 1-D, two-phase system for steady-state and transient models near the interface of a caprock and reservoir.

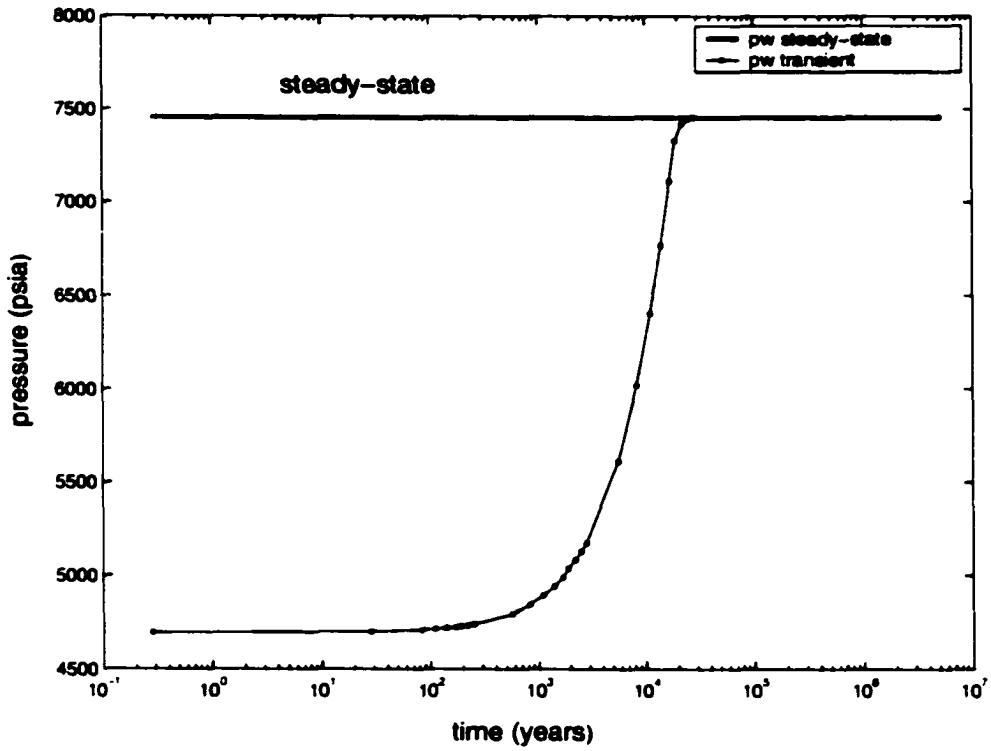

Figure 6.19: Water pressure build-up in the reservoir vs. simulation time.

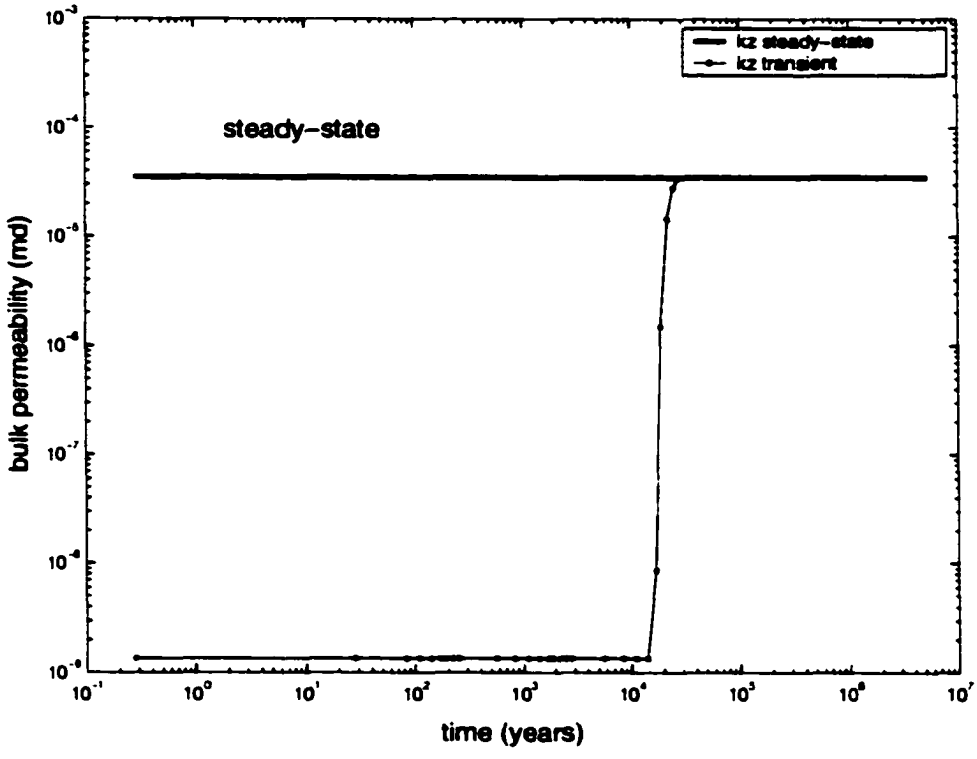

Figure 6.20: Permeability of a caprock vs. simulation time.

Figures 6.21 and 6.22 show steady state saturations. As the system approaches steady state some gas is trapped in the sand below the caprock. The transient (at steady state) and steady-state models are in good agreement with each other. The gas trapped below the caprock at steady state can be described by capillary pressure relationship of the two formations. Because the pressure is continuous across the interface between the two formations the capillary pressure must also be continuous. Since different capillary pressure curves apply to the two formations, there is a discontinuity in the saturations across the interface. The fluid fluxes determine the fracture permeability, the caprock capillary pressure and the gas relative permeability. The gas relative permeability then determines the saturations in the caprock (Figure 6.23.a). This information can then be used to determine the saturations in the sand (Figure 6.23.b). The capillary

pressure can be converted for a gas column height ($h_g = \frac{P_c}{(\rho_w - \rho_g)g}$). This gas column strongly depends on the fracture width in the caprock as shown in Eqn. 5.10.

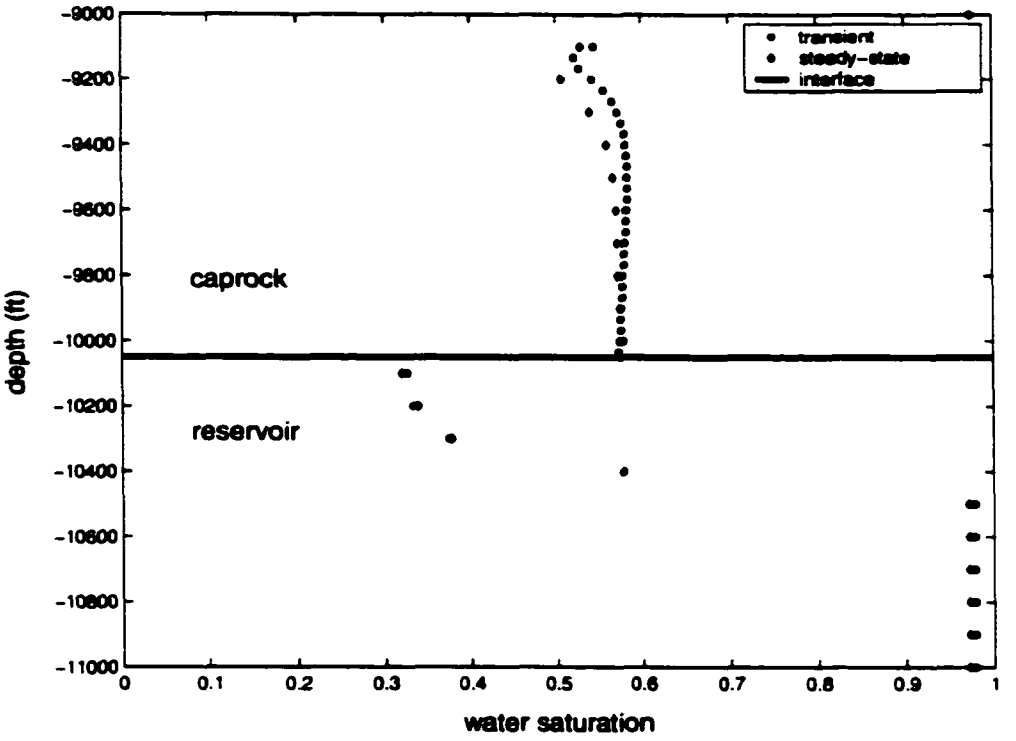

Figure 6.21: The comparison of water saturation in 1-D, two-phase system for steady-state and transient models.

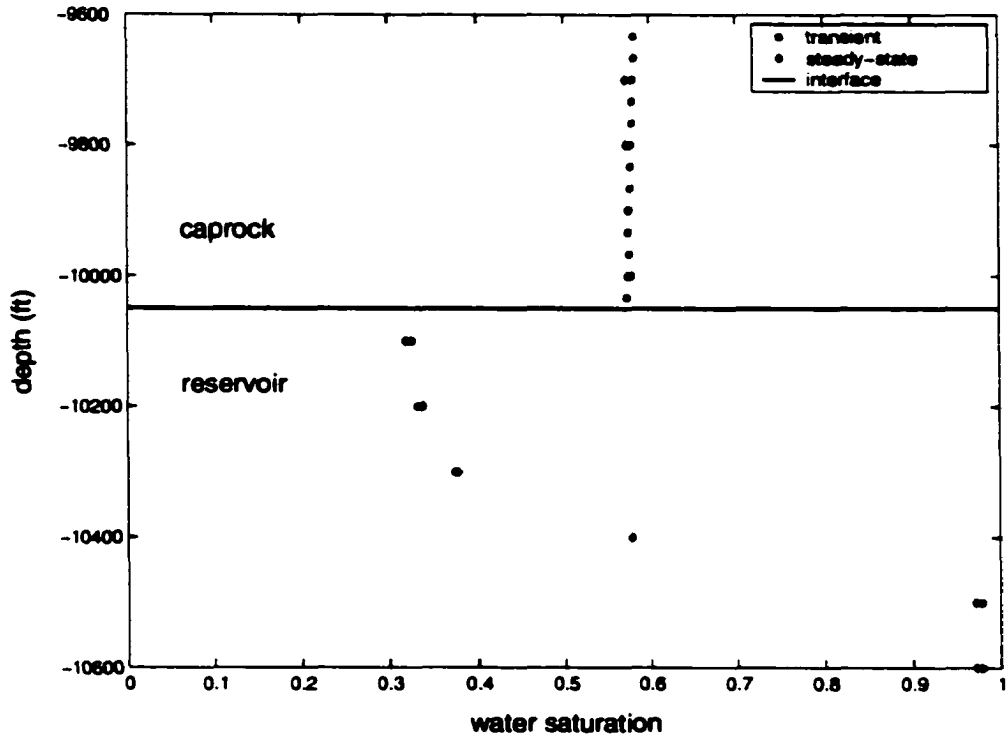

Figure 6.22: The comparison of water saturation in 1-D, two-phase system for steady-state and transient models near the interface of a caprock and reservoir.

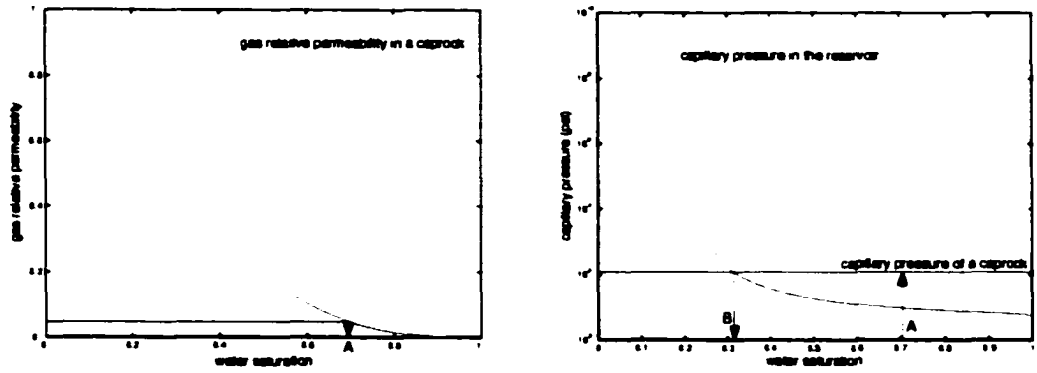

a) Gas relative permeability in a caprock b) Capillary pressure in a caprock and reservoir

Figure 6.23: Gas relative permeability and capillary pressure relationships illustrating the existing relationships between caprock saturation and reservoir saturation. The fluid fluxes determine the gas relative permeability and a caprock capillary pressure. The gas relative permeability then determines the saturation in a caprock (Figure 6.23.a). Since different capillary pressure relationships apply to the caprock and reservoir, there is a discontinuity in the saturations across the interface. At steady state, the capillary pressure at the interface of the two formations is the same.Thus the saturation in the caprock (point A) can be used to determine the saturation in the reservoir (point B) (Figure 6.23.b).

6.5.2 Comparison between steady-state and transient models in 2-D case

Again Figure 6.7 is used in this study. Similar to the 1-D two-phase case, the system is divided into two formations and then we impose hydrostatic pressure at the top of the caprock and constant injection rate for both gas and water at the base. The injection rate for water is $3\times10^{-09}\ STB/D\cdot ft^2$ and the injection rate for gas is 3 $SCF/D\cdot ft^2$.

Figures 6.24 and 6.25 show the results of the study. We again observed a similar behavior between 1-D and 2-D two-phase cases. Initially the sand pressure increases because water and gas are injected into the sand which has a relatively high permeability. The increased pressure in the sand causes the effective stress in the caprock to decrease and thus increases the fracture width of a caprock. The fracture width becomes wider and the permeability of the caprock becomes larger. The gas saturation in the sand below the caprock increases which reflects the entrapment of gas. The same gas column height is observed in the 1-D and 2-D cases because the injection rates of water and gas and boundary condition are the same in both cases. Figures 6.26 and 6.27 show the saturations in the sand and a caprock.

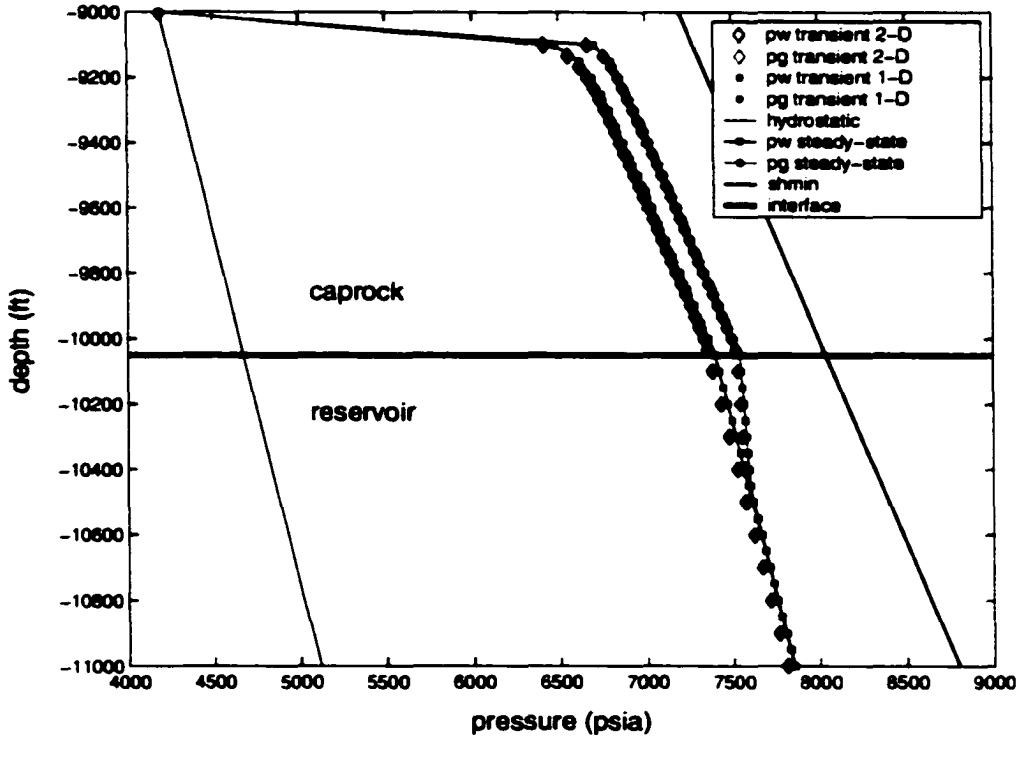

Figure 6.24: The comparison of pressure in 2-D, two-phase system for steady-state and transient models.

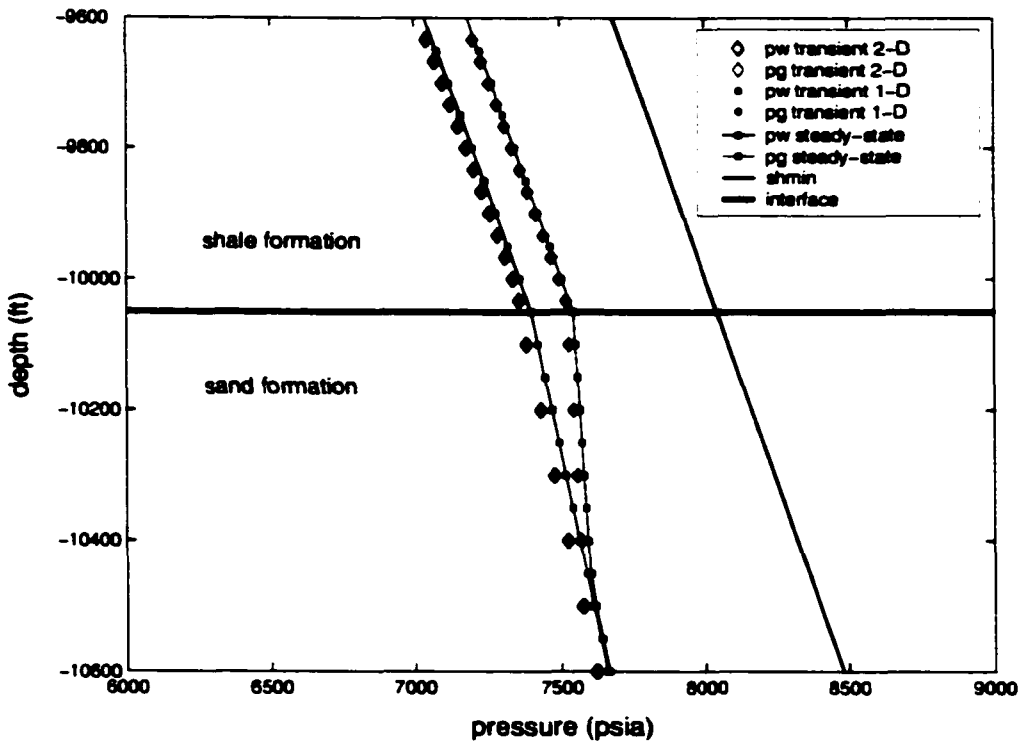

Figure 6.25: The comparison of pressure in 2-D, two-phase system for steady-state and transient models near the interface of a caprock and reservoir.

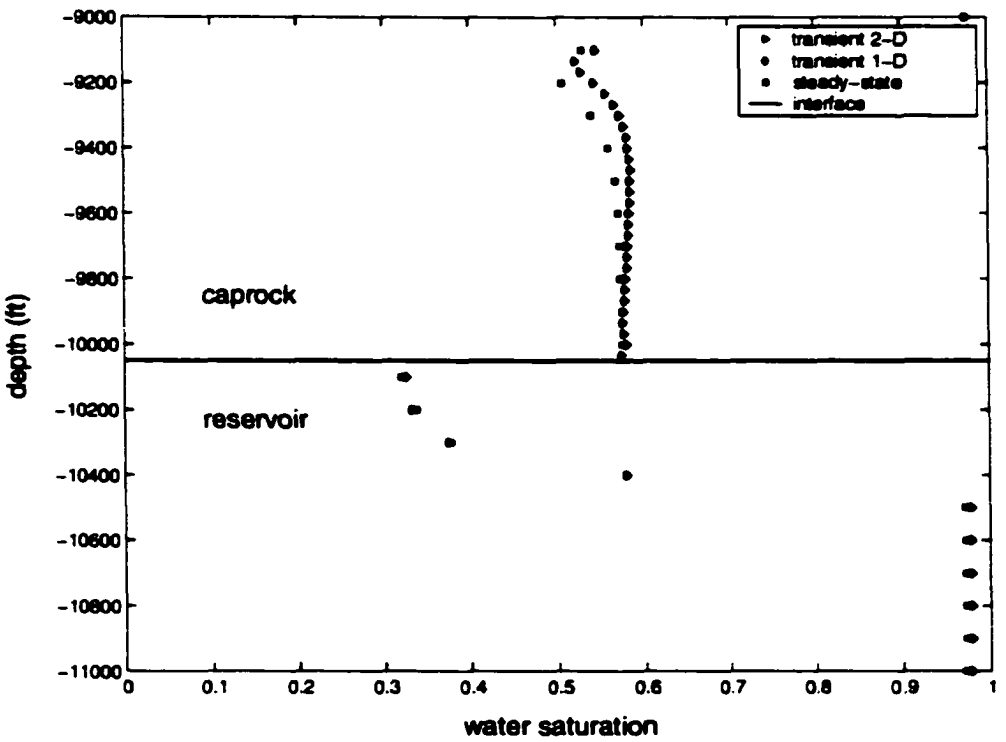

Figure 6.26: The comparison of water saturation in 2-D, two-phase system for steady-state and transient models.

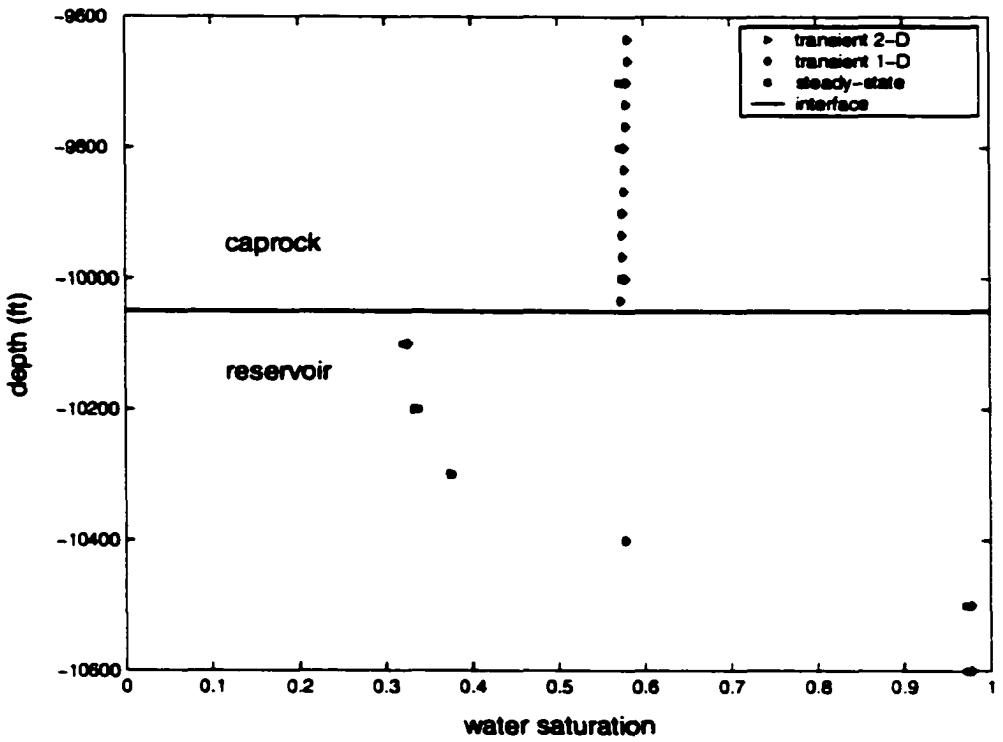

Figure 6.27: The comparison of water saturation in 2-D, two-phase system for steady-state and transient models near the interface of a caprock and reservoir.

6.5.3 Transient model in 2-D (dip) case (low-rate case)

We now simulate the 2-D case where the system has a dip as shown in Figure 6.10. The dip is 30^o with respect to the x-direction. Similar to the 2-D and single-phase cases presented before, we impose a constant pressure boundary at the top of formation and constant injection rate at the base of the formation. The system is divided into three formations (two sands and one caprock). The sand layers are at the top and at the base of the model with the caprock in the middle.

To study this case, we inject $2.5\times10^{-08}\ STB/D\cdot ft^2$ of water and 3.75×10^{-04} $SCF/D\cdot ft^2$ of gas into the base of the system. We assume the minimum horizontal stress (S_{hmin}) gradient is a constant 0.8 psi/ft.

Figure 6.28 shows the steady state pressure profile along the path $A-A'$ (see Figure 6.10). The pressure in the sand below the caprock increases because of the fluid injection and the low permeability of the caprock. The pressure increases the fracture width due to the lower effective stress. As before, gas is trapped below the caprock. This behavior is the same as we observe in 1-D case. Saturation profile along path $A-A'$ is given in Figure 6.29.

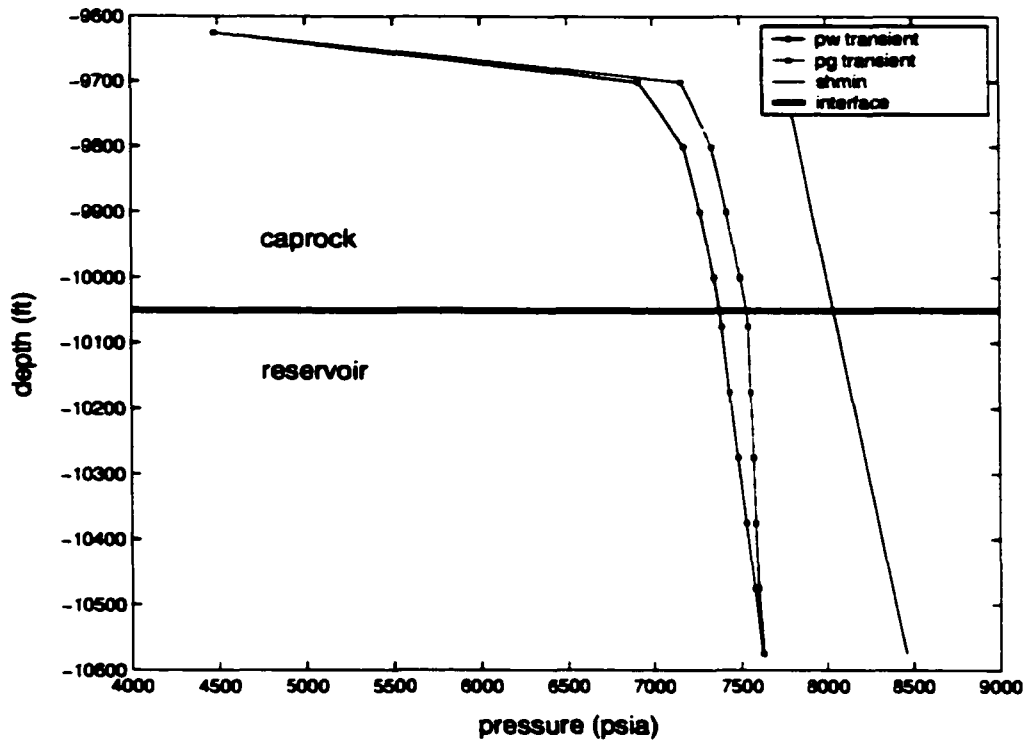

Figure 6.28: Predicted pressure in a 2-D, two-phase system with a dip along $A - A'$ (see also Figure 6.10).

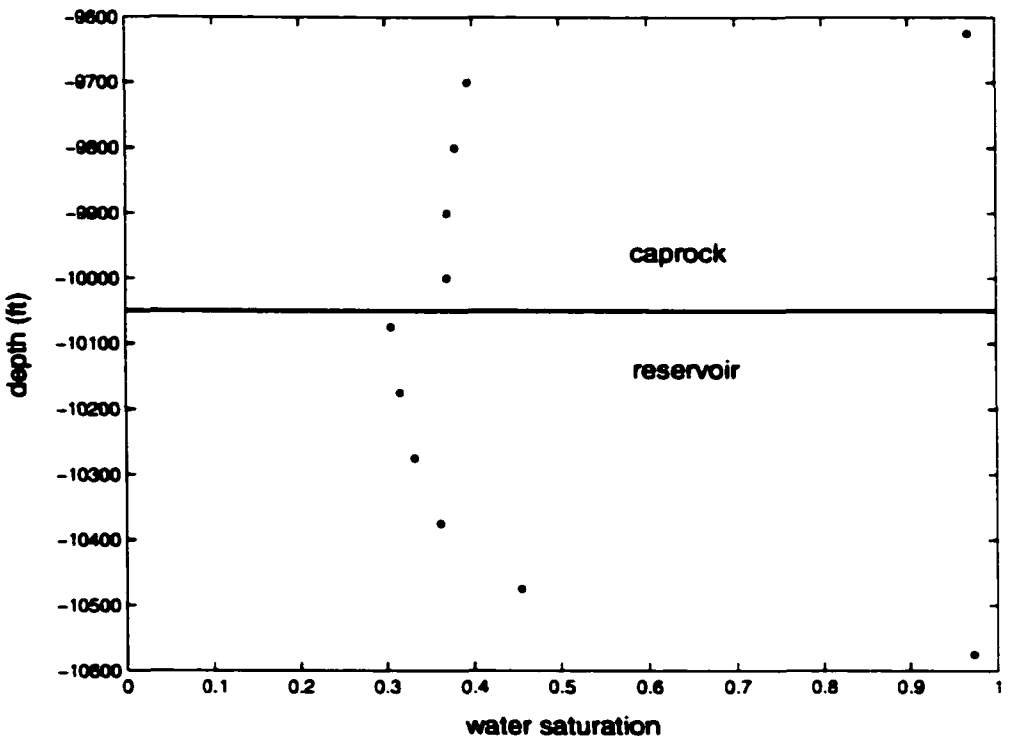

Figure 6.29: Predicted water saturation in a 2-D, two-phase system with a dip along $A - A'$ (see also Figure 6.10).

Figures 6.30 through 6.36 describe overpressure, effective stress, and saturation profiles of the system as the system approaches steady state. In Figures 6.31 and 6.32 we observe pressure buildup along the underlying reservoir below the caprock. The behavior is the same as observed in 1-D case. The high permeability in the reservoir and the low permeability in the caprock cause pressure build-up in the reservoir. At the initial time, the overpressure for all computed grid blocks equal to zero (Figure 6.30). Near the upper boundary layer, the pressure is constant at hydrostatic due to the boundary condition imposed to the system. The region near the base of the reservoir where water and gas are injected and the region near the top of the lower reservoir, the

overpressure is large which indicates a pressure build-up in the caprock and lower reservoir.

Figures 6.33 and 6.34 show the distribution of the effective stress in the system. In a two-phase system, we calculate the effective stress (σ_{hmin}) based on the water pressure. The distribution of the σ_{hmin} at the initial time is shown in Figure 6.33. Similar to the single-phase case previously, at the initial time the σ_{hmin} for all blocks is large due to the initial pressure we assign to the system. The pressure responses are similar to the single-phase case. The high lateral permeability in the reservoir causes gas and water move laterally through the reservoir. The pressure at the top of reservoir then increases rapidly due to the low permeability the caprock. The increase of pressure in a caprock causes the effective stress to decrease. Following the decrease in effective stress, the caprock permeability increases. This allow the gas and water breach the caprock and migrate vertically through the caprock.

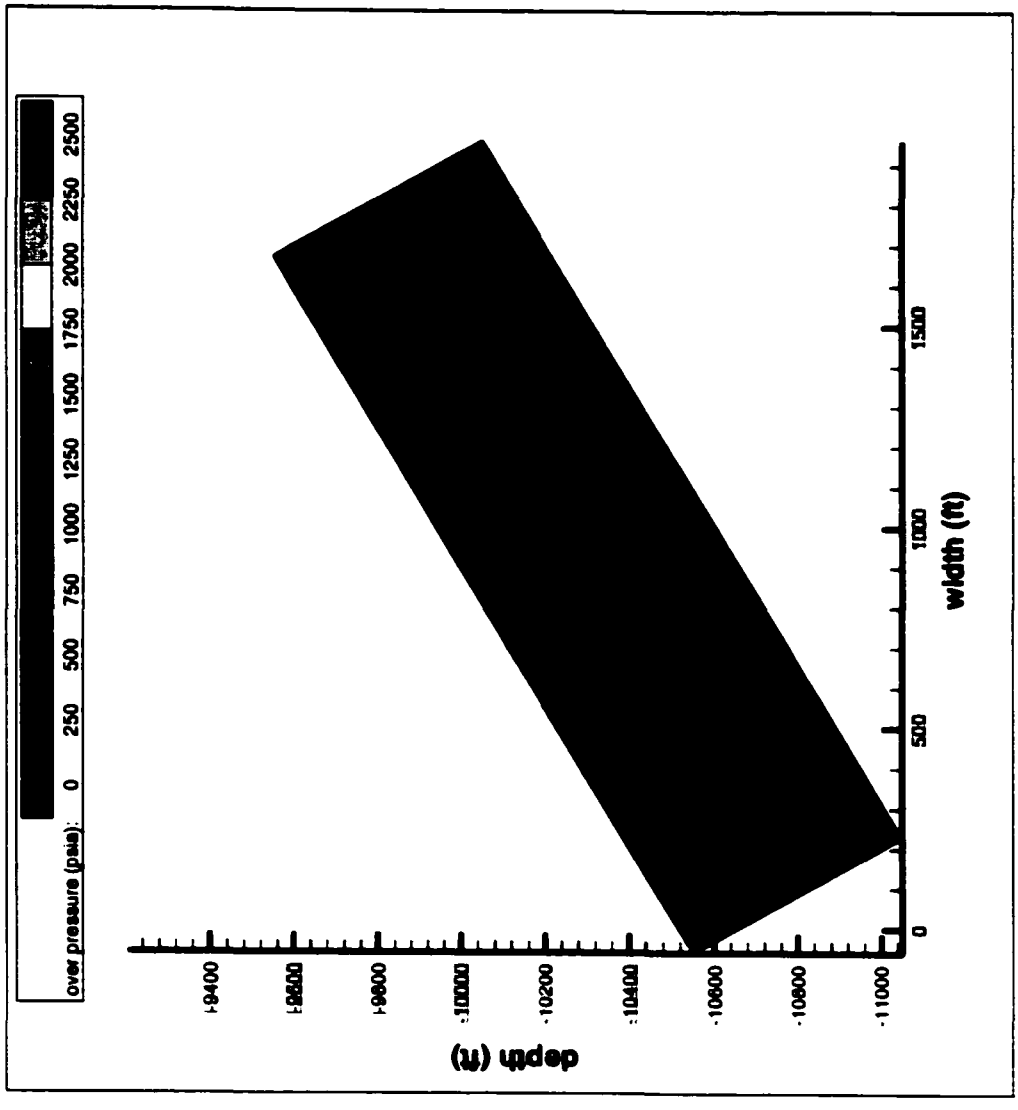

Figure 6.30: Overpressure in a 2-D, two-phase system with a dip at initial time.

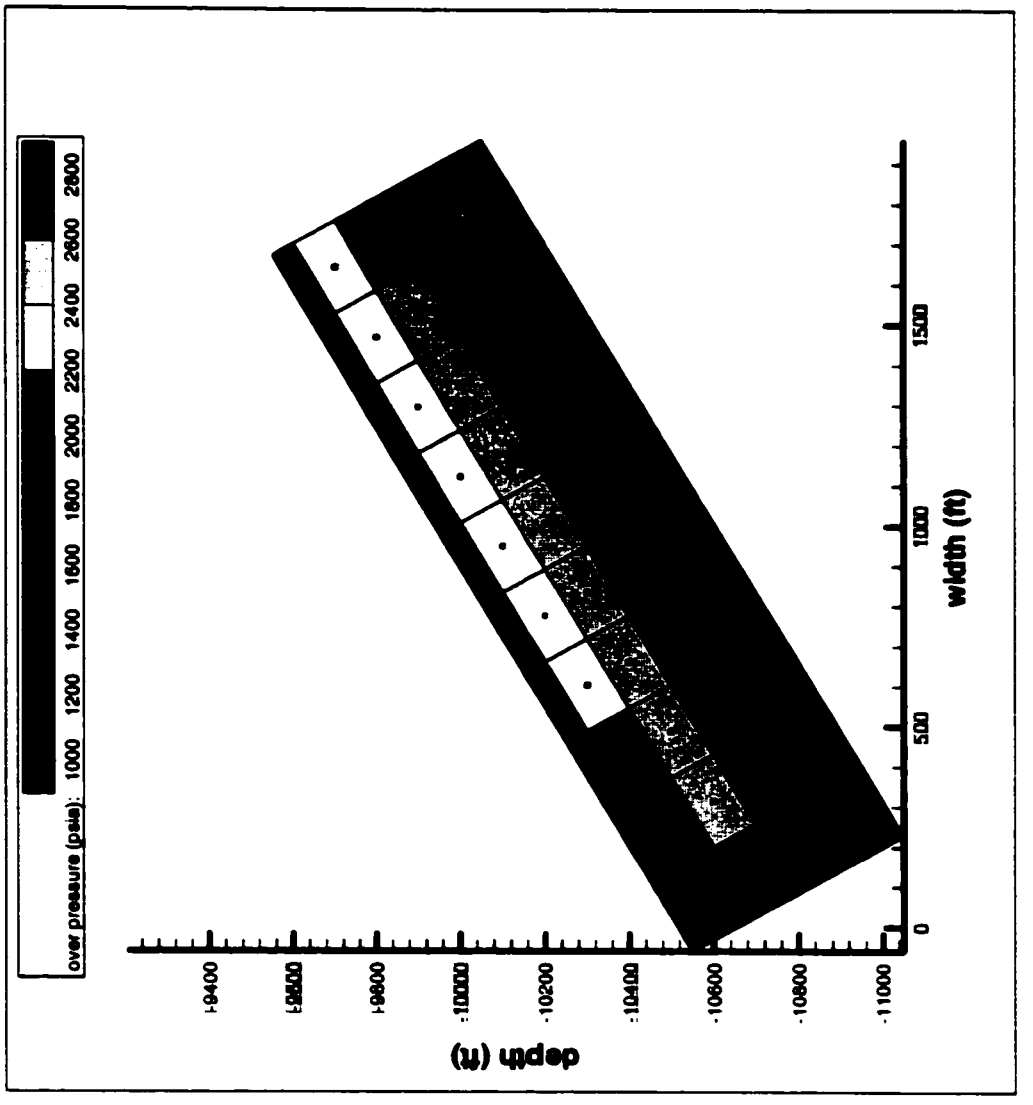

Figure 6.31: Overpressure in a 2-D, two-phase system with a dip at steady state.

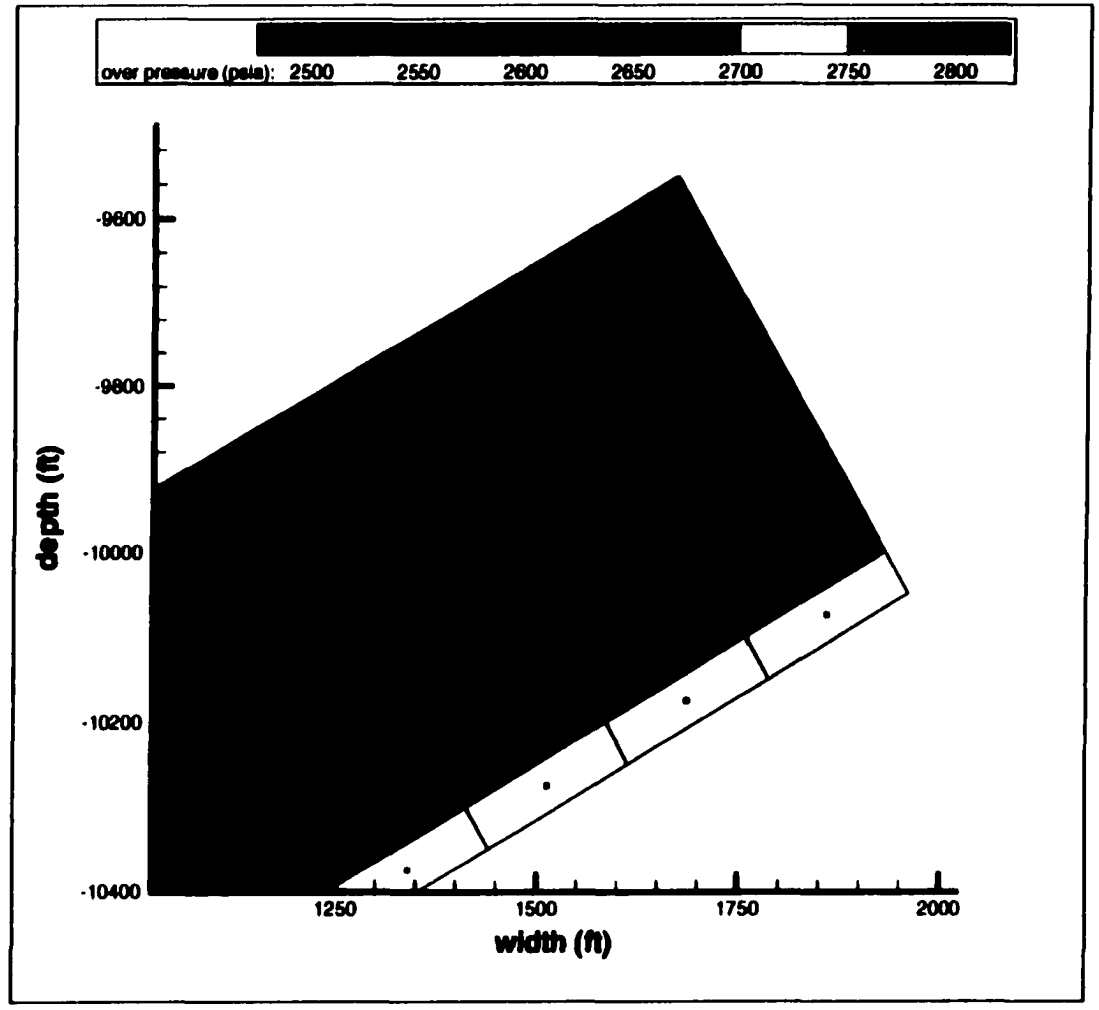

Figure 6.32: Overpressure in a 2-D, two-phase system with a dip at steady state (upper part of the system).

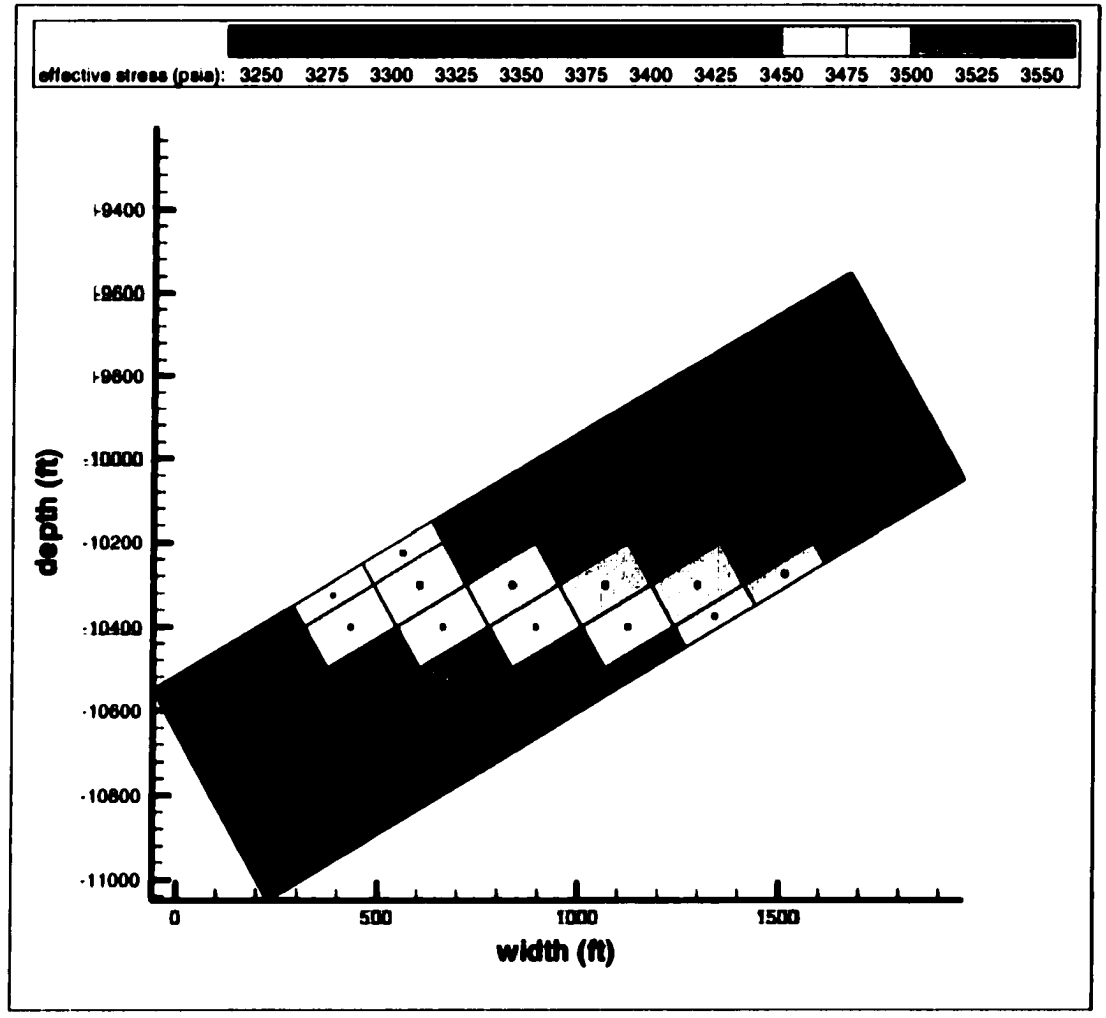

Figure 6.33: Effective stress in a 2-D, two-phase system with a dip at initial time.

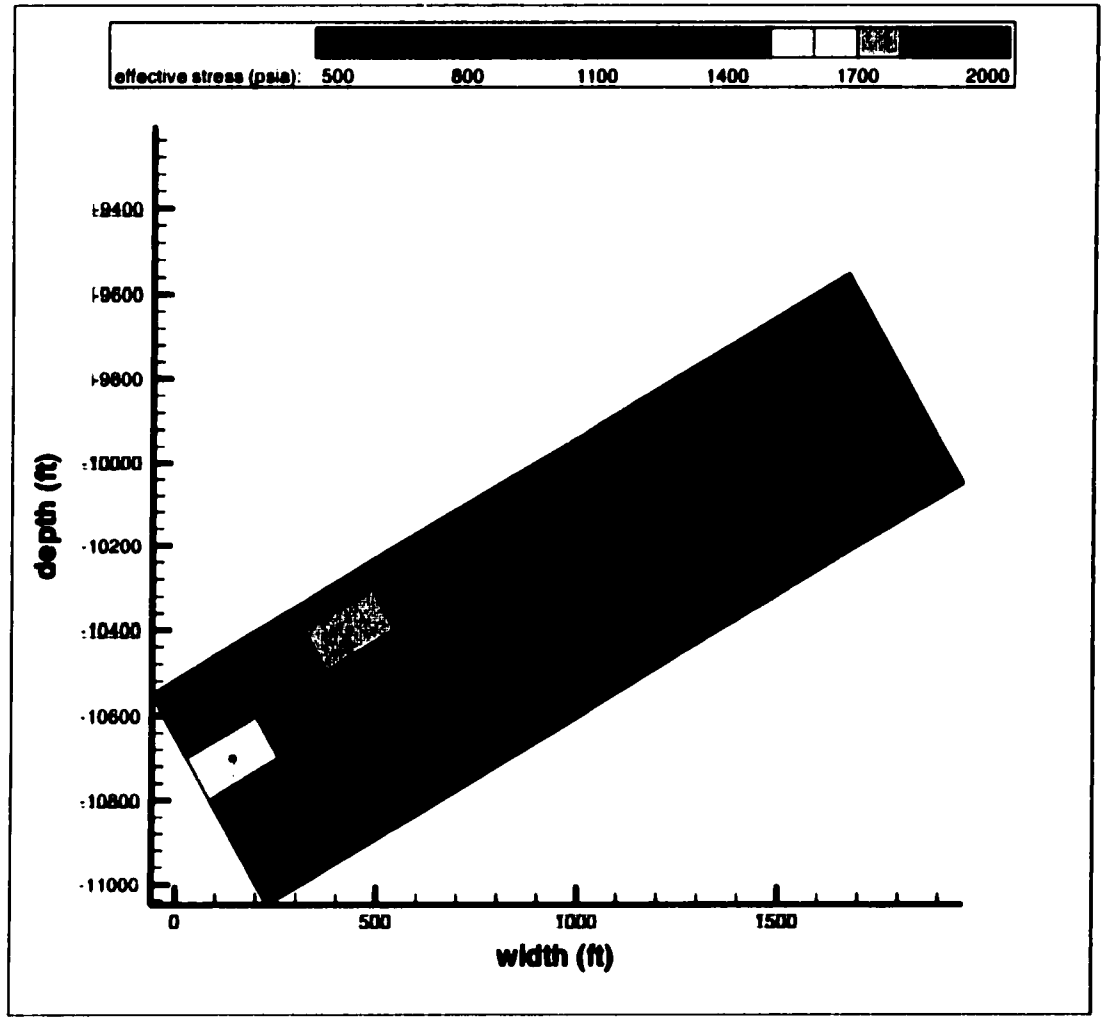

Figure 6.34: Effective stress in a 2-D, two-phase system with a dip at steady state.

Figures 6.35 and 6.36 show the distribution of the water saturation in the system. Initially the water saturation in the system is 100%. From the base of the reservoir, gas and water are injected simultaneously to simulate the hydrocarbon migration. From Figure 6.34, we observed that as the water and gas enter the system, the σ_{hmin} decreases allowing the fluids to migrate vertically through the caprock. For gas to enter the fracture, the capillary pressure must exceed the displacement pressure of the fracture. Initially the displacement pressure of the caprock is high as indicated by the high σ_{hmin}. However, when the system approaches steady state, the σ_{hmin} becomes smaller and the permeability of a caprock becomes larger. The fracture width that determines the permeability increases. This allows the displacement pressure to decrease. Figure 6.35 shows that the accumulated gas at the top of the reservoir as recorded in the high gas saturation in that region.

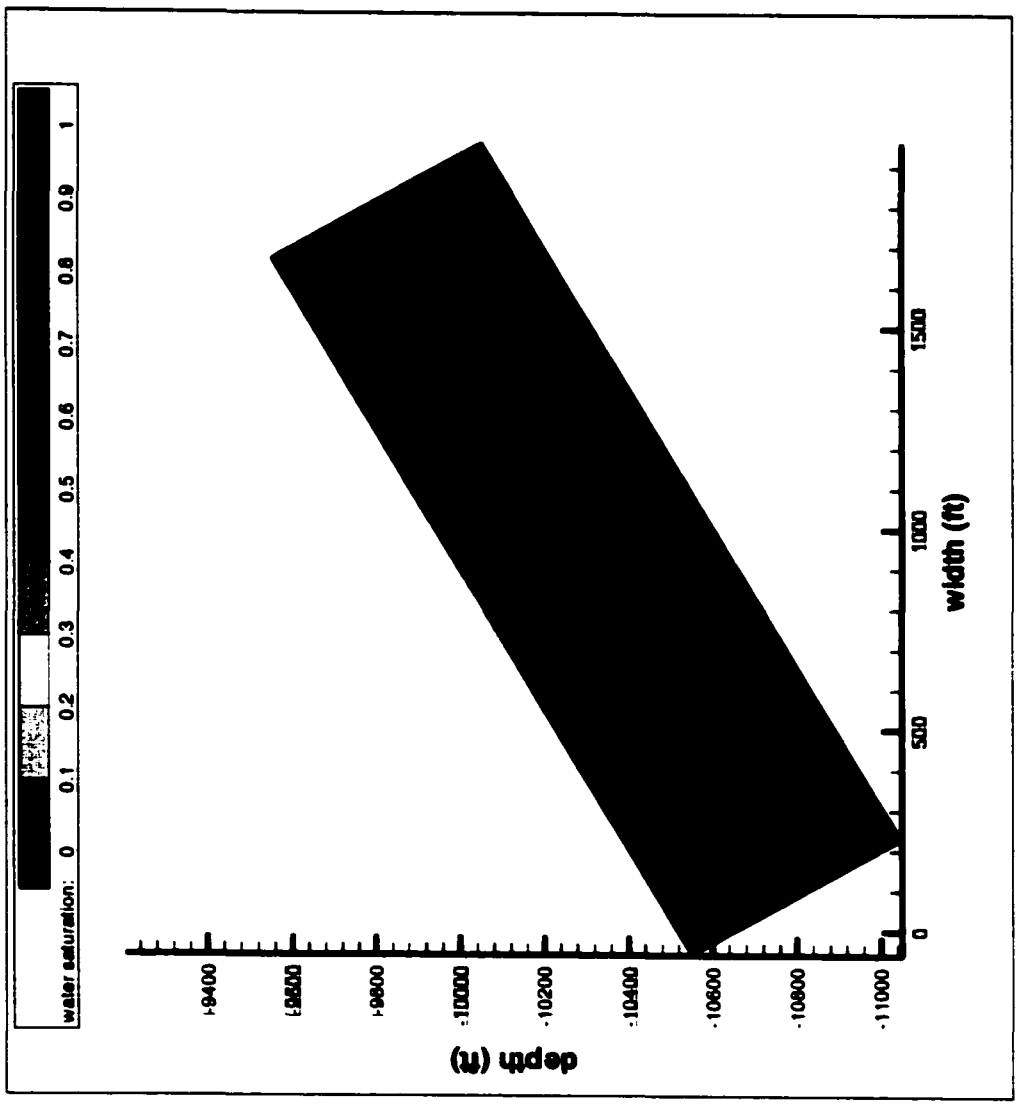

Figure 6.35: Water saturation in a 2-D, two-phase system with a dip at initial time.

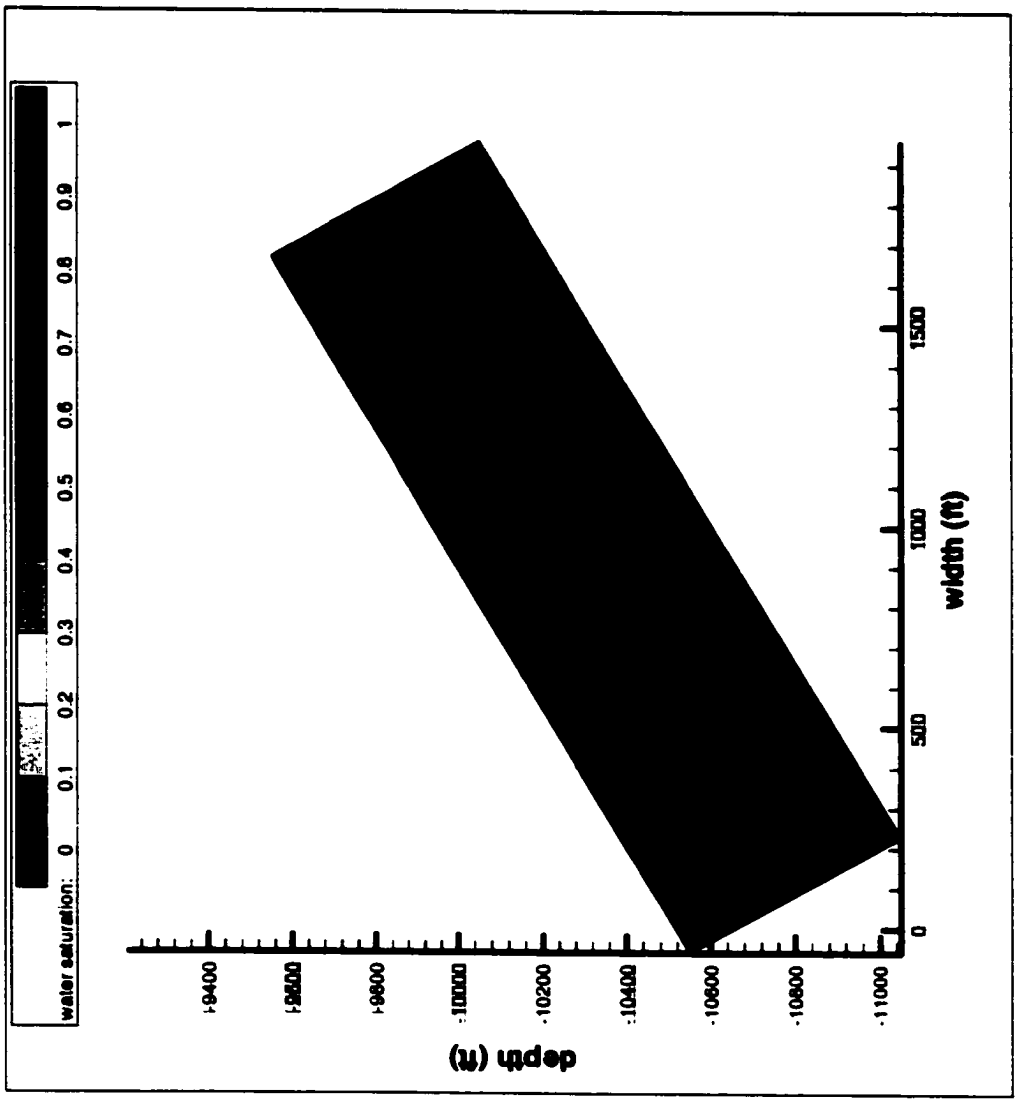

Figure 6.36: Water saturation in a 2-D, two-phase system with a dip at steady state.

Figures 6.37 and 6.38 show the vector flows for gas and water for the system. The velocity vectors in the x and z-directions are defined to describe the direction of fluid flow. We observe that most gas escape from the top of the reservoir. This is expected since at the top of reservoir, the fracture permeability is high as recorded in low effective stress and high overpressure of that region (Figures 6.30 and 6.34). Gas velocity in the x-direction for that region (a caprock with the green color) varies from 1×10^{-06} to 1×10^{-07} ft/D. In the z-direction the velocity is more uniform (in the order of 1×10^{-04}.

Figure 6.38 shows the flow direction of the water. The gas saturation at the top of the reservoir is high which causes the low relative permeability for the water in the region. As a results, instead of moving laterally through the high permeability reservoir, water tends to move vertically. This causes an increase in the caprock permeability. In a caprock water velocity in the x-direction varies from 1×10^{-10} to 1×10^{-12} ft/D. In the z-direction water velocity is more uniform (in the order of 1×10^{-10} ft/D). For the underlying reservoir, we observe that water velocity in the x-direction is larger than the velocity in the z-direction. Water velocity in the x-direction is in the order of 1×10^{-08} ft/D while water velocity in the z-direction is in the order of 1×10^{-09} ft/D.

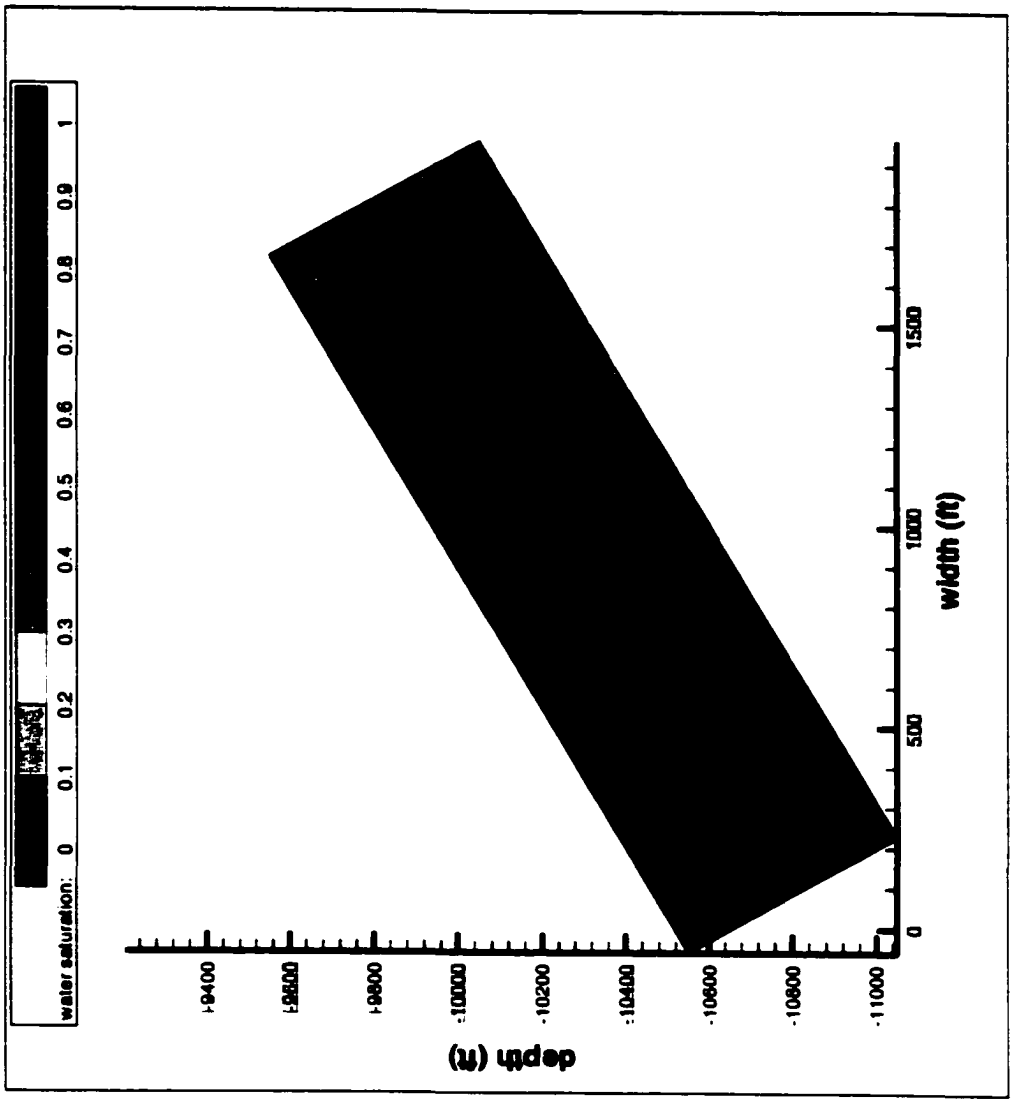

Figure 6.37: Vector flow of gas in a 2-D, two-phase system with a dip at steady state.

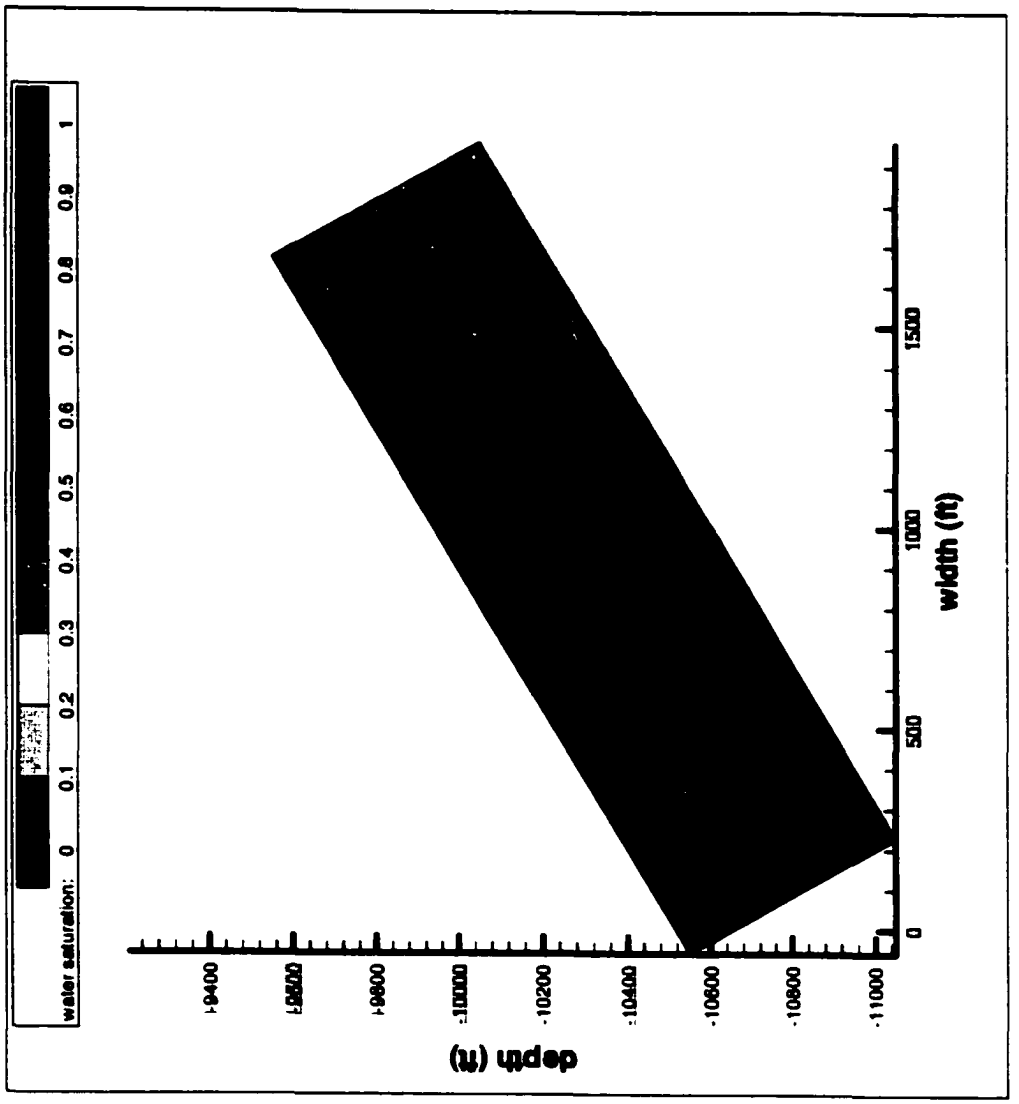

Figure 6.38: Vector flow of water in a 2-D, two-phase system with a dip at steady state.

6.5.4 Transient model in 2-D (dip) case (high-rate case)

We now increase the water influx for the 2-D (dip) case (Sec. 6.5.3) to study the effect of water influx on gas column height. We increase water rate by one order magnitude from the previous run. Water 0.25×10^{-06} $STB/D \cdot ft^2$ and gas 3.75×10^{-04} $SCF/D \cdot ft^2$ are injected into the system.

Figures 6.39 and 6.40 show the results of the study. Pressure and saturation profiles both in caprock and sand are given. Compared to the previous run (low-rate case), we observe that the high water influx reduces the gas column. This is because at high rate the effective stress of the caprock reduces and the permeability increases.

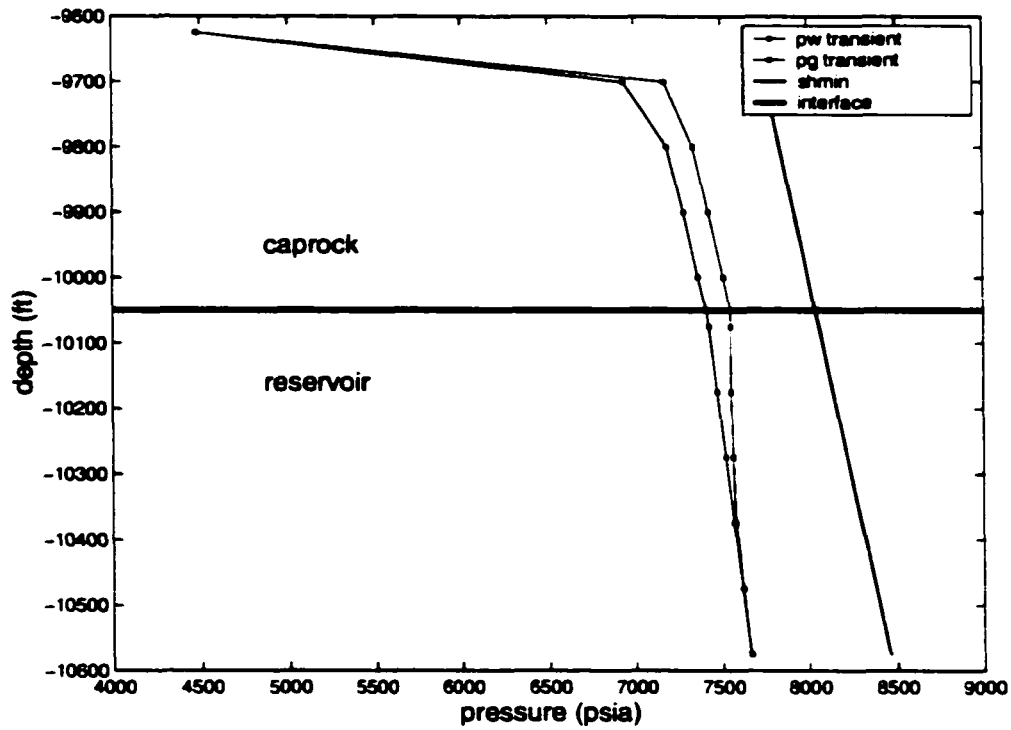

Figure 6.39: Predicted pressure in a 2-D, two-phase system with a dip along $A - A'$ (see also Figure 6.10).

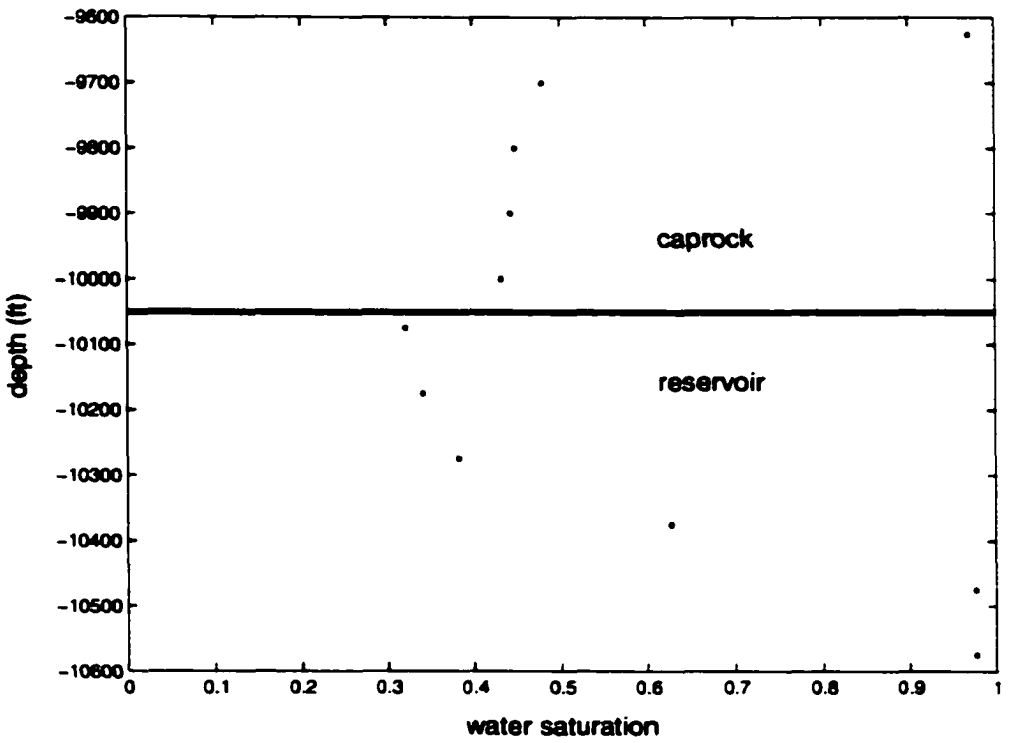

Figure 6.40: Predicted water saturation in a 2-D, two-phase system with a dip along $A - A'$ (see also Figure 6.10).

Figures 6.41, 6.42, and 6.43 show the distribution of the overpressure in the system. Similar to the low-rate case, the pressure in the underlying reservoir and the region near to the base and near to the top of the reservoir increases as it is recorded by the high overpressure in the region. The effective stress distribution of the system is shown in Figures 6.44 and 6.45. Again, similar to the low-rate case, the effective stress near the top of the reservoir decreases as the system approaches steady state.

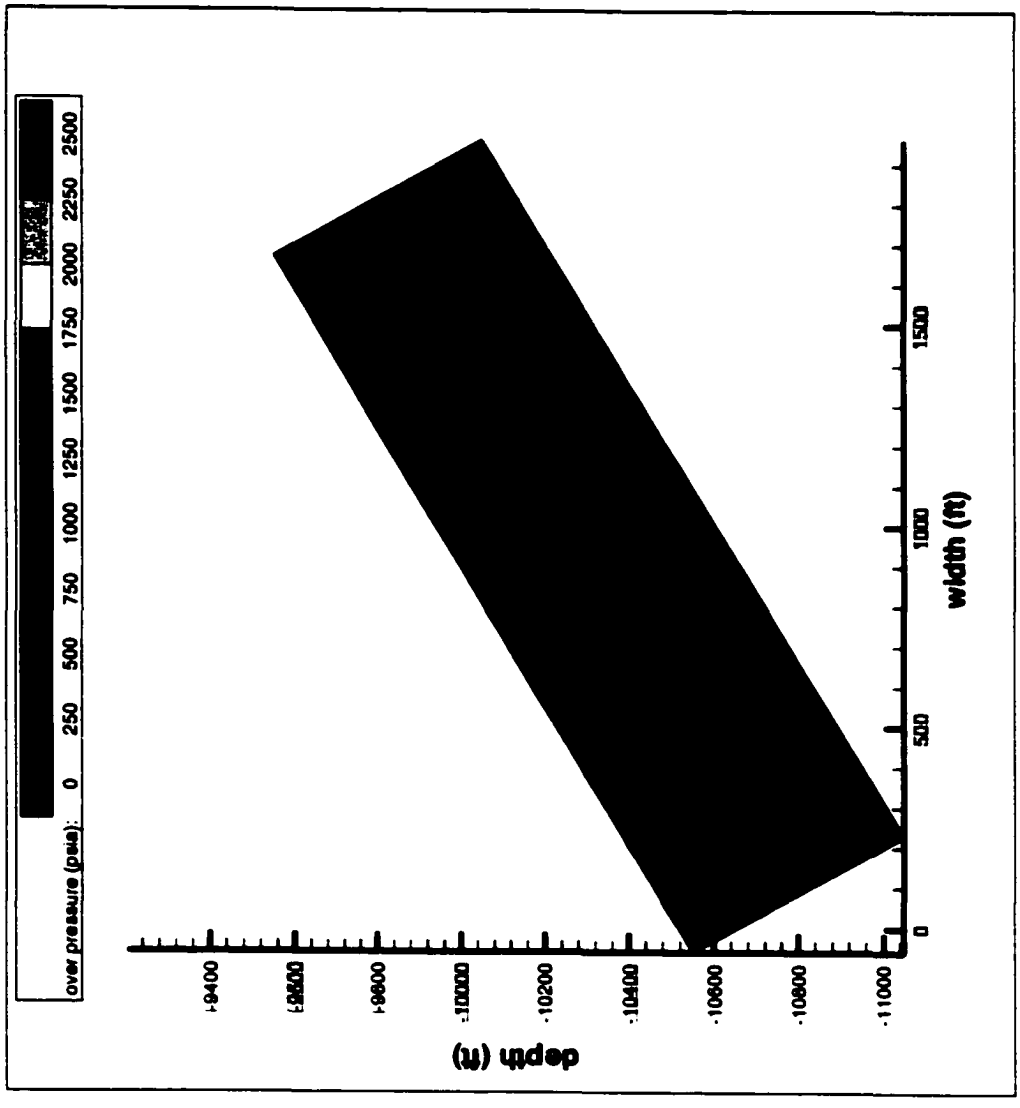

Figure 6.41: Overpressure in a 2-D, two-phase system with a dip at initial time.

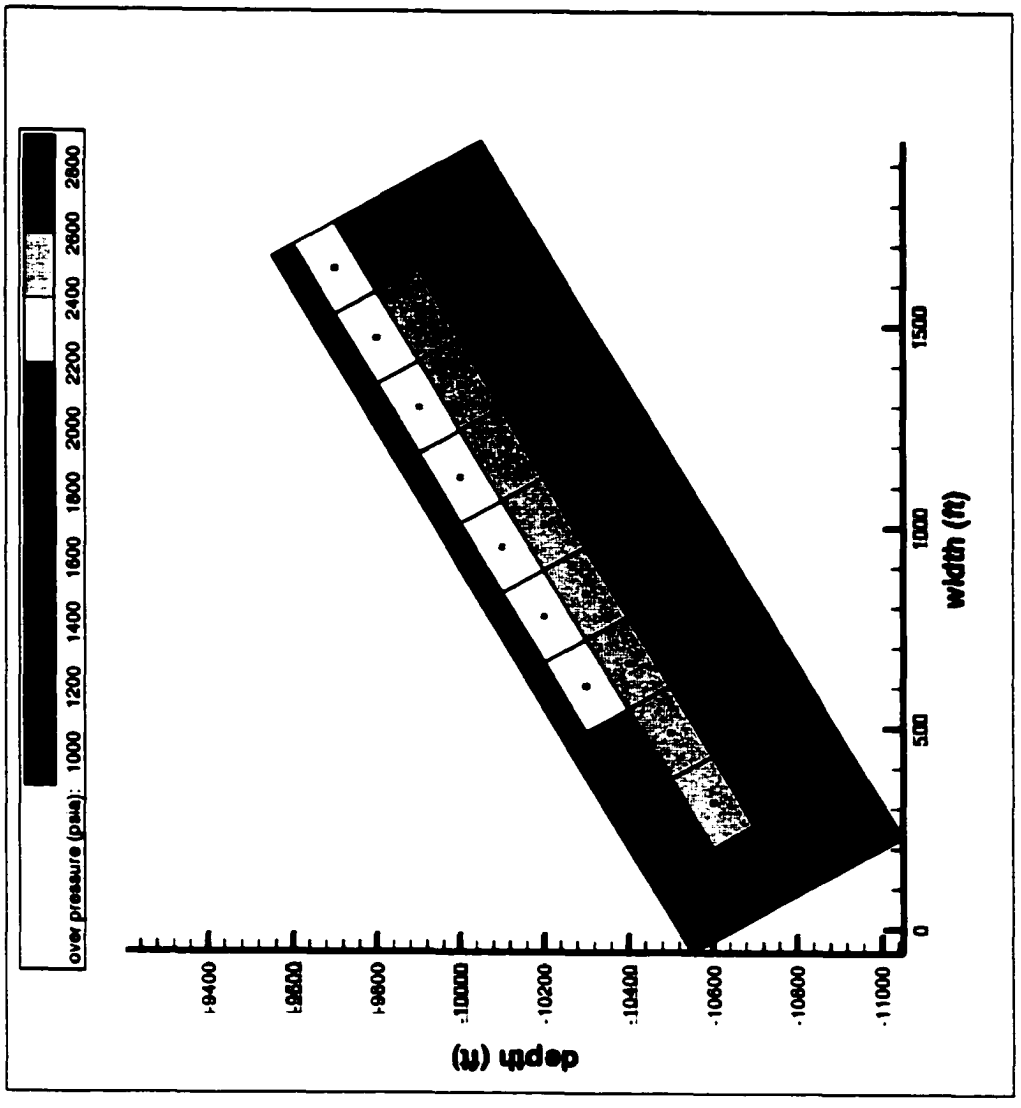

Figure 6.42: Overpressure in a 2-D, two-phase system with a dip at steady state.

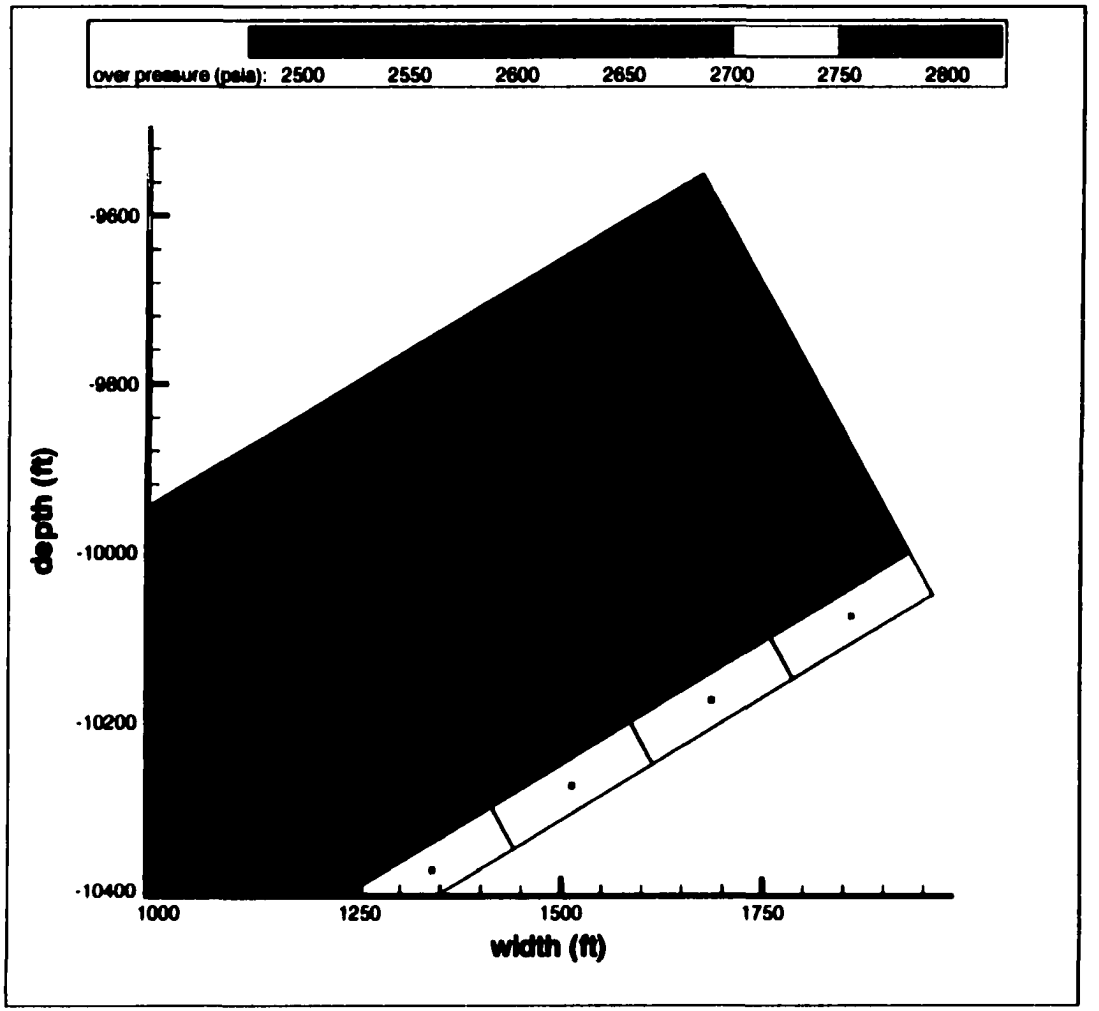

Figure 6.43: Overpressure in a 2-D, two-phase system with a dip at steady state (upper part of the system).

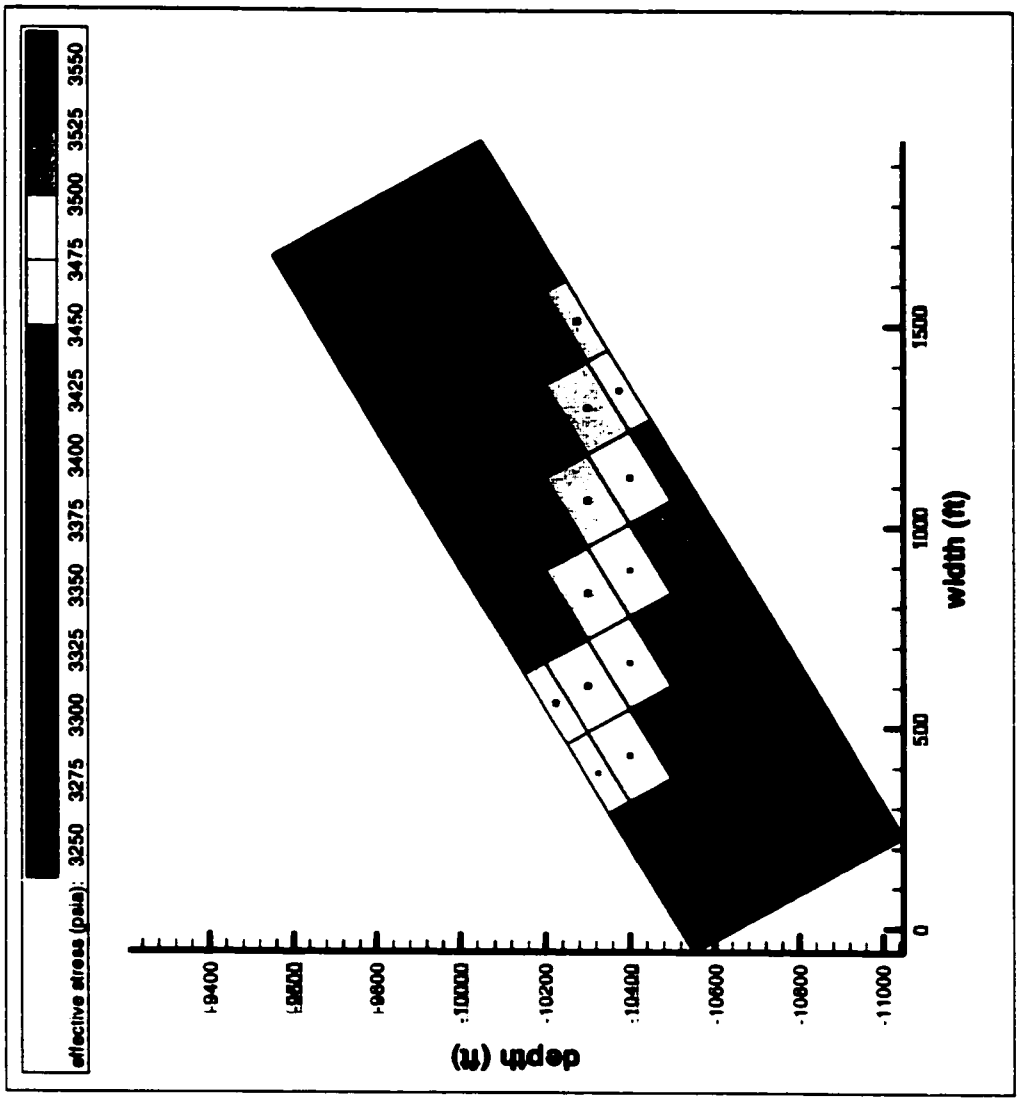

Figure 6.44: Effective stress in a 2-D, two-phase system with a dip at initial time.

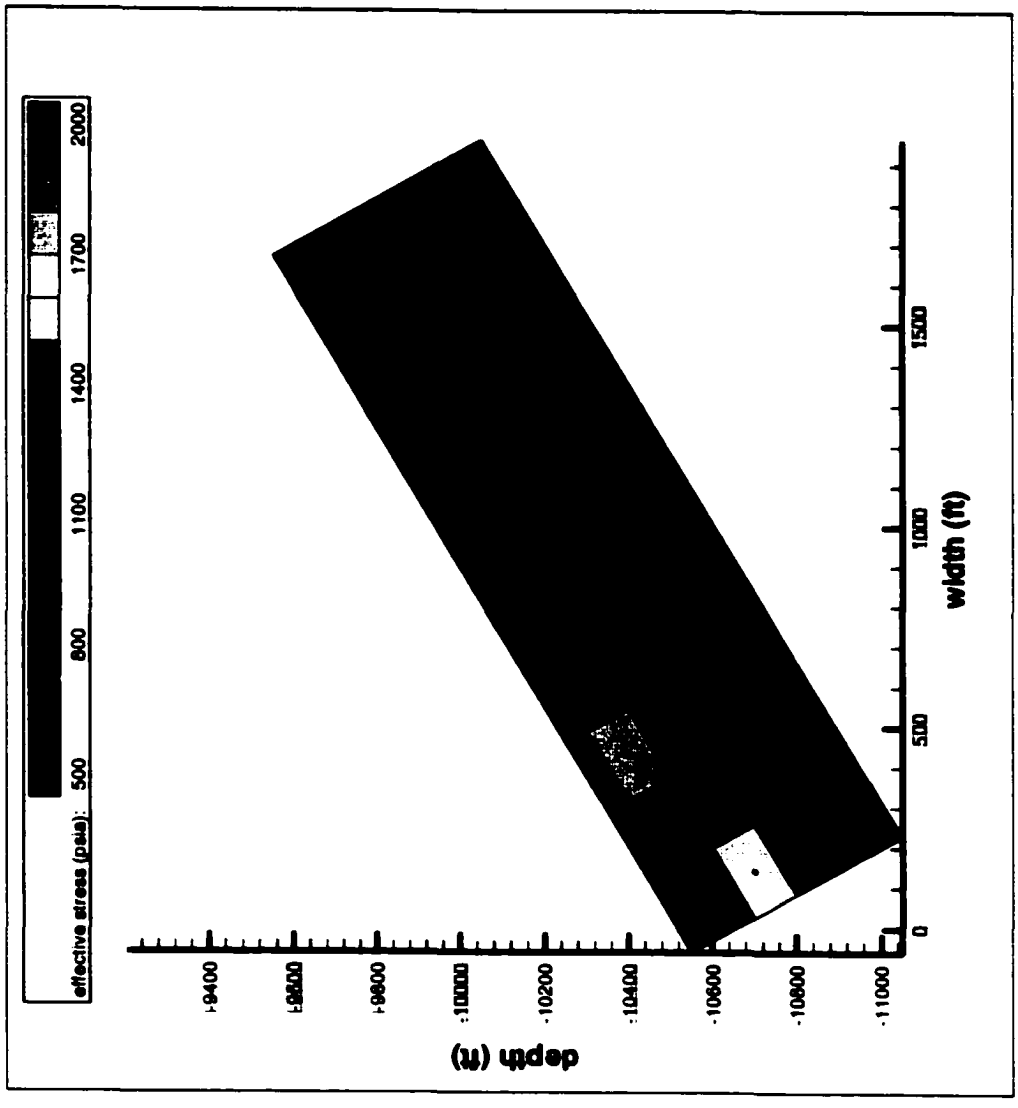

Figure 6.45: Effective stress in a 2-D, two-phase system with a dip at steady state.

The water saturation distributions are shown in Figures 6.46 and 6.47. Initially the system is filled entirely with water. Similar to the low-rate case, gas and water are injected at the base of the reservoir. In this study, we increase the water injection rate and study the capability of the caprock to trap the gas. Figure 6.47 shows the distribution of water saturation in the system. Gas is shown to be accumulated at the top of the reservoir. As we increase the water injection rate, more gas can flow vertically through the caprock due to the low displacement pressure of a caprock. As discussed previously in 1-D case, by increasing the water rate the fracture width will increase and thus decreases the displacement pressure. The result is a smaller gas column in the system.

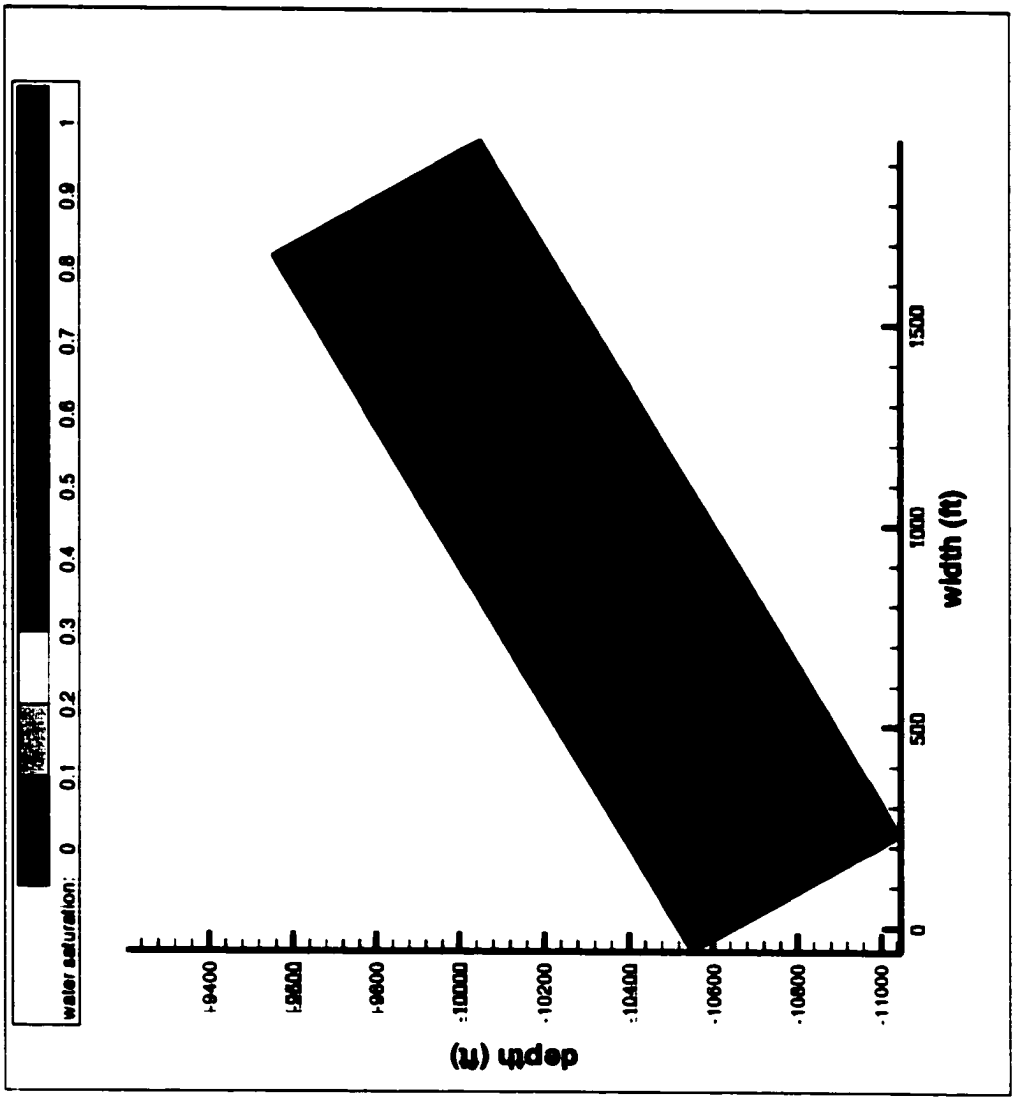

Figure 6.46: Water saturation in a 2-D, two-phase system with a dip at initial time.

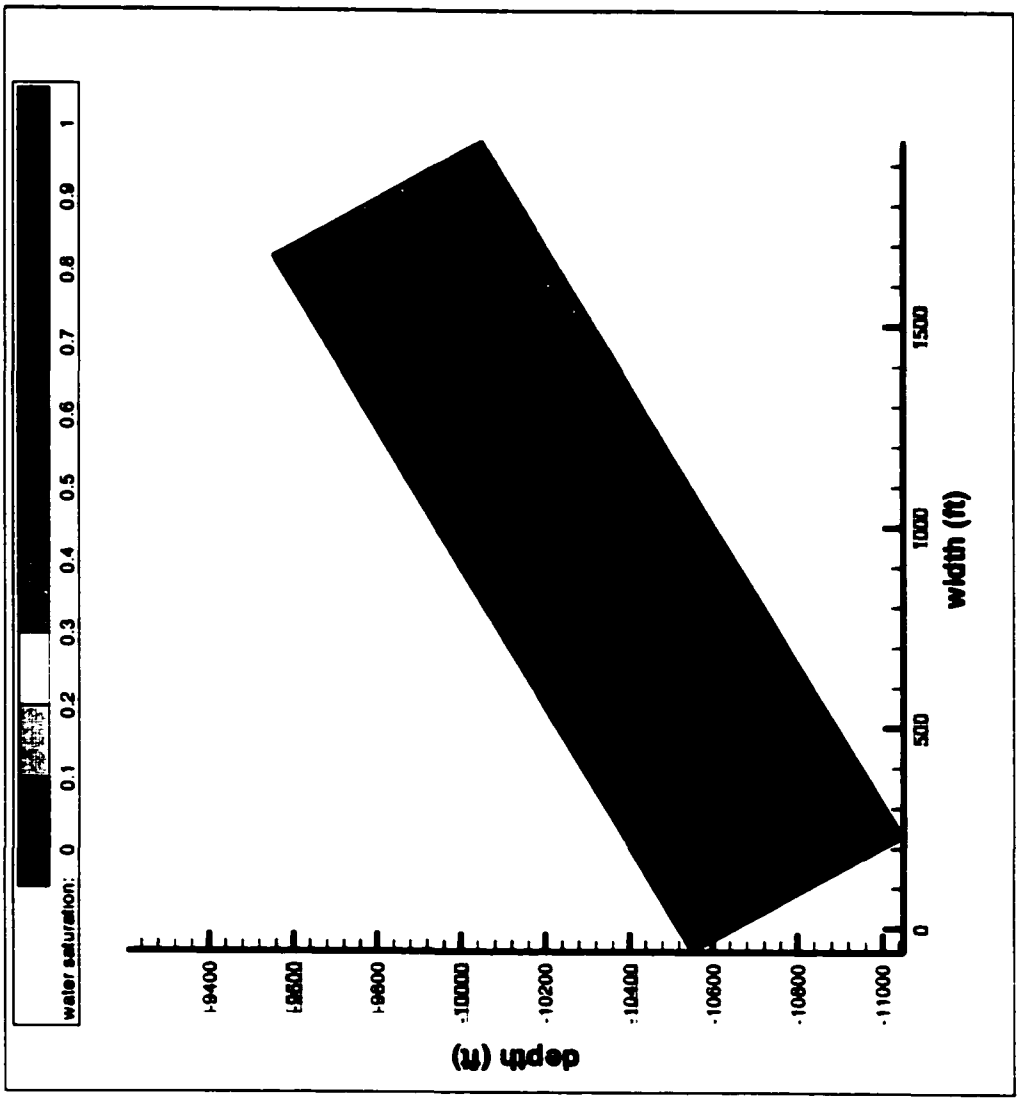

Figure 6.47: Water saturation in a 2-D, two-phase system with a dip at steady state.

The gas and water flow directions are shown in Figures 6.48 and 6.49. We observe the similar behavior of gas and water flow direction with the low-rate case. Most gas escapes from the top of the reservoir due to the high permeability and low displacement pressure of a caprock in that region. Instead of flowing through the high reservoir permeability, the water tends to flow vertically through the caprock. The low water saturation at the top of the sand results in a low water relative permeability in the region.

In a caprock, gas velocity varies from 1×10^{-04} to 1×10^{-08} ft/D. For the region where the gas saturation is high (area with the green color), the velocity in the z-direction is larger than the velocity in the x-direction. The velocity in the x-direction is in between 1×10^{-06} to 1×10^{-07} ft/D while the velocity in the z-direction is in between 1×10^{-04} to 1×10^{-05} ft/D. The gravity and the increase in a caprock permeability in the z-direction cause gas to move vertically. Water velocity in the region is observed to be varied from 1×10^{-10} to 1×10^{-12} ft/D however in the z-direction the water velocity is more uniform (in the order of 1×10^{-09} ft/D).

In the reservoir, water velocity in the x-direction varies from 1×10^{-06} to 1×10^{-07} ft/D. For the z-direction, water velocity varies from 1×10^{-08} to 1×10^{-09} ft/D. We observe the similar behavior with the low-rate case, the velocity in the x-direction is larger than the velocity in the z-direction.

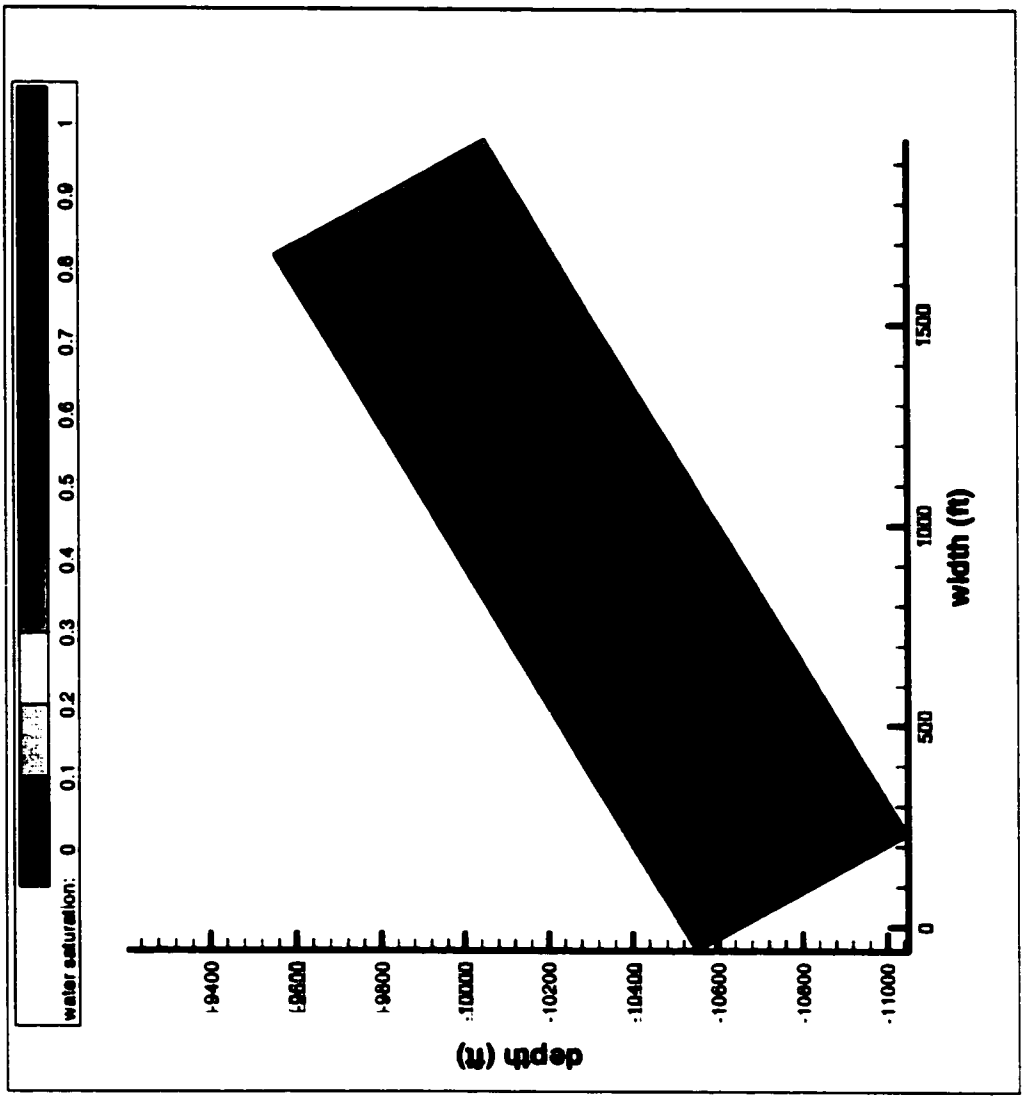

Figure 6.48: Vector flow of gas in a 2-D, two-phase system with a dip at steady state.

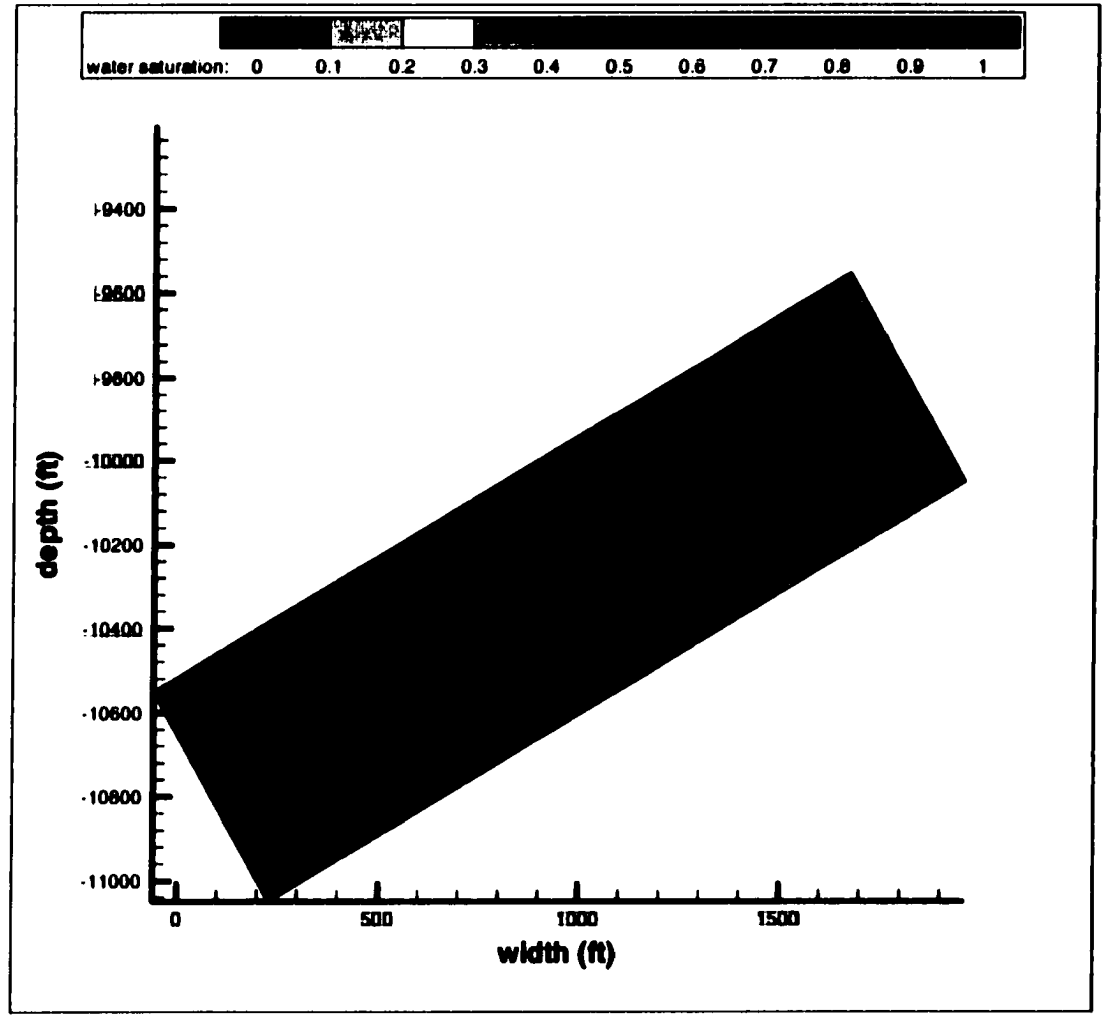

Figure 6.49: Vector flow of water in a 2-D, two-phase system with a dip at steady state.

6.6 Summary

We have developed a 2-D, transient multi-phase flow model to study secondary gas migration from underlying source rock. Three cases are developed. Two cases are developed to study the fracture permeability in a 1-D and in a simple 2-D cases. The simple 2-D case is an extension of a 1-D case (Figure 6.7). The third case describes the study of gas migration where the formations (caprock and reservoir) have a dip (Figure 6.10).

In the 1-D transient study, we focus on the validation of the transient model (at steady state) with the steady-state model. We see the good agreement between the two models. The discrepancies between the two models shown in Figure 6.5 reflects the effect of the grid size. In 1-D transient model, we use the large size of blocks. The cross-sectional area perpendicular to the flow is given in Table 6.1. We also study the pressure build-up in the reservoir and in a caprock. We observe that as the system moves to steady state from the initial state, the pressure in the reservoir increases rapidly. This is due to the low permeability of a caprock. The permeability of the caprock changes as the pressure increase.

The capability of a caprock to trap gas depends mainly on the fracture width. For gas to enter the fracture and to displace the water, the capillary pressure must exceed the displacement pressure of the caprock. At small fracture width, the capillary pressure is high, however as the pressure in the reservoir and caprock increases, the fracture width becomes wider and decreases the displacement pressure of the caprock. By increasing the water influx, the effective stress decreases and the fracture width increases and thus decreases the capability of the caprock to trap gas.

At steady state, the capillary pressure at the interface between a caprock and the reservoir is equal to maintain the continuity of the pressure. Since different capillary pressure relationships apply to the two different formations (caprock and reservoir), there

is a discontinuity in the saturation across the interface. Figure 6.23 shows the relationships between the two capillary pressures. The fluid fluxes determine the gas relative permeability and the caprock capillary pressure. The gas relative permeability then is used to determine the saturation in the caprock. Because the capillary pressures at the interface at steady state are equal, the saturation in a caprock can be used to determine the saturation in a reservoir.

In a 2-D, two-phase flow system with a dip, we observe that most of the gas escapes from the top of the reservoir. We observe that the conductivity of the caprock above the top reservoir increases rapidly as the pressure of the reservoir below increases. The low effective stress in the caprock above the reservoir causes most of the gas to flow through this part of the caprock.

Chapter 7
Conclusions and Recommendations

We have presented a conceptual and quantitative model to describe the interaction between fluid pore pressures, minimum horizontal stress (S_{hmin}) and fracture permeability. The model is then coupled with 1-D steady-state flow and 1-D and 2-D transient-flow models to study fluid flow through a caprock and the trap integrity. The model assumes that all flow in the caprock is via fracture permeability and that permeability is a function of fluid pressure within the fractures and the stress-state in the caprock.

7.1 Conclusions

Based on this research, the following conclusions are drawn:

1. The ability of the caprock to trap gas depends on the permeability of the caprock. A mechanism where the permeability of the caprock increases in the presence of natural factures and in an overpressured environment is presented. Using the model, we have shown that overpressure (fluid pore pressures in excess of hydrostatic) enhances the caprock permeability assuming that the S_{hmin} in the caprock is constant. A simple formulation that relates permeability to fluid pore pressures and the S_{hmin} is developed.

2. Three parameters are found to play an important role in controlling the behavior of the fracture permeability. The first one is the fractional contact area. When the contact area is large, the effective stress needed to yield the same deformation with the small contact area is also large. The second one is the spacing or the distance between the fractures. We have shown that when the spacing increases, the fracture permeability decreases. The third one is the maximum asperity height. The maximum asperity height is defined as the maximum height of the asperities at zero effective stress. It is observed that when the asperity height increases, the fracture permeability increases.

3. The ability of the caprock to trap gas also depends on the width of the fracture. For gas to enter the fracture and to displace the water, the capillary pressure must exceed the displacement pressure of the fracture. At small fracture widths, the displacement pressure is large. We show that this width is a strong function of the effective stress. When the effective stress increases, the width becomes smaller and the displacement pressure becomes larger. At zero effective stress the width is set to the maximum asperity height. In the presence of overpressure, the excess pressure reduces the effective stress. In this situation, the width is large which decreases the ability of the caprock to trap the gas.

4. The pressure gradient in the underlying reservoir at steady-state is nearly hydrostatic. This is due to the high permeability of the reservoir and the small fluid fluxes. However in the caprock, the pressure gradient follows the S_{hmin} gradient which results in a constant effective stress in the caprock. This implies that the pressure generation and dissipation in the caprock are equal (Hart et al., 1995). Since the effective stress in the caprock remains constant, the fracture width is also constant which leads to the constant capillary pressure. The gas pressure gradient thus will follow the S_{hmin} gradient $(\frac{dp_w}{dz} = \frac{dp_g}{dz} = \frac{d(Shmin)}{dz})$.

5. In the calculation of the effective stress, the developed formulation is based on the water pressure. In this research, we work with the water-wet system therefore we use the water pressure to control the fracture width. It is found that when water influx increases, the fracture width increases. This affects the ability of the caprock to trap gas. In our models, water saturation in the caprock at steady state is nearly constant.

7.2 Recommendations

The proposed fracture model assumes that a fracture behaves like a smooth parallel-plate. This assumption is based on the relatively small contact area between asperities and the fracture wall in the model. Further research involving distribution of the asperities which can suitably describe the roughness of the fracture surface is needed. Furthermore, the change of the fractional contact area as a function of the effective stress is also needed. This can be done most effectively by applying the appropriate distribution of the asperities (e.g. lognormal distribution) to the developed formulation of the effective stress and integrate the model to the developed steady-state flow and the transient flow models.

As noted earlier, we use water pressure rather than gas pressure to control the fracture width. We recognize that at high gas saturation, gas pressure will contribute to the opening of the fracture. Further study to investigate the effect of using gas pressure instead of water pressure or the combination of both (water and gas pressures) through their saturations (e.g. $p_{avg} = S_w p_w + S_g p_g$) to control the fracture width on the accumulation of gas in the reservoir is needed.

More parametric studies are also needed. Questions such as how fast the gas can bleed off and under what circumstances do the gas can bleed off once the charge stops need to be answered. To address these questions, it is desirable to run a number of transient simulations with variable charge rates. It is also valuable to run sensitivity studies looking at relative permeability and caprock capillary pressure models.

Nevertheless, the most pressing problem in the secondary gas migration is to predict the presence of an effective seal which controls the reservoir column height under various phase problems. In this research, we apply the concept to the single and two-phase problems. Much can be learned by constructing a two-phase model, however in the petroleum fluid migration, the presence of the complex three-phase flow exists.

Thus, it is important to extend this work to model three-phase flow involving gas and oil that flow through the water-saturated caprock.

References

Amyx, J. W., Bass, D. M., and Whiting, R. L., 1960, Petroleum reservoir engineering: McGraw-Hill, New York, 610 pp.

Archard, J. F., 1957, Elastic deformation and the laws of friction: Proceeding of the Royal Society of London, Series A, v. 243, pp. 190-205.

Ashby, M. F., and Jones, D. R. M., 1996, Engineering materials 1: Butterworth-Heinemann, Oxford, 306 pp.

Ashbaugh, J. P., 1997, Numerical and analytical model of secondary migration in faults: Dynamic control on hydrocarbon column height. M.Sc. thesis, Pennsylvania State University.

Bear, J., 1972, Dynamics of fluids in porous media: Elsevier Scientific, New York, 764 pp.

Bennett, M. H., 1996, Simulation of secondary migration in faults: Dynamic control on hydrocarbon column height: M.Sc. thesis, Pennsylvania State University.

Berg, R. R., 1975, Capillary pressure in stratigraphic traps: AAPG. Bulletin, v. 59, pp. 939-956.

Corey, A. T., 1954, The interrelationship between gas and oil relative permeabilities: Prod. Mon., pp. 38-41.

Downey, M. W., 1984, Evaluating seals for hydrocarbon accumulations: AAPG. Bulletin, v. 68, No. 11, pp. 1752-1763.

Elsworth, D., and Mase, C. R., 1993, Groundwater in rock engineering: Comprehensive rock engineering, v. 1, pp. 201-226.

England, W. A., and Fleet, A. J., eds., 1991, Petroleum migration: Geological Society Special Publication 58, 280 pp.

England, W. A., Mackenzie, A. S., Mann, D. M., and Quigley, T. M., 1987, The movement and entrapment of petroleum fluids in the subsurface: Journal of Geological Society, v. 144, pp. 327-347.

Ertekin, T., Abou-Kassem, J. H., and King, G. R., 2001, Basic Applied Reservoir Simulation: SPE. Textbook Series, v. 7, The Society of Petroleum Engineers Inc., 406 pp.

Finkbeiner, T., Zoback, M., Flemings, P. B., and Stump, B., 2001, Stress, pore pressure, and dynamically constrained hydrocarbon columns in the South Eugene Island 330 field, northern Gulf of Mexico, AAPG. Bulletin, v. 85, No. 6, pp. 1007-1031.

Fisher, A. T., and Zwart, G., 1996, Relation between permeability and effective stress along a plate-boundary fault, Barbados accretionary complex: Geology, v. 24, pp. 307-310.

Fisher, A. T., and Zwart, G., 1997, Packer experiments along the decollement of the Barbados accretionary complex: Measurements of in situ permeability, in Ogawa, Y., Shipley, T. H., Blum, P., and Bahr, J. M., Proceeding of the Ocean Drilling Program, Scientific Results, v. 156: College Station, Texas, Ocean Drilling Program (in Press).

Gangi, A. F., 1978, Variation of whole and fractured porous rock permeability with confining pressure: International Journal of Rock Mechanics and Mining Sciences & Geomechanics Abstract, v. 15, pp. 249-257.

Gangi, A. F., and Carlson, R. L., 1996, An asperity-deformation model for effective pressure: Tectonophysics, v. 256, pp. 241-251.

Greenwood, J. A., and Williamson, J. B. P., 1966, Contact of nominally flat surfaces: Proceeding of the Royal Society of London, Series A, v. 295, pp. 300-318.

Gussow, W. C., 1954, Differential entrapment of oil and gas: AAPG. Bulletin, v. 38, pp. 816-853.

Hart, B. S., Flemings, P. B., and Deshpande, A., 1995, Porosity and pressure: Role of compaction disequilibrium in the development of gepresures in a Gulf Coast Pleistocene basin: Geology, v. 23, No. 1, pp. 45-48.

Hubbert, M. K., 1953, Entrapment of petroleum under hydrodynamic conditions: AAPG. Bulletin, v. 37, No. 8, pp. 1954-2026.

IMSL, 1978, Fortran77 IMSL Library: Imsl Inc.

Iwai, K., 1976, Fundamental studies of the fluid flow through a single fracture: Ph.D. thesis, University of California, Berkeley.

Jones, F. O., 1975, A laboratory study of the effects of confining pressure on fracture flow and storage capacity in carbonate rocks: Journal of Petroleum Technology, pp. 21-27.

McCain Jr., W. D., 1991, Reservoir-fluid property. Correlations-state of the art: SPE Reservoir Engineering, pp. 266-272.

Muskat, M., 1937, Flow of homogenous fluids: McGraw-Hill Book Comp., New York.

Nelson, R., 1975, Fracture permeability in porous reservoirs: Experimental and field approach: Ph.D dissertation, Texas A&M Univ., College Station.

Neuzil, C. E., and Tracy, J. V., 1981, Flow through fractures: Water Resources Research, v. 17, pp. 191-199.

Persoff, P., Pruess, K., and Myer, L., 1991, Two-phase flow visualization and relative permeability measurements in transparent replicas of rough-walled fracture: Sixteenth Workshop on Geothermal Reservoir Engineering, Workshop Rep. SGP-TR-134, Standford Geotherm Program, Standford Univ., Standford, Calif., pp. 203-210,

Pruess, K., and Tsang, Y. W., 1990, On two-phase relative permeability and capillary pressure of rough-walled rock fractures: Water Resources Research, v. 26, pp. 1915-1926.

Reitsma, S., and Kueper, B. H., 1994, Laboratory measurement of capillary pressure-saturation relationships in a rock fracture: Water Resources Research, v. 30, pp. 865-878.

Renshaw, C. E., 1995, On the relationship between mechanical and hydraulic apertures in rough-walled fractures: Journal of Geophysical Research, v. 100, pp. 24,629-24,636.

Romm, E. S., 1966, Fluid flow in fractured rocks (in Russian): Nedra, Moscow. (English translation, Blake, W. R., 1972, Oklahoma)

Schowalter, T. T., 1976, The mechanics of secondary hydrocarbon migration and entrapment: Earth Science Bulletin, v. 9, pp.43.

Screaton, E. J., Fisher, A. T., Carson, B., and Becker, K., 1997, Barbados ridge hydrologic tests: Implications for fluid migration along an active decollement: Geology, v. 25, pp. 239-242.

Sims, J. E., Elsworth, D., and Cherry, J. A., 1996, Stress-dependent flow through fractured clay till: A laboratory study: Canadian Geothechnical Journal, v. 33, pp. 449-457.

Smith, D. A., 1966, Theoretical considerations of sealing and non-sealing faults: AAPG. Bulletin, v. 50, pp. 363-374.

Sharp, J. C., 1970, Fluid flow through fissured media: Ph.D thesis, University of London.

Snow, D. T., 1965, A parallel plate model of fractured permeable media: Ph.D. thesis, University of California, Berkeley.

Snow, D. T., 1970, The frequency and apertures of fractures in rock: International Journal of Rock Mechanics and Mining Sciences & Geomechanics Abstract, v. 7, pp. 33-40.

Thomas, M. M., and Clouse, J. A., 1995, Scaled physical model of secondary migration: AAPG. Bulletin, v. 79, pp. 19-29.

Thomeer, J. H. M., 1960, Introduction of a pore geometrical factor defined by the capillary pressure curve: Journal of Petroleum Technology, pp. 73-77.

Tsang, Y. W., and Witherspoon, P. A., 1981, Hydromechanical behavior of a deformable rock fracture subject to normal stress: Journal of Geophysical Research, v. 86, pp. 9287-9298.

Tsang, Y. W., and Witherspoon, P. A., 1983, The dependence of fracture mechanical and fluid flow properties on fracture roughness and sample size: Journal of Geophysical Research, v. 88, pp. 2359-2366.

Van Golf-Racht, T. D., 1982, Fundamental of fractured reservoir engineering: Elsevier Scientific, New York.

Walsh, J. B., 1965, The effect of cracks on the uniaxial elastic compression of rocks: Journal of Geophysical Research, v. 70, pp. 399-411.

Walsh, J. B., 1981, Effect of pore pressure and confining pressure on fracture permeability: International Journal of Rock Mechanics and Mining Sciences & Geomechanics Abstract, v. 18, pp. 429-435.

Walsh, J. B., and Grosenbaugh, M. A., 1979, A new model for analyzing the effect of fracture on compressibility: Journal of Geophysical Research, v. 84, pp. 3532-3536.

Watts, N. L., 1987, Theoretical aspects of cap-rock and fault seals for single and two-phase hydrocarbon columns: Marine and Petroleum Geology, v. 4, pp. 274-307.

Witherspoon, P. A., Wang, J. S. Y., Iwai, K., and Gale, J. E., 1980, Validity of cubic law for fluid flow in a deformable rock fracture: Water Resources Research, v. 16, pp. 1016-1024.

Appendix A

Reservoir fluid properties

It is assumed that water density at standard conditions is 67 lb/ft^3 and the percent salinity is 0 %. Temperature is constant at 100 $°F$.

Table A.1: Water properties

Pressure (p) $psia$	Water viscosity (μ_w) cp	Water formation volume factor (B_w) RB/STB	Water density (ρ_w) lb/ft^3	Gas solution (R_{sw}) SCF/STB
14.7	0.62573	1.0088	66.413	0
514.7	0.63885	1.0085	66.436	0
2014.7	0.68404	1.0067	66.552	0
2514.7	0.70105	1.0059	66.608	0
3014.7	0.71903	1.0049	66.671	0
3514.7	0.73798	1.0039	66.743	0
4014.7	0.75791	1.0027	66.823	0
4514.7	0.77880	1.0013	66.911	0
5014.7	0.80067	0.9998	67.008	0
5514.7	0.82351	0.9983	67.113	0
7014.7	0.89786	0.9928	67.481	0
7514.7	0.92459	0.9908	67.621	0
8014.7	0.95229	0.9886	67.770	0
8514.7	0.98096	0.9863	67.928	0
9014.7	1.01060	0.9839	68.095	0

Table A.2: Gas properties

Pressure (p) $psia$	Gas viscosity (μ_g) cp	Gas formation volume factor (B_g) RB/SCF	Gas density (ρ_g) lb/ft^3
14.7	0.011074	0.1914300	0.0500
514.7	0.011887	0.0049830	1.9231
1014.7	0.013351	0.0022951	4.1753
2014.7	0.018552	0.0010163	9.4292
2514.7	0.021830	0.00081540	11.752
3014.7	0.025030	0.00070349	13.622
3514.7	0.027970	0.00063484	15.095
4014.7	0.030618	0.00058903	16.269
4514.7	0.033000	0.00055630	17.226
5014.7	0.035160	0.00053162	18.026
5514.7	0.037137	0.00051220	18.709
7014.7	0.042257	0.00047208	20.299
7514.7	0.043763	0.00046238	20.725
8014.7	0.045192	0.00045387	21.114
8514.7	0.046554	0.00044630	21.472
9014.7	0.047858	0.00043951	21.803

VITA

VICTOR SIAHAAN

Born on June 2, 1963 in Bogor, Indonesia

Education

1/96 - 5/02	Ph.D. in Petroleum and Natural Gas Engineering, The Pennsylvania State University, University Park, PA 16802
5/93 - 1/95	M.S. in Petroleum and Natural Gas Engineering, The Pennsylvania State University, University Park, PA 16802
8/85 - 5/90	B.S. in Gas and Petrochemical Engineering, University of Indonesia, Depok, Jawa Barat, Indonesia
8/83 - 8/85	Freshman and Sophomore in Physics Science, University of Indonesia, Jakarta, Indonesia

Experience

1/98 - 5/02	Research Assistant at the Petroleum and Natural Gas Engineering Section, The Pennsylvania State University, University Park, PA 16802
3/96 - 1/98	Teaching Assistant at the Petroleum and Natural Gas Engineering Section, The Pennsylvania State University, University Park, PA 16802
1/95 - 3/96	Reservoir Engineer at consulting company, Jakarta, Indonesia

Honor

1/93 - 1/95	Consortium Pertamina-Production Sharing Contractors Fellowship